DOT/FAA/TCTT-23/53

Federal Aviation Administration
William J. Hughes Technical Center
Aviation Research Division
Atlantic City International Airport
New Jersey 08405

Ductile Fracture of Aluminum 2024-T351, Ti-6Al-4V, and Inconel 718 under Complex States of Stress

September 2023
Technical Thesis

The research described in this report was funded by the FAA as part of its mission to improve aircraft safety. The views and opinions expressed are those of the author alone and do not necessarily represent the views of the FAA. The FAA assumes no liability for the contents or use thereof. The FAA has not edited or modified the contents of the report in any manner.

U.S. Department of Transportation
Federal Aviation Administration

NOTICE

This document is disseminated under the sponsorship of the U.S. Department of Transportation in the interest of information exchange. The U.S. Government assumes no liability for the contents or use thereof. The U.S. Government does not endorse products or manufacturers. Trade or manufacturers' names appear herein solely because they are considered essential to the objective of this report. The findings and conclusions in this report are those of the author(s) and do not necessarily represent the views of the funding agency. This document does not constitute FAA policy. Consult the FAA sponsoring organization listed on the Technical Documentation page as to its use.

This report is available at the Federal Aviation Administration William J. Hughes Technical Center's Full-Text Technical Reports page: actlibrary.tc.faa.gov in Adobe Acrobat portable document format (PDF).

Technical Report Documentation Page

Form DOT F 1700.7 (8-72) Reproduction of completed page authorized

1. Report No.	2. Government Accession No.	3. Recipient's Catalog No.
DOT/FAA/TCTT-23/53		

4. Title and Subtitle	5. Report Date
Ductile Fracture of Aluminum 2024-T351, Ti-6Al-4V, and Inconel 718 under Complex States of Stress	May 2022
	6. Performing Organization Code

7. Author(s)	8. Performing Organization Report No.
Bryson Knott	DOT/FAA/TCTT-23/53

9. Performing Organization Name and Address	10. Work Unit No. (TRAIS)
Graduate Program in Mechanical Engineering The Ohio State University	11. Contract or Grant No.

12. Sponsoring Agency Name and Address	13. Type of Report and Period Covered
	14. Sponsoring Agency Code

15. Supplementary Notes

16. Abstract

Many high-rate impact applications in the aerospace industry, such as a fan blade out event, can induce ductile fracture under loading conditions that are difficult to replicate experimentally. Varying temperatures and strain rates can influence fracture behavior, but the primary variable that drives fracture initiation in a ductile material is the state of stress. If numerical models of applications involving ductile fracture at complex stress states are to be trusted, it is necessary to develop novel fracture testing techniques that can be used to calibrate fracture criteria in finite element material models.

A novel test technique is used to induce asymmetric in-plane biaxial tension and out-of-plane compression. The materials of interest for this test are Titanium 6Al-4V and Inconel 718. A small, elliptical shaped punch is advanced into a thin plate of specimen material, inducing an unequal amount of biaxial in-plane tension. A 1075 steel backing plate is in clamped to the back surface of the specimen plate, inducing out-of-plane compression. Test parameters such as the specimen thickness, backing plate thickness, and punch geometry can be varied to alter the stress state. The commercial finite element code LS-DYNA is used to simulate the test and fine tune the state of stress in order to optimize the geometries for calibration of fracture models. The software is also used to validate experimental results and determine the equivalent plastic strain at fracture in the tests.

17. Key Words	18. Distribution Statement
Aircraft Engines - fatigue and Fracture mechanics	This document is available to the U.S. public through the National Technical Information Service (NTIS), Springfield, Virginia 22161. This document is also available from the Federal Aviation Administration William J. Hughes Technical Center at actlibrary.tc.faa.gov.

19. Security Classif. (of this report)	20. Security Classif. (of this page)	21. No. of Pages	19. Security Classif. (of this report)
Unclassified	Unclassified	150	Unclassified

Ductile Fracture of Aluminum 2024-T351, Ti-6Al-4V, and Inconel 718 under Complex States of Stress

Thesis

Presented in Partial Fulfillment of the Requirements for the Degree Master of Science in the Graduate School of The Ohio State University

By

Bryson Knott, B.S.

Graduate Program in Mechanical Engineering

The Ohio State University

2023

Thesis Committee

Professor Amos Gilat, Advisor

Professor Jeremy Seidt

Abstract

Many high-rate impact applications in the aerospace industry, such as a fan blade out event, can induce ductile fracture under loading conditions that are difficult to replicate experimentally. Varying temperatures and strain rates can influence fracture behavior, but the primary variable that drives fracture initiation in a ductile material is the state of stress. If numerical models of applications involving ductile fracture at complex stress states are to be trusted, it is necessary to develop novel fracture testing techniques that can be used to calibrate fracture criteria in finite element material models.

A novel test technique is used to induce asymmetric in-plane biaxial tension and out-of-plane compression. The materials of interest for this test are Titanium 6Al-4V and Inconel 718. A small, elliptical shaped punch is advanced into a thin plate of specimen material, inducing an unequal amount of biaxial in-plane tension. A 1075 steel backing plate is in clamped to the back surface of the specimen plate, inducing out-of-plane compression. Test parameters such as the specimen thickness, backing plate thickness, and punch geometry can be varied to alter the stress state. The commercial finite element code LS-DYNA is used to simulate the test and fine tune the state of stress in order to optimize the geometries for calibration of fracture models. The software is also used to validate experimental results and determine the equivalent plastic strain at fracture in the tests.

Another novel test technique is introduced to induce a state of stress analogous to plane strain compression. A notched ring geometry is compressed axially in a hydraulic load frame. Naturally, this induces axial compression. The notch in the center of the specimen causes it to buckle inward, which induces a small compressive radial stress. Poisson's effect causes

compressive stress in the tangential direction. The materials of interest for this test are Aluminum 2024-T351, Titanium 6Al-4V, and Inconel 718. Once again, LS-DYNA is used to aid in the design of the test geometries, as well as to validate test results and determine the equivalent plastic strain at fracture in the tests.

Dedication

Dedicated to my family and friends.

Acknowledgments

I am incredibly grateful for all of the people who have helped shape me into the person I am today. First and foremost, thank you to my parents, Dennis and Pauline Knott, for your love and support throughout my entire life. Thanks also to my sister, Kylee, and brother, Brody, for being constant sources of love and friendship. I would like to acknowledge my friends for all of the memories over the years that will last a lifetime. To Alli Dendinger, thank you for giving me strength and encouragement when I needed it most.

I have a great amount of appreciation for my advisor, Dr. Amos Gilat, for giving me the opportunity to work in his lab and learn from his expertise. The strides I have made as an engineer and as a professional in general over the past two years would not have been possible without his guidance. Thanks also to Dr. Jeremy Seidt for the mentorship, training, and advice he provided. I saw Jeremy as a second advisor, and he deserves a great deal of credit for his input to this work. I also want to acknowledge Dr. Nathan Spulak for his mentorship during my first year. This work is a continuation of what he had already accomplished, and I'm grateful for his efforts in preparing me to take on this project.

This research was funded by the Federal Aviation Administration and performed in collaboration with the National Aeronautics and Space Administration, George Mason University, and the University of Dayton. Thank you to all members of this team for your valuable input and guidance: Dr. Daniel Cordasco, Dr. Tom Vasko, Dr. Michael Pereira, Duane Revilock, Dr. Kelly Carney, Paul Du Bois, Dr. Cing-Dao (Steve) Kan, Dr. Leyu (Doug) Wang, Dr. C.K. Park, Dr. Stefano Dolci, and Dr. Robert Lowe.

Finally, I would like to thank some more of my colleagues at The Ohio State University. First, thanks to machinists Chad Bivens, Kevin Wolf, and Aaron Orsborn for their quality fabrication work and advice on numerous projects I was involved in. The following members of the Dynamic Mechanics of Materials Laboratory were also integral to my success through the help and friendship they provided: Kelton Rieske, Dr. Jarrod Smith, Mark Konieczny, Michael Burton, Jerome Klein, Jeremy Massie, Vedant Joshi, Gaurav Upadhyay, and Peiyu Yang.

Vita

2017…….....St. Thomas Aquinas High School,
Louisville, OH

2021……...B.S. Mechanical Engineering,
The Ohio State University

2021-present…….…….Graduate Research Associate,
Dynamic Mechanics of Materials Laboratory,
Department of Mechanical and Aerospace Engineering,
The Ohio State University

Fields of Study

Major Field: Mechanical Engineering

Specializations: Experimental Mechanics, Ductile Fracture, Finite Element Analysis, Computational Mechanics

Table of Contents

List of Tables

List of Figures

Chapter 1 Introduction

1.1 Motivation and Objectives

Finite element analysis (FEA) is a powerful engineering tool used to simulate and analyze a wide range of physical phenomena. LS-DYNA, a commercial finite element code developed by the former Livermore Software Technology Corporation (acquired by Ansys in 2019), is a popular choice for simulating high-rate impact loading events. Accurately modeling catastrophic aircraft engine failure events, such as a fan blade out scenario, is of particular interest in the aerospace industry.

In 1989, the United Airlines Flight 232 DC-10 commercial aircraft experienced an uncontained fan blade out event that disabled the redundant flight control systems, and the resulting crash landing killed 112 passengers [1]. The Federal Aviation Administration (FAA) Aircraft Catastrophic Failure Prevention Program (ACFPP) was created in response to this tragedy. Uncontained engine failure mitigation has been one of the primary research focuses of this program since its inception [2]. Unfortunately, uncontained engine failure events continue to plague aircraft in modern times. A fragment of a fan cowl caused a cabin window to detach from the plane and cause rapid depressurization of the cabin on Southwest Airlines Flight 1380 in 2018. One death and eight minor injuries resulted from the event [3]. In 2021, United Airlines Flight 328 experienced fan blade fractures in the right engine which caused significant damage and an emergency landing. No casualties resulted from this event, but debris falling from the sky posed a dangerous risk to those on the ground below [4]. Figure 1.1 shows damage from each of these events. The FAA has collaborated with industry and academia to develop research aimed at preventing these types of failures. One such collaboration is the LS-DYNA Aerospace Working

Group (AWG). The AWG is a team of federal agencies, industry partners, and university research labs working together to improve numerical modeling of aerospace-related applications in LS-DYNA.

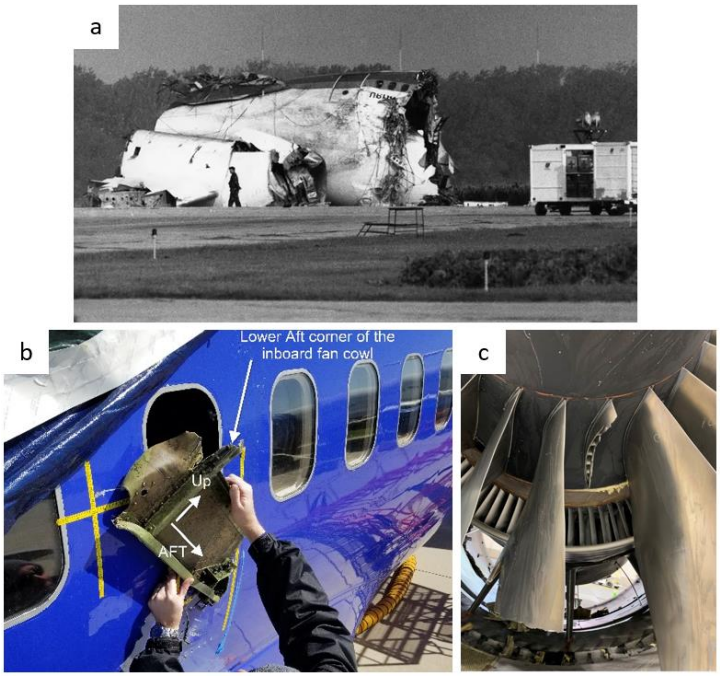

Figure 1.1: (a) Crash site of United Airlines Flight 232, (b) debris and site of detached window of Southwest Airlines Flight 1380, and (c) fractured fan blades on United Airlines Flight 328

Material model development has been an important research focus for the AWG in recent years. The group has created tabulated Johnson-Cook material models known as *MAT_224 for Aluminum 2024-T351 (Al-2024), Ti-6Al-4V (Ti64), and Inconel 718 (In718). The models rely heavily on mechanical test data at various stress states, strain rates, and temperatures. Stress-strain relations are input from material characterization test results to model the plastic behavior

of the materials. The equivalent plastic strains at fracture taken from fracture test series are used to generate fracture criteria, which are modeled using element erosion in simulation.

From ballistic impact validation tests of the original *MAT_224 Al-2024 model, it was discovered that ductile fracture tended to occur in a state of in-plane biaxial tension and out-of-plane compression [5]. The original test dataset for Al-2024 lacked data under this state of stress. Therefore, a modified version of the standard ASTM E643 metallic punch test was introduced to determine the equivalent strain to fracture under this state of stress [6][7]. A punch made of a material that can be treated as approximately rigid is advanced into a thin plate of specimen material. A plate of a suitable thickness and material is placed behind the specimen plate to induce out-of-plane compression on the back surface of the specimen. When using a hemispherical punch geometry, the specimen experiences equi-biaxial in-plane tension. When using an elliptical punch geometry, there is an unequal amount of in-plane tension. Tests with a hemispherical punch geometry were performed on Al-2024, Ti64, and In718, and tests with an elliptical punch geometry were performed on Al-2024 [8]. The goal of this research is to continue this test series by performing elliptical backed punch tests on Ti64 and In718. The test geometries are optimized through finite element analysis (FEA) in LS-DYNA to find geometries that would induce useful stress states for the calibration of the Ti64 and In718 *MAT_224 models. Then, the tests are performed and used to determine the equivalent strain to fracture under the states of stress specified by the design simulations.

Another particularly difficult state of stress to achieve experimentally is one of plane strain compression. A novel notched ring specimen geometry is proposed to study this state of stress for Al-2024, Ti64, and In718. Fracture test data for *MAT_224 models under compressive

dominated stress states are sparse. Therefore, material fracture behavior models under compressive states of stress largely rely on extrapolations from other test data. Because fracture strains become much higher in compressive states of stress relative to other loading conditions, these extrapolations are not necessarily reliable. Compression tests using the novel notched ring design can provide insights into the equivalent strain to fracture under a state of plane strain compression. This data can then be interpolated to calibrate *MAT_224 material models to better predict fracture under other compressive states of stress.

1.2 Literature Review

The theory behind *MAT_224 is based on the well-known Johnson-Cook phenomenological material model [9]. In this model, the von Mises flow stress $\bar{\sigma}$ is given by

$$\bar{\sigma} = \left[A + B(\bar{\epsilon_p})^n\right][1 + C\ \ln\dot{\epsilon}^*][1 - (T^*)^m] \tag{1.1}$$

where *A*, *B*, *n*, *C*, and *m* are material constants. *A*, *B*, and *n* are strain hardening constants; *C* is the strain rate hardening constant; and *m* is the thermal softening constant. $\bar{\epsilon_p}$ is the equivalent plastic strain. $\dot{\epsilon}^*$ is the dimensionless plastic strain rate defined as the ratio of plastic strain rate $\dot{\epsilon_p}$ to a reference strain rate of $\dot{\epsilon}_0 = 1\ \mathrm{s}^{-1}$ ($\dot{\epsilon}^* = \frac{\dot{\epsilon_p}}{\dot{\epsilon}_0}$). T^* is the homologous temperature defined as $T^* = \frac{T - T_r}{T_m - T_r}$ where *T* is the material temperature, T_r is a reference temperature (usually defined as room temperature), and T_m is the material melting temperature.

Johnson and Cook also implemented fracture criteria based on damage accumulation. Damage *D* is defined by

$$D = \sum \frac{\Delta\bar{\epsilon}_p}{\bar{\epsilon}_p^f} \tag{1.2}$$

where $\Delta\bar{\epsilon}^p$ is the increment of plastic strain accumulated over one numerical integration cycle and $\bar{\epsilon}_p^f$ is the equivalent plastic fracture strain of the material. Once $D = 1$, the material fractures. The fracture strain as a function of stress, strain rate, and temperature is given by

$$\bar{\epsilon}_f^p = [D_1 + D_2 \exp(D_3\sigma^*)][1 + D_4 \ln(\dot{\epsilon}^*)][1 + D_5 T^*] \tag{1.3}$$

D_1, D_2, D_3, D_4, and D_5 are material constants. D_1, D_2, and D_3 scale the fracture strain in such a way that fracture strain decreases as hydrostatic tension increases. The hydrostatic tension is related to the stress triaxiality σ^*, defined as the ratio of mean stress σ_m to von Mises equivalent stress $\bar{\sigma}$ ($\sigma^* = \frac{\sigma_m}{\bar{\sigma}}$). Increasingly positive values of triaxiality correspond to greater hydrostatic tension, whereas increasingly negative values of triaxiality correspond to greater hydrostatic compression. Equation 1.3 only holds for $\sigma^* \leq 1.5$. D_4 and D_5 account for strain rate effects and temperature effects, respectively.

One major disadvantage of the Johnson-Cook model is the decoupled nature of strain hardening, strain rate, and temperature. Each of these variables are independent of one another. Therefore, the model cannot capture any changes in strain hardening behavior due to combined rate and temperature effects. *MAT_224 accounts for this by using tabulated stress-strain curves [5]. Rate-dependent hardening curves based on experimental data are tabulated in the function $k_1(\bar{\epsilon}_p, \dot{\epsilon}_p)$. Temperature dependent hardening curves are tabulated in the function $k_t(\bar{\epsilon}_p, T)$. The effects of strain rate and temperature are then coupled by a new flow stress function:

$$\bar{\sigma} = k_1(\bar{\epsilon}_p, \dot{\epsilon}_p)\frac{k_t(\bar{\epsilon}_p, T)}{k_t(\bar{\epsilon}_p, T_R)} \tag{1.4}$$

Another limitation of the Johnson-Cook model is its assumption that fracture strain exponentially decreases with increasing triaxiality, which is not necessarily true. Bao and

Wierzbicki [10], through mechanical testing of Al-2024, found that equivalent fracture strain exponentially decreased with increasing triaxiality and reached a minimum at $\sigma^* = 0$ (pure shear), increased up to $\sigma^* = 0.4$, then exponentially decreased again in the high triaxiality range. Barsoum and Faleskog [11] addressed this issue by including a deviatoric stress parameter known as the Lode parameter along with stress triaxiality to determine fracture criteria. The Lode parameter μ is defined by

$$\mu = \frac{2\sigma_2 - \sigma_1 - \sigma_3}{\sigma_1 - \sigma_3} \tag{1.5}$$

where σ_1, σ_2, and σ_3 are the principal stresses such that $\sigma_1 \geq \sigma_2 \geq \sigma_3$. Through combined tension and torsion tests of alloyed steel double notched tube specimens, they found that at high stress triaxialities, fracture is driven by void growth and internal necking. At low triaxialities, fracture is driven by void shearing. Therefore, it was concluded triaxiality alone was not sufficient to characterize fracture. A deviatoric stress state parameter was also needed, particularly at low triaxialities. This conclusion supports the findings of Bao and Wierzbicki [10], Wierzbicki et al [12], and Gao and Kim [13]. Wierzbicki et al [12] defined a similar deviatoric stress state parameter *L*, also called the Lode parameter, as

$$L = \frac{27}{2}\frac{J_3}{\bar{\sigma}^3} \tag{1.6}$$

J_3 is the third invariant of the deviatoric stress tensor. This is the definition used in *MAT_224, and is the definition utilized for the remainder of this text.

To account for Lode parameter dependence on fracture, *MAT_224 defines plastic fracture strain as

$$\bar{\epsilon}_p^f = f(\sigma^*, L)g\left(\dot{\epsilon}_p\right)h(T)i(l_c, \sigma^*, L) \tag{1.7}$$

The function *f* defines the plastic fracture strain as a function of triaxiality and Lode parameter. The functions g and h scale the fracture strain according to strain rate and temperature, respectively. The function *i* scales the fracture strain according to the characteristic length of the elements used in the FEM model l_c, triaxiality, and Lode parameter [5]. It is important to note that *MAT_224 defines triaxiality as follows:

$$\sigma^* = -\frac{\sigma_m}{\bar{\sigma}} \tag{1.8}$$

This definition differs by a negative sign from the definition found in most of the literature, but this is the definition that is used going forward since it is the relevant definition for calibration of LS-DYNA's *MAT_224 material model. Therefore, increasingly positive values of triaxiality correspond to increasingly compressive hydrostatic stress, whereas increasingly negative values correspond to increasingly tensile hydrostatic stress.

Under plane stress conditions, it can be shown that the Lode parameter and triaxiality are related via the following cubic function:

$$L = \frac{27}{2}\sigma^*(\sigma^{*2} - \frac{1}{3}) \tag{1.9}$$

Under the plane strain condition, the Lode parameter is zero. These relations are useful when examining the stress space visually, such as in Figure 1.2.

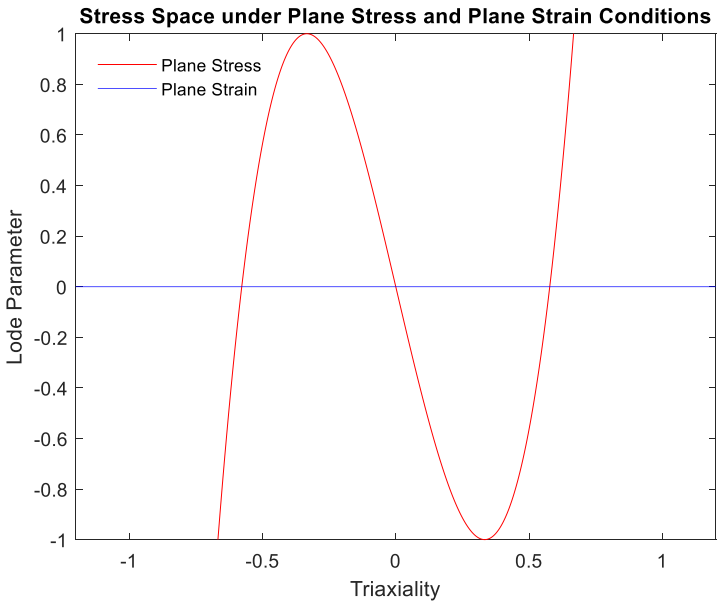

Figure 1.2: Stress space under plane stress and plane strain conditions

Mechanical testing in the high triaxiality range has historically been a challenging task in the field of experimental mechanics. In the traditional plane strain compression test introduced by Watts and Ford [14] and commonly used in many plane strain compression studies [15][16][17], the outer surface is traction free, meaning it is free to expand out-of-plane. Thus, the triaxial stress experienced by elements on this surface is more tension-dominated. Because the outer surface is not in a state of plane strain compression, digital image correlation (DIC), an optical technique used to measure surface displacements, cannot be used to measure full field displacements near the stress state of interest. Also, it is difficult to tell where exactly the fracture would initiate using this test setup. Although this test can provide useful insights into plasticity, it is not an ideal candidate for a fracture test. The typical test setup is illustrated in Figure 1.3.

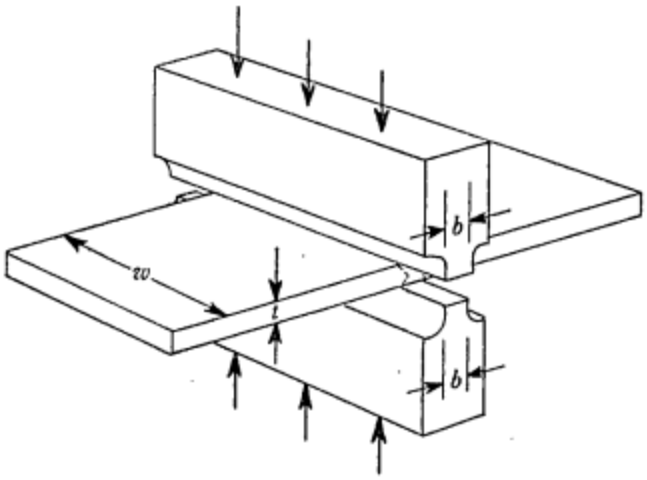

Figure 1.3: Plane strain compression test schematic

Alternative test setups have been used to induce high triaxialities. Wang et al [18] developed an apparatus to test medium-density sands under plane strain compression loading. The cubic specimen was compressed from the sides in a pressure vessel. Axial loading was generated by a servomotor and ball screw system. Tempered glass was used on the front and back of the specimen to prevent out-of-plane displacements. Because the front surface was prevented from displacing out-of-plane and cameras could view the specimen through the glass, plane strain compression was maintained on the outer surface and DIC could be used to measure full-field displacements. This setup is useful for relatively weak and brittle materials with low yield stresses, but impractical for high-strength ductile metals such as Al-2024, Ti64, and In718 due to the large pressures that would be required to deform the specimens and the much higher loads that would be needed to induce fracture.

Kubík et al [19] utilized cylindrical specimens with spherical recesses to find the fracture strains of Al-2024 and AISI 1045 steel under high stress triaxialities. The recess induces high

triaxialities in the center because the specimen deforms inward instead of barreling outward as in a typical cylindrical specimen compression test. Average stress triaxialities and Lode parameters were found through numerical simulations. For the recessed cylinder geometry, average triaxialities of 0.485 and 0.473 were found for AISI 1045 steel and Al-2024, respectively. Average Lode parameters were found to be -0.688 and -0.687 for AISI 1045 steel and Al-2024, respectively. In general, average triaxialities and Lode parameters are computed with respect to equivalent plastic strain, such that

$$\sigma^* = \frac{1}{\bar{\epsilon}_f^p} \int_0^{\bar{\epsilon}_f^p} \sigma^* \mathrm{d}\bar{\epsilon}_p \tag{1.10}$$

$$L = \frac{1}{\bar{\epsilon}_f^p} \int_0^{\bar{\epsilon}_f^p} L \mathrm{d}\bar{\epsilon}_p \tag{1.11}$$

Chapter 2 Experimental Techniques

The experimental specifications for the elliptical backed punch test and notched compression ring experiments are presented. All specimens are fabricated from the same 12.7 mm plate stock used in previous fracture testing for *MAT_224 models [20][21][22][8]. The same plate stock is used to eliminate the potential for variable material properties resulting from manufacturing processes. Tables 2.1, 2.2, and 2.3 summarize the chemical compositions of each material. The In718 plate is precipitate hardened via the procedure shown in Table 2.4.

Table 2.1: Chemical composition of Aluminum 2024-T351

Si	Fe	Cu	Mn	Cr	Zn	Ti	V	Zr	Al
0.08	0.22	4.47	0.59	1.37	0.01	0.18	0.02	0.01	bal

Table 2.2: Chemical composition of Titanium 6Al-4V

Al	V	Fe	O	C	N	Ti
6.64	4.04	0.13	0.19	0.011	0.006	bal

Table 2.3: Chemical composition of precipitate hardened Inconel 718

C	Mn	P	S	Si	Ni	Cr	Mo	Co	Cu	Al	Ti	Cb	B	Fe	Ta
0.048	0.08	0.008	0.0001	0.072	52.6	18.32	2.87	0.2	0.034	0.54	1.02	4.94	0.0029	19.25	0.01

Table 2.4: Heat treatment procedure for precipitate hardened Inconel 718

Description	Time (hours)
Hold constant temp at 718 °C	8
Furnace cool at 55 °C per hour	1.76
Hold constant temp at 621 °C	8

Three-dimensional (3D) digital image correlation (DIC) is integrated into each test. DIC is an optical technique used to measure surface displacements. The relevant functionality of DIC used in this work is described here. A comprehensive overview of DIC can be found in Sutton et al [23]. A contrast is applied to the test specimen surface, typically in the form of a black and white speckle pattern. As a test specimen is deforming, it is photographed. These images are then taken into the DIC software package VIC-3D, where the area of interest in the image is divided into small areas called subsets. A user-defined step size determines the number of pixels between each subset center. A correlation function is implemented that uses the grayscale of each pixel to track the displacements of the subsets. Strains can be derived from these displacements. Since the strains are computed over a very small area, they are smoothed over a group of points using a decay filter worth 10% at the edges. The size of this group of points is defined by the strain filter, another user-defined parameter. Thus, the actual length over which strains are computed is the step size times the strain filter. Multiplying this value by the physical length of each pixel gives the physical length over which strains are computed, known as the virtual strain gauge length (VSGL).

2.1 Elliptical Backed Punch

The experimental design and test procedures for the elliptical backed punch tests are closely modeled after work by Spulak [7][8]. An iterative numerical study is performed in LS-DYNA to select test geometries, and then the tests are conducted using a custom punch test setup in a servohydraulic load frame. In previous work, hemispherical backed punch tests were performed on Al-2024, Ti64, and In718, and elliptical backed punch tests were performed on Al-2024. This study continues this test series by performing elliptical backed punch tests on Ti64 and In718.

The necessary components of the backed punch test setup consist of a rigid punch, a thin specimen plate, and a thin backing plate. The backing plate material should be sufficiently thick, have a lower yield stress, and have higher ductility than the specimen material to ensure it deforms appropriately and does not fracture before the specimen. The backing plate and specimen are clamped together, and then the punch is advanced into the specimen. Figure 2.1 illustrates the basic setup.

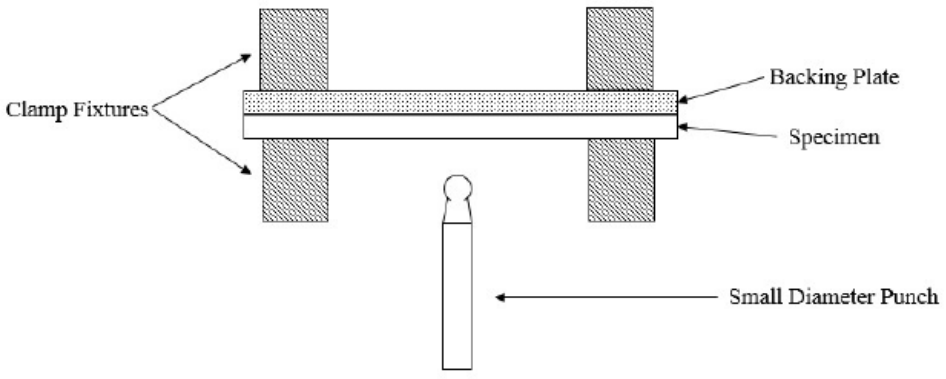

Figure 2.1: Backed Punch Test Schematic

The exact geometries for the punches, specimens, and backing plates are determined via numerical analysis in LS-DYNA. This analysis and justification for the final geometries are explained in section 3.1. The punches used are made of hardened 4340 steel and have elliptical geometries. Both have minor diameters of 2 mm. One has a major diameter of 4 mm, and the other has a major diameter of 6 mm. Drawings are provided in Figure 2.2. The 2x4 mm punch is hardened to about 50 HRC, whereas the 2x6 mm punch is hardened to about 45 HRC.

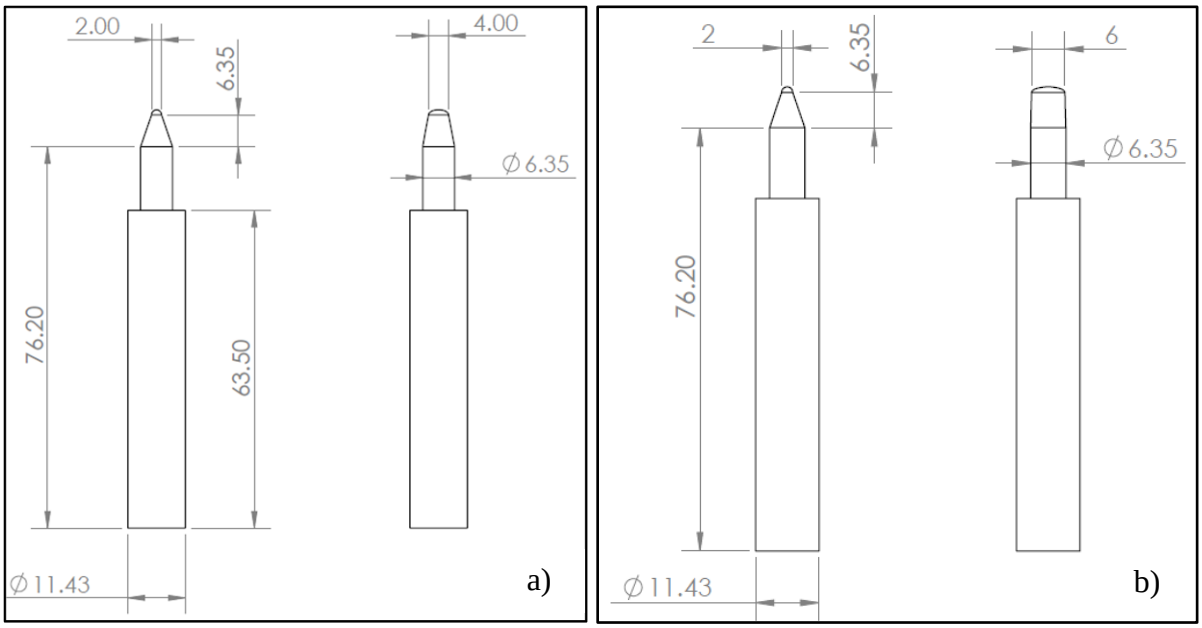

Figure 2.2: a) 2x4 mm Punch Geometry and b) 2x6 mm Punch Geometry

The specimens are manufactured out of the 12.7 mm plate stock using wire electrical discharge machining (EDM). The backing plates are cut out of annealed sheets of 1075 spring steel with a waterjet. The specimen and backing plates are clamped together using bolts and a custom die-clamp fixture. They are designed to have identical side lengths. General dimensions

are shown in Figure 2.3. The only variable dimension is the plate thickness. The side lengths are designed to be as short as possible in an effort to conserve material.

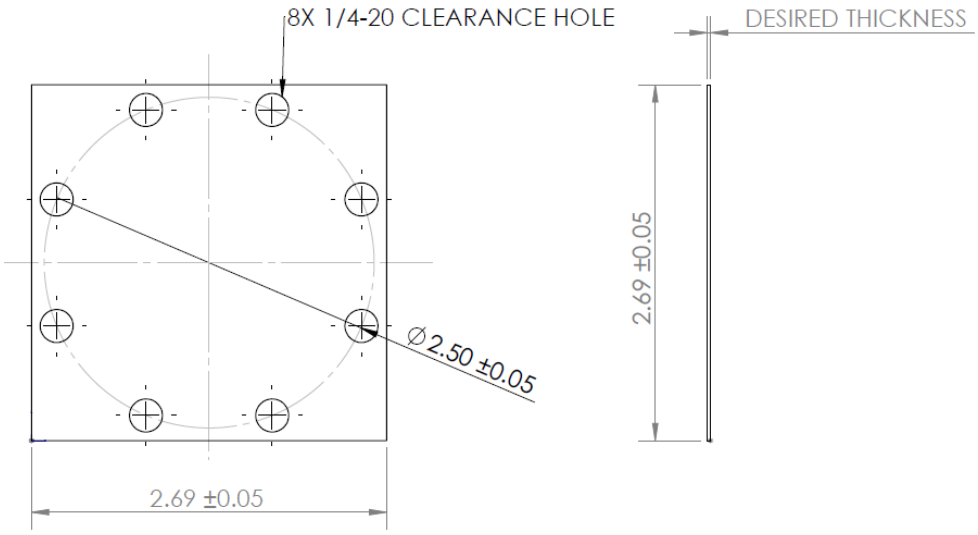

Figure 2.3: Specimen and backing plate dimensions in inches

The tests are conducted using a 250 kN capacity MTS 793 servohydraulic load frame. The entire setup is pictured in Figure 2.4. The custom fixture is fixed in the frame using hydraulic wedge grips. Hydraulic wedge grips are also used to fix the punch to the frame's actuator. Two separate methods are used to load the specimen. Half of the specimens are loaded continuously to fracture, and half are loaded sequentially to fracture. For the continuously loaded tests, the punch is advanced into the specimen at a speed of 0.085 mm/s. The punch is lubricated with Teflon spray. The surfaces in contact between the backing plate and specimen are lubricated with the same Teflon spray. A black and white speckle pattern is spray painted on the back surface of the backing plate for the use of 3D DIC. Two Point Gray Gazelle GZL-CL-41C6M-C digital cameras equipped with 35 mm lenses are used to take images of the specimens throughout

the duration of the tests. Because the view of the specimen back surface is blocked by the backing plate, fracture initiation cannot be observed optically in the continuously loaded tests. To help detect fracture, an acoustic emissions (AE) detection system is integrated into the setup. Two piezoelectric transducers are attached to the test fixture using a rubber band. A small amount of vacuum grease is applied to the transducers to help with adhesion and enhance signal strength. These transducers convert vibrations to voltage signals. The voltage signals are then passed through a preamplifier and into a Micro II PCI-2 AE System. If the magnitude of the signal is greater than a set decibel threshold, the software registers the signal as a "hit." Hits can be used to identify the onset of fracture by examining the associated energy of the hit. Energy, in this context, is defined as the integral of the rectified voltage signal over the duration of the AE hit [24]. Its units are voltage-time. AE hits from external noise not related to fracture can occur during the tests, but these can usually be distinguished from hits related to fracture by examining the energy. Energy from hits due to fracture are typically much larger in magnitude than hits due to other sources of noise.

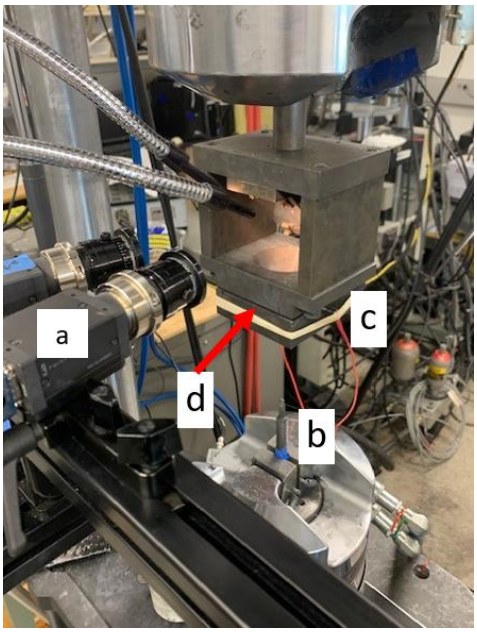

Figure 2.4: Continuous punch test setup: a) cameras, b) punch, c) AE sensors, d) specimen and backing plate (clamped in fixture)

For the sequentially loaded tests, the back surface of the specimen is spray painted with a black and white speckle pattern instead of the backing plate. This allows for 3D DIC on the specimen back surface. To protect the speckle pattern from degrading due to contact with the backing plate, a thin layer of clear M-Bond 200 cyanoacrylate strain gauge adhesive is applied over the spray paint after allowing at least 24 hours for the paint to cure. The punch is advanced 0.254 mm into the specimen at a rate of 0.085 mm/s. The punch is then retracted, and the specimen is removed from the test fixture. The specimen is placed in a separate fixture where the same Point Gray Gazelle cameras with polarizing filters are positioned to capture an image of the back surface. A polarized light source is used to illuminate the specimen. The polarized filters and light source reduce the effect of glare caused by the Teflon spray used to lubricate the

specimen. This loading and unloading process is repeated until fracture is observed. Observing the initial fracture usually requires viewing the specimen under a microscope. AE detection is not used for these tests. Figure 2.5 shows the sequential test setup.

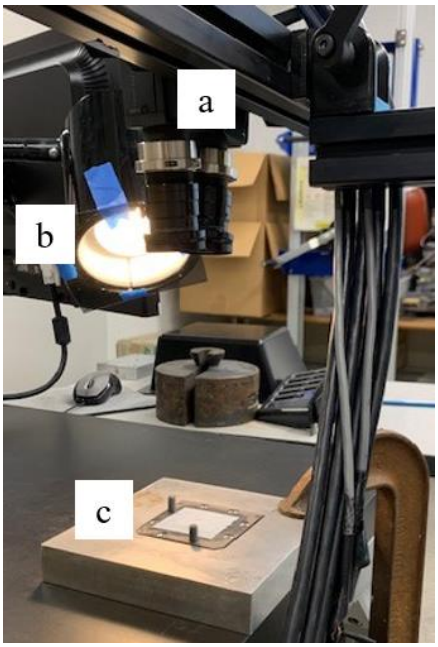

Figure 2.5: Sequential punch test setup: a) cameras, b) polarized light source, and c) specimen

2.2 Notched Compression Ring

The notched compression ring experiment is first performed on Al-2024 after it was designed through numerical analysis at George Mason University (GMU) [25]. After the initial experiments, additional numerical analyses are performed to compare the Al-2024 tests to experiments and design similar tests for Ti64 and In718. Additional tests are then conducted on all three materials.

The Al-2024 geometry designed at GMU is shown in Figure 2.6. Various manufacturing methods are used to machine the specimens. The most efficient method used is wire EDM to cut out cylindrical ring blanks through the thickness of the 12.7 mm plates, followed by turning on a lathe to cut the notches.

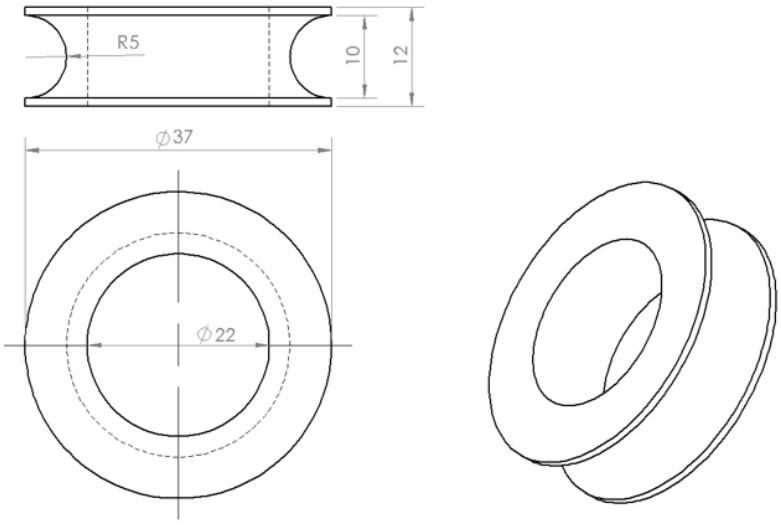

Figure 2.6: Al-2024 notched compression ring original design (dimensions in mm)

The ring is placed between two tungsten carbide platens fixed to the same MTS 793 servohydraulic load frame used in the backed punch tests. Steel platens are also used for some of the tests, but tungsten carbide is preferred due to its higher stiffness. The loads seen in these tests are very high, and this can cause the more compliant steel platens to experience some plastic deformation, particularly when testing In718. A black and white speckle pattern is spray painted on the front of each specimen to allow the use of DIC. The surfaces in contact between the rings and the platens are lubricated with grease. The actuator compresses the specimen at a rate of 0.005 mm/s for the initial tests. The rate is increased to 0.010 mm/s in later tests. The tests are

carried out until a significant drop in the measured load is observed. In later tests, AE sensing is implemented using the same system described in section 2.1. Two Point Gray Gazelle GZL-CL-41C6M-C digital cameras equipped with 50 mm lenses are used to take images for 3D DIC. The setup is shown in Figure 2.7.

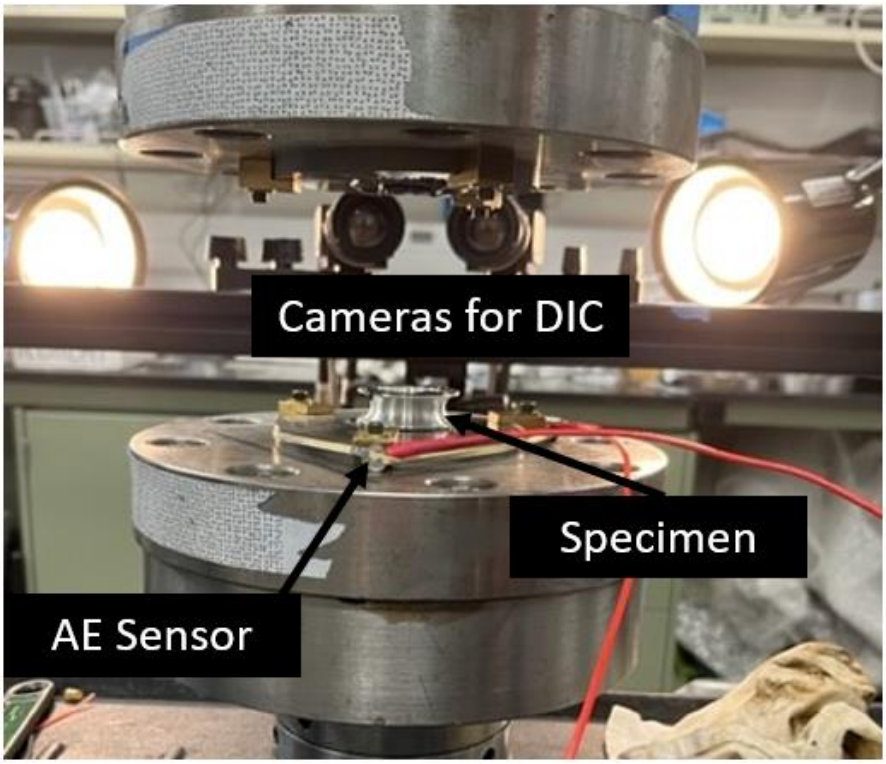

Figure 2.7: Notched compression ring test setup

Chapter 3 Numerical Analysis

3.1 Elliptical Backed Punch

Numerical analysis in LS-DYNA is performed to select test geometries that induce stress states within the unpopulated regions of the fracture surfaces of Ti64 and In718. The test is modeled using quarter symmetry with 0.15 mm constant stress hexahedral solid elements with reduced integration. The punch and clamps are modeled as rigid materials using LS-DYNA's *MAT_020 material model. Nodal displacements and rotations in the normal directions of the symmetry surfaces are constrained to maintain quarter symmetry. The outer circumferential surface nodes are all fixed to mimic the clamped boundary condition in the test. The clamps are fixed in place. The punch is assigned a prescribed motion in the direction normal to the specimen surface and constrained in all other directions. All contacts are modeled using the *CONTACT_AUTOMATIC_SURFACE_TO_SURFACE card with no friction since the punch-specimen and specimen-backing plate interfaces are lubricated during the tests. Figure 3.1 displays the mesh.

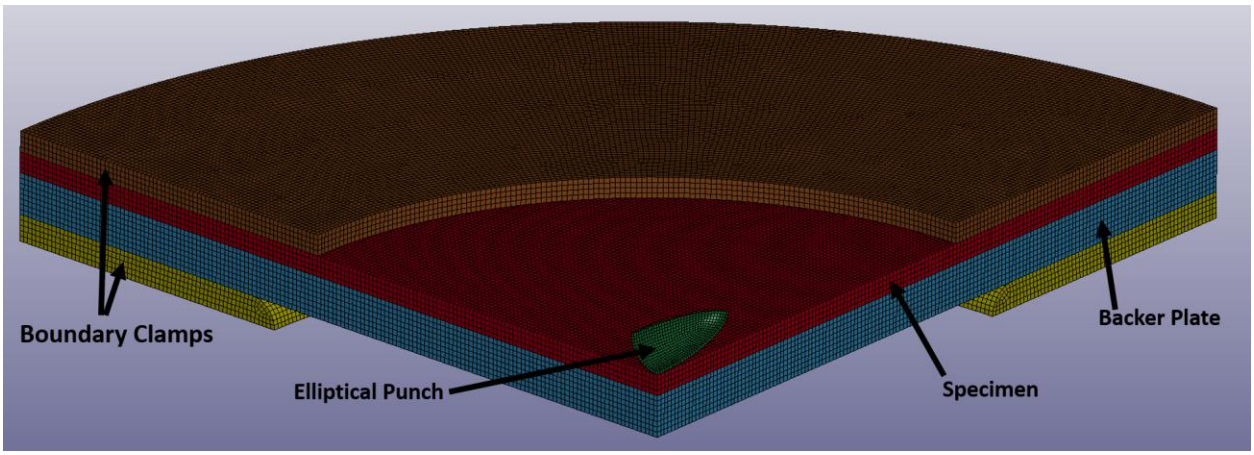

Figure 3.1: Sample backed punch test quarter symmetric simulation

The initial design simulations are conducted using *MAT_024, a piecewise linear plasticity model, for the specimen and backing plate. The specimen materials of interest are Ti64 and In718. AISI 1075 steel is used as the backing plate material for both specimen materials. Elastic constants and densities used for these materials are summarized in Table 3.1.

Table 3.1: Elastic constants and yield stresses of simulated materials

Material	Elastic Modulus (GPa)	Poisson's Ratio	Yield Stress (MPa)	Density (kg/m^3)
Ti64	110	0.342	718.15	4430
In718	210	0.29	996.68	8190
1075 Steel	200	0.29	342.51	7850

The post-yield behavior of each material is derived from stress-strain data from uniaxial tests using the process outlined in Park et al [5]. The stress-strain curves derived previously in the development of *MAT_224 models of Ti64 and In718 [21][22][26][27] are used. Uniaxial tension data is used to derive the In718 curve. Two separate curves are used to model the Ti64 behavior: one derived from uniaxial tension data and one from uniaxial compression data. Ti64 exhibits asymmetric behavior in tension versus compression. Because this test induces combinations of tension and compression, both curves are tested to determine which produces a better match to the test data. In the interest of time and to match previous work [8], the design simulations only utilize the compression curve for Ti64. Tension tests were performed on annealed 1075 steel by Spulak [8] and used to derive the material's post-yield behavior. The uniaxial tension tests were simulated using the *MAT_024 models, and the true stress-strain responses are shown in Figure 3.2.

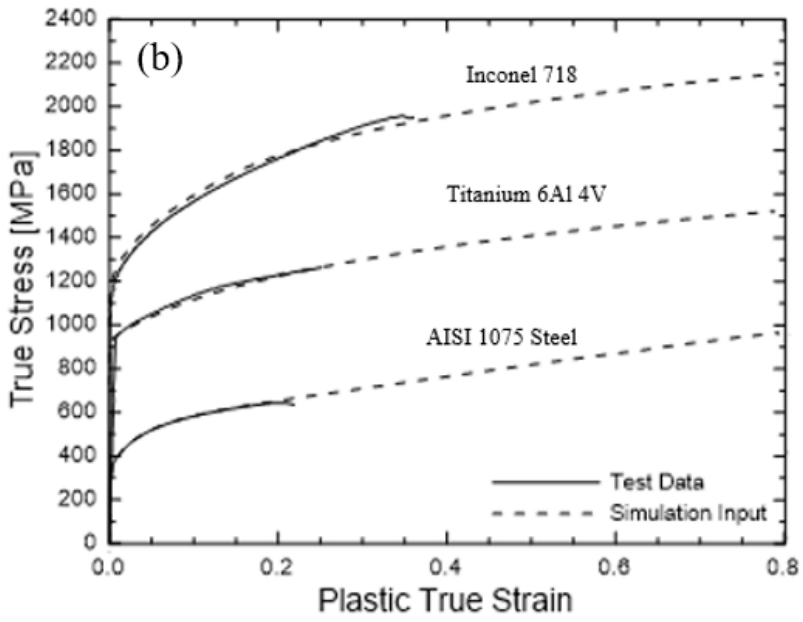

Figure 3.2: Plastic stress-strain responses for materials used in the backed punch tests (Ti64 curve is derived from compression data)

Simulations with varying specimen and backing plate thicknesses are performed. The evolution of stress state on the center element on the back surface of the specimen is examined and compared for each simulation. The goal is to obtain triaxialities between -2/3 and 1/3 and Lode parameters roughly between -1 and 0. It is also desirable to keep the values of triaxiality and Lode parameter as constant as possible throughout the duration of the test. It is impossible to obtain a perfectly constant triaxiality and Lode parameter for the entire duration of the test, but keeping them relatively consistent makes the data more useful for calibrating the fracture surfaces in the numerical models. The Lode parameter is found to be more variable than the triaxiality. It always starts at -1, increases a bit, and then shows some oscillatory behavior for the remainder of the loading. The Lode parameter should be -1 for a state of axisymmetric

compression. This is why the Lode parameter remains -1 for the entire duration of hemispherical backed punch tests. The elliptical punch geometry appears to initiate axisymmetric out-of-plane compression at the start, but the eccentricity of the punch causes the Lode parameter to be drawn away from a value of -1 as the punch advances and deviatoric stresses are more pronounced. Accepting the variability of the Lode parameter, the focus of the design turns to maintaining relatively constant triaxiality. With thicker backing plates, variation in triaxiality increases. Thicker backing plates induce more out-of-plane compression, leading to higher initial triaxialities. However, as the test progresses and deformations become larger, in-plane tension begins to dominate, and the triaxiality falls back into the negative region of stress space. An example of this behavior on a Ti64 simulation is shown in Figure 3.3. The triaxiality increases to about 0.3, which corresponds to uniaxial compression. It then decreases to around -0.4. This high variability makes it practically difficult to implement this data into a ductile fracture model since the data needs to be somehow translated to a point on a fracture surface.

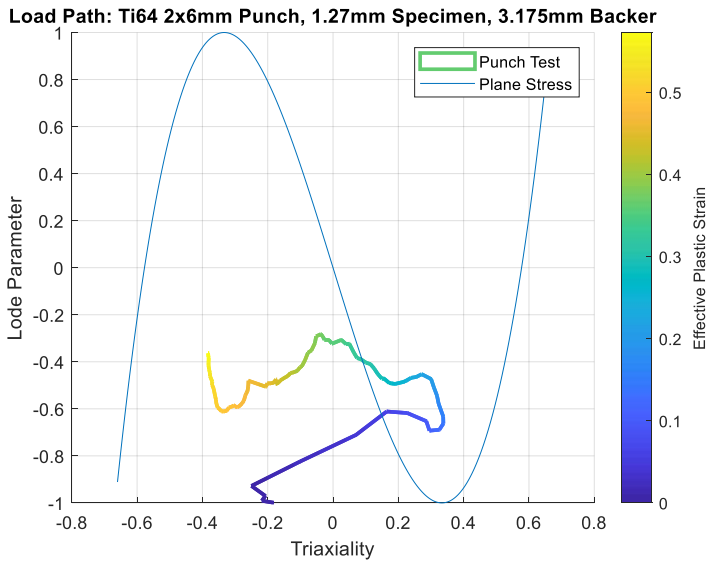

Figure 3.3: Load path for Ti64 specimen with backer plate to specimen thickness ratio of 2.5

Another target of the design is to keep the load path as far from the left side of the plane stress curve as possible. Previous fracture test series [21][22] have produced data along this curve, so obtaining data in a new, more sparsely populated area of the fracture surface would be more useful for calibrating Ti64 and In718 material models. Test geometries are selected based on these criteria and shown in Table 3.2. The geometries and load paths of these designs are shown in Figures 3.4-3.6 with previous fracture test points overlaid. A comprehensive list of the load paths from each simulation is in Appendix A.

Table 3.2: Selected Punch Test Geometries

Material	Punch Geometry (mm)	Specimen Thickness (mm)	Backing Plate Thickness (mm)
Ti64	2x6	0.635	1.27
Ti64	2x6	1.27	1.575
In718	2x4	0.635	0.889

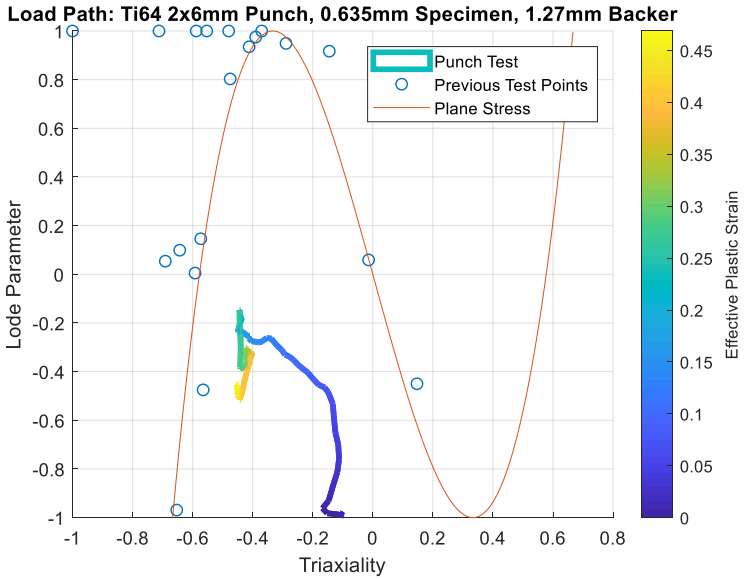

Figure 3.4: Load path with previous fracture test points overlaid for 0.635 mm (thin) Ti64 specimen

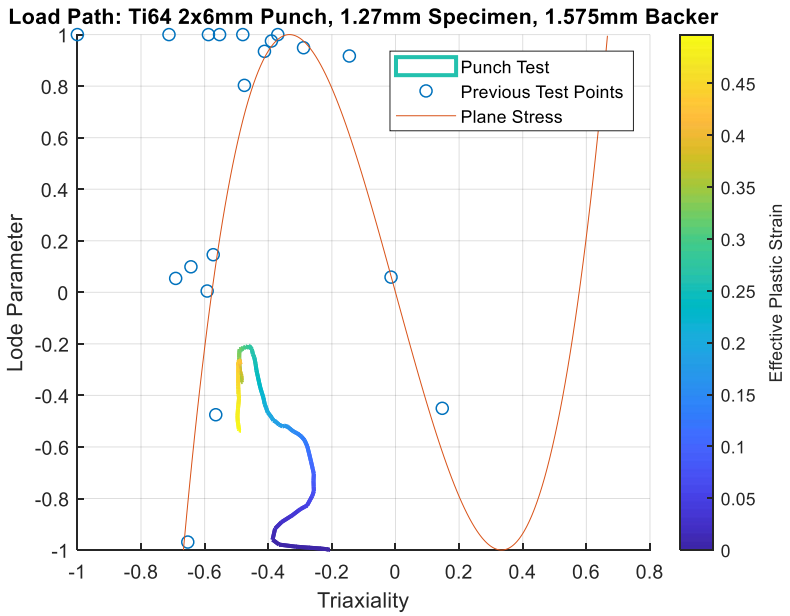

Figure 3.5: Load path with previous fracture test points overlaid for 1.27 mm (thick) Ti64 specimen

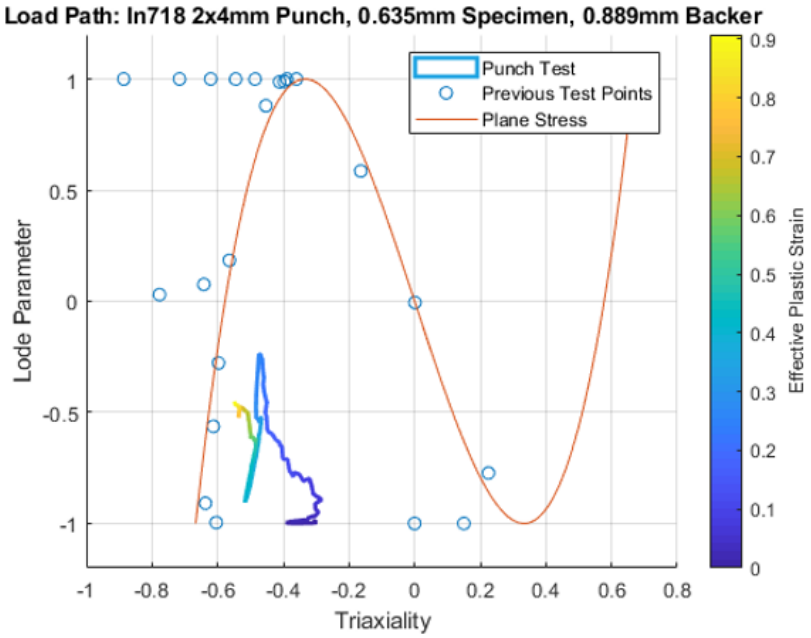

Figure 3.6: Load path with previous fracture test points overlaid for 0.635 mm In718 specimen

3.2 Notched Compression Ring

The notched ring concept is extended to Ti64 and In718 after reviewing numerical analysis done at GMU for Al-2024. The first steps are to ensure the specimens converge to the desired stress state ($\sigma^* \approx 0.6$, $L \approx 0$) in the center and that the load levels are within the practical range of the MTS Model 661 22H-01 force transducer used in the tests, which is rated for up to 250 kN. The primary variable that affects load level is the inner diameter, which determines the minimum wall thickness of the specimen. Various wall thicknesses are modeled using the full specimen geometry with 0.15 mm solid elements. For Ti64, constant stress solid elements with reduced integration are used. For In718, fully integrated solid elements are used. The choice in element formulation is based on the recommendations for each material's respective *MAT_224 model. Material model calibration for Ti64's *MAT_224 was done using constant stress solids with reduced integration. For In718, material model calibration for *MAT_224 was done using fully integrated solids. To ensure consistent results, the same element formulations used in the calibration should be used in any application. The same Ti64 and In718 *MAT_024 models used in the punch test simulations are used to model the specimen materials. Only the Ti64 compression curve is used, as this test induces a highly compressive state of stress. Platens are used to compress the specimen and are modeled as rigid using *MAT_20. The top platen is fixed in place, and the bottom is fixed in every direction except the direction of axial displacement. A prescribed velocity of 5000 mm/s is applied on the bottom platen in this direction to compress the specimen. The loading rate is high to decrease simulation run times. Simulations are also conducted at lower and higher rates, and it is determined that 5000 mm/s is the highest rate that

can be used before results differ due to inertial effects. The contacts are frictionless, as the specimen-platen contact surfaces are lubricated during the tests. Figure 3.7 displays the mesh.

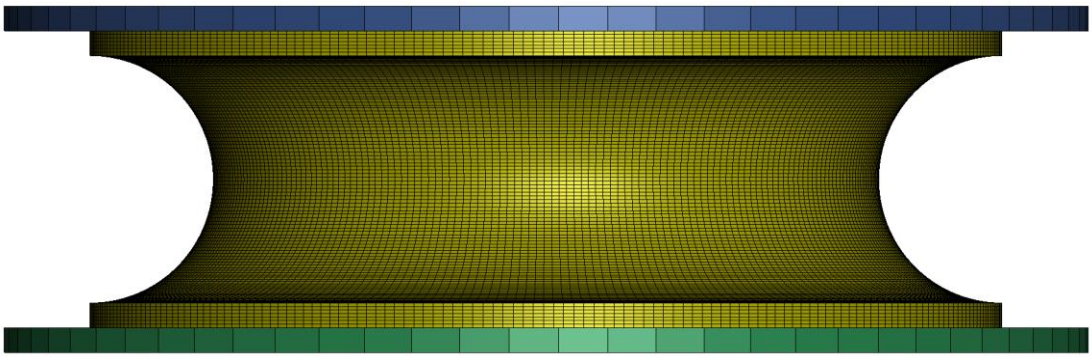

Figure 3.7: Sample notched ring full simulation mesh

The drawings in Figures 3.8 and 3.9 show the chosen final geometries after testing geometries with wall thicknesses of 1 mm, 1.25 mm, 1.5 mm, 1.75 mm, and 2 mm for each material in simulation. The chosen Ti64 and In718 specimen geometries have minimum wall thicknesses of 1.5 mm and 1.25 mm, respectively. It should be noted that specimens with 1 mm wall thickness are also physically tested. In a Ti64 test with 1 mm wall thickness, fracture is observed on the inner part of the ring, as shown in Figure 3.10. Fracture likely occurs on the outer circumference first and then propagates through the thickness at about 45°, which is consistent with failure in shear. Nevertheless, a thicker wall is used for both Ti64 and In718 to protect against severe buckling and fracture in undesirable regions of the specimen.

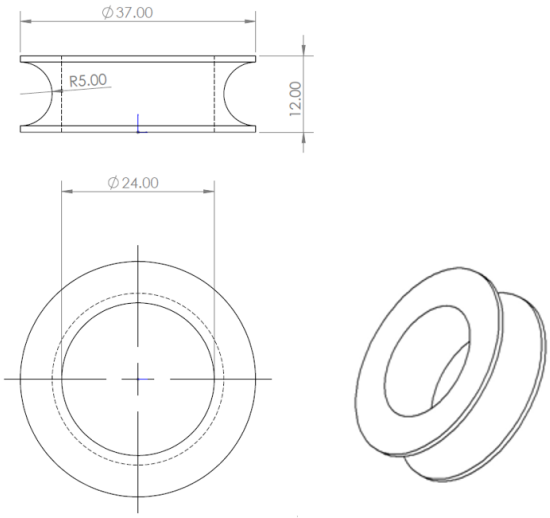

Figure 3.8: Ti64 notched compression ring specimen (dimensions in mm)

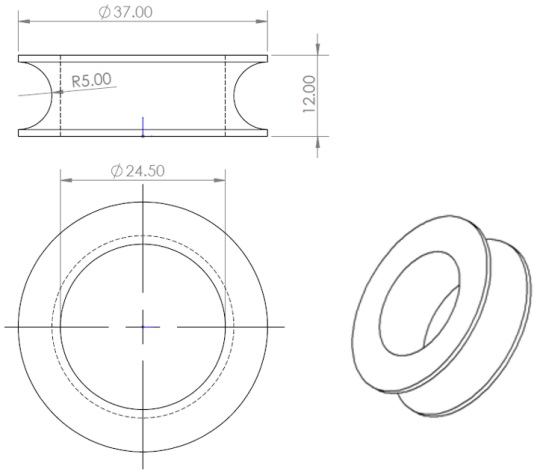

Figure 3.9: In718 notched compression ring specimen (dimensions in mm)

Figure 3.10: Fracture on inner ring surface on Ti64 specimen with 1 mm wall thickness

To confirm the specimen geometry with a 1.25 mm wall thickness would not induce too much buckling, the damage accumulation is compared on the inner ring surfaces. In order to track damage accumulation, fracture strains had to be considered. Thus, the *MAT_224 models of Ti64 and In718 available on the Ansys AWG website [28] are used to model the specimen's fracture behavior, but the same stress-strain curves are used to model plasticity. It should be noted the In718 model is not publicly available at the time of this writing. In Figure 3.12, the damage is plotted over time along a slice of elements in the highly damaged region of the inner ring surface as shown in Figure 3.11. The damage accumulation plots clearly indicate a reduction in maximum damage in Ti64 from 0.90 to roughly 0.57 when transitioning from the 1 to the 1.5 mm wall. The damage is not nearly as high in the In718 specimen with a 1 mm wall, but the wall thickness is increased to 1.25 mm anyway to be conservative. Increasing the thickness of the

In718 specimen to 1.5 mm would have generated loads greater than the 250 kN threshold, which is why a 1.25 mm wall is chosen instead. The force-displacement responses predicted by the *MAT_024 simulations for the notched ring tests are shown in Figure 3.13.

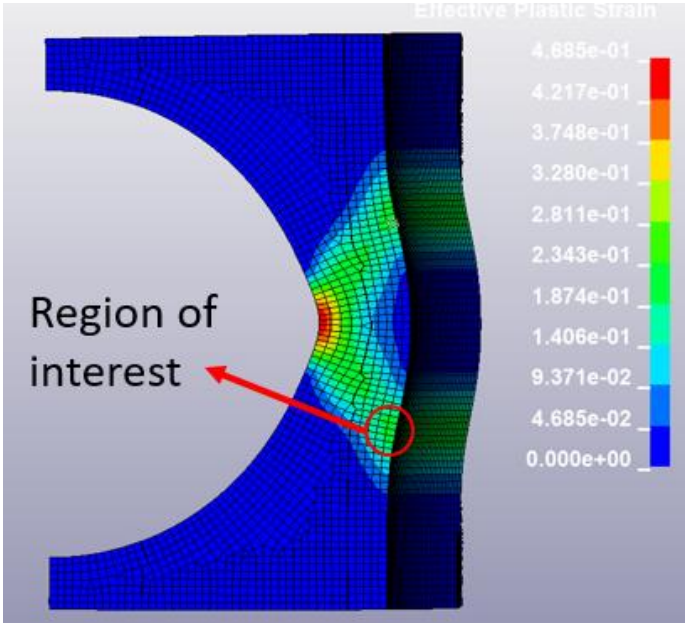

Figure 3.11: Region of interest for damage accumulation

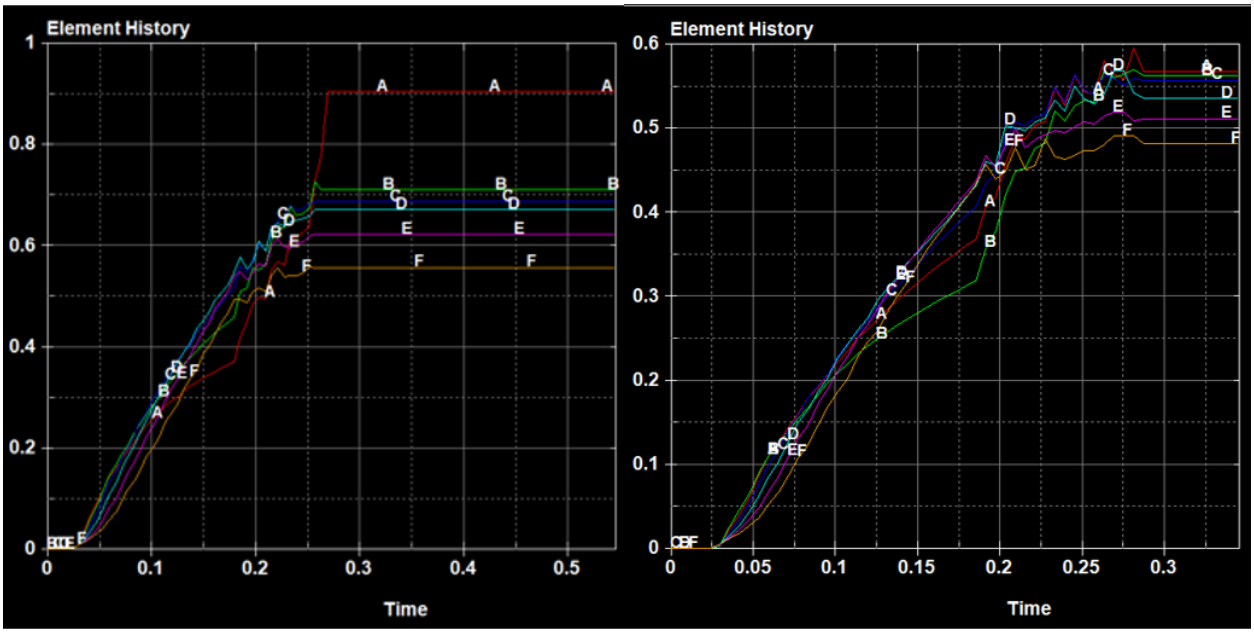

Figure 3.12: Ti64 damage accumulation on inner surface of specimens with 1 mm wall (left) and 1.5 mm wall (right)

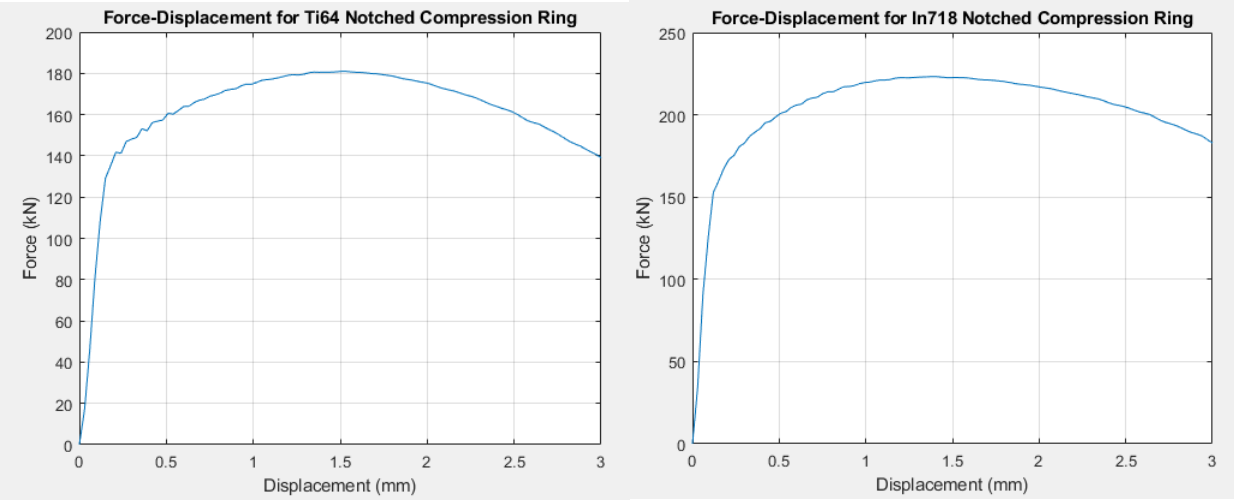

Figure 3.13: Simulated force-displacement responses for Ti64 (left) and In718 (right) notched compression rings

The stress state analysis is done through mesh convergence studies. Symmetry is exploited by only modeling a cross-section of the specimen with volume weighted axisymmetric solid quadrilateral elements, as shown in Figure 3.14. Mesh sizes used are 0.15, 0.10, 0.05, and 0.025 mm. The *MAT_024 material models are once again used to model the specimen, and the platens are modeled as rigid.

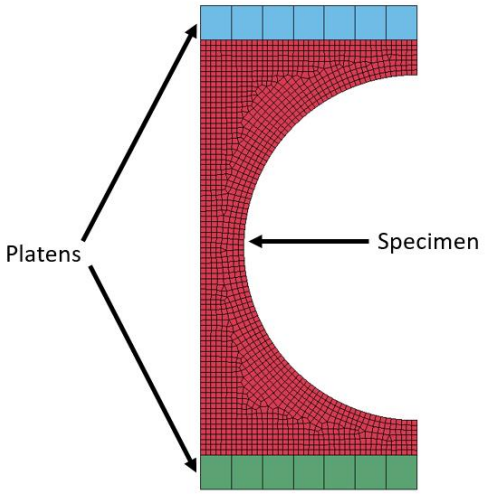

Figure 3.14: Sample notched ring axisymmetric mesh

The state of stress at the center element tends to become unstable at large strains. The triaxiality and Lode parameter remain relatively constant at values near 0.6 and 0, respectively, for the majority of the simulation times. However, both the triaxiality and Lode parameter begin to exponentially increase near the end of the simulations. As element size decreases, the onset of instability is delayed. This trend is illustrated in Figures 3.16-3.23. High element distortion coupled with severe buckling, as shown in Figure 3.15, likely causes the unstable state of stress. The localized deformation in the center requires small elements to properly capture the material

behavior. Thus, it is desirable for the test specimen to fracture before the onset of the localized element distortions. From this information, it can be reasonably concluded that the physical state of stress experienced at the center of the specimen has an approximately constant triaxiality near 0.6 and an approximately constant Lode parameter near 0, at least until the onset of high local strains in the center of the specimen. As long as fracture in the tests occurs before the onset of instability in the simulation, the fracture strain can reliably be determined.

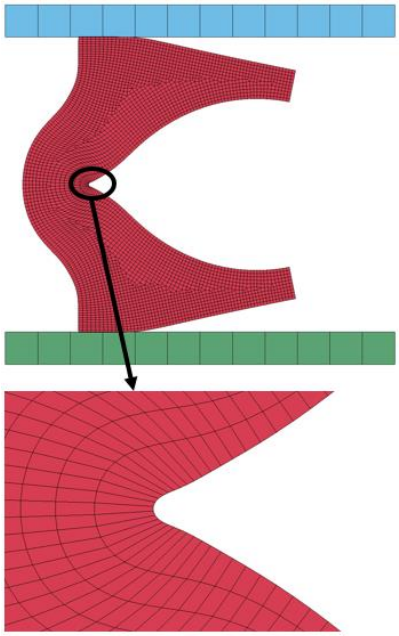

Figure 3.15: Deformed specimen. Elements in center are clearly distorted.

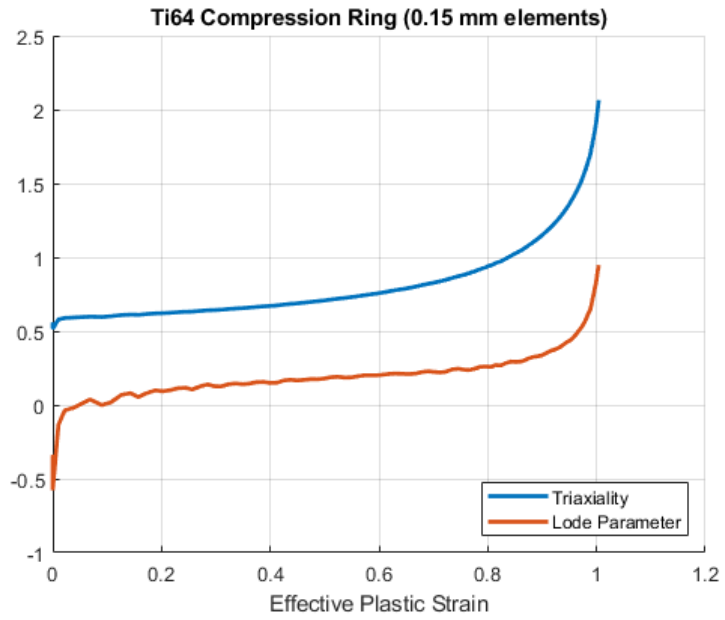

Figure 3.16: Stress state parameters for Ti64 notched ring with 0.15 mm elements

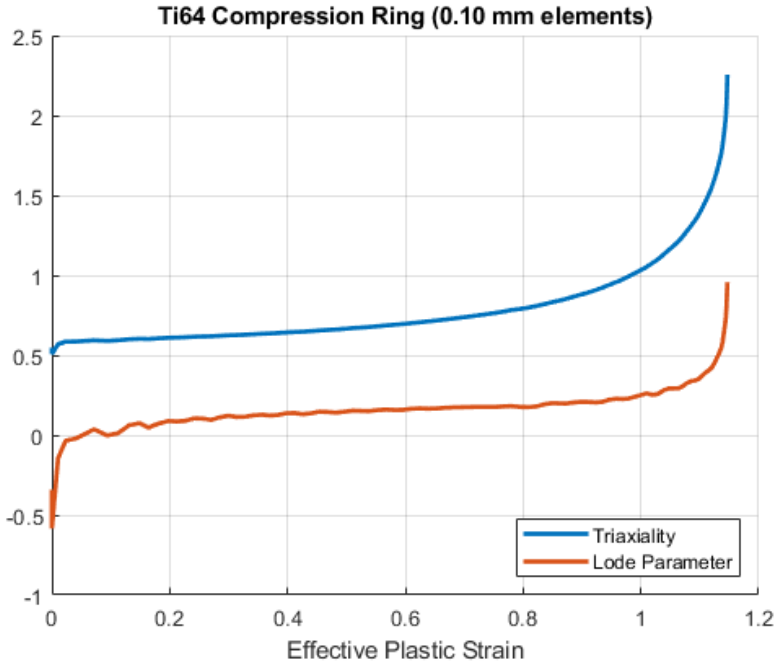

Figure 3.17: Stress state parameters for Ti64 notched ring with 0.10 mm elements

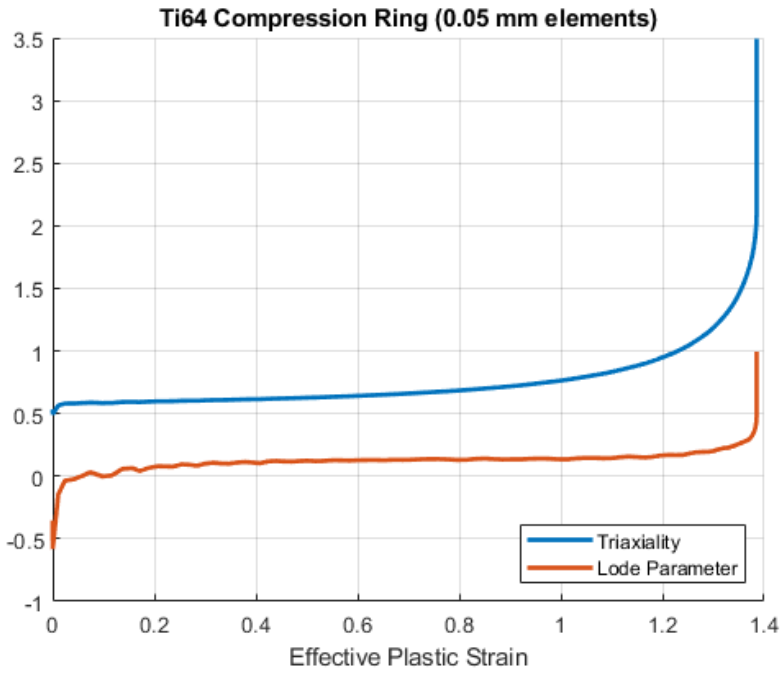

Figure 3.18: Stress state parameters for Ti64 notched ring with 0.05 mm elements

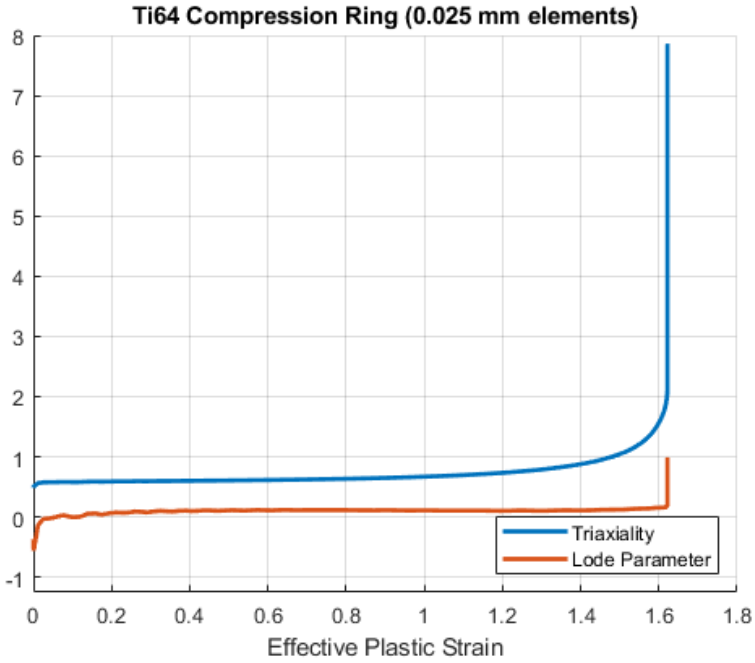

Figure 3.19: Stress state parameters for Ti64 notched ring with 0.025 mm elements

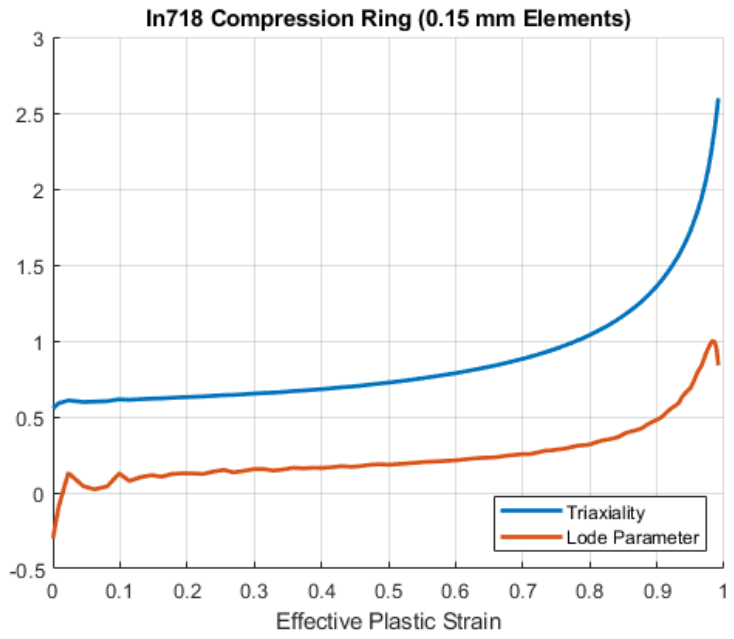

Figure 3.20: Stress state parameters for In718 notched ring with 0.15 mm elements

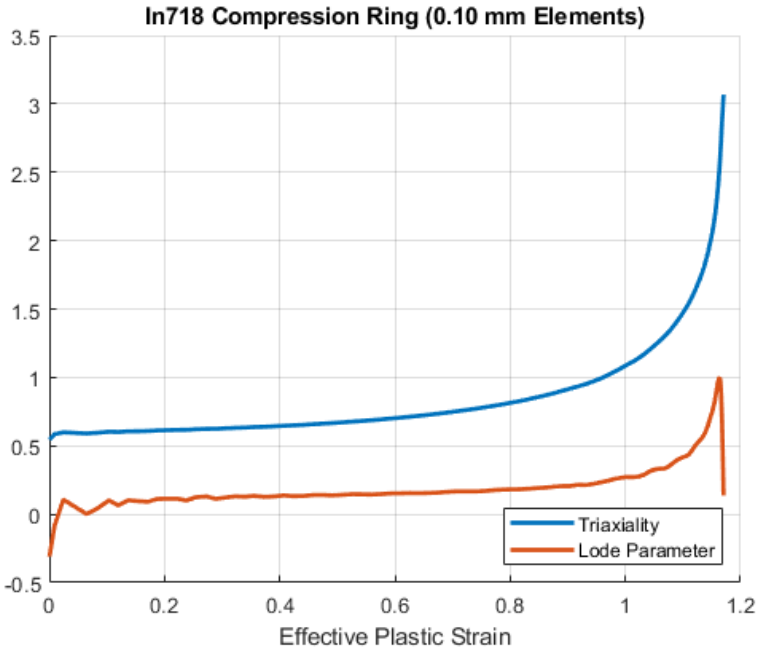

Figure 3.21: Stress state parameters for In718 notched ring with 0.10 mm elements

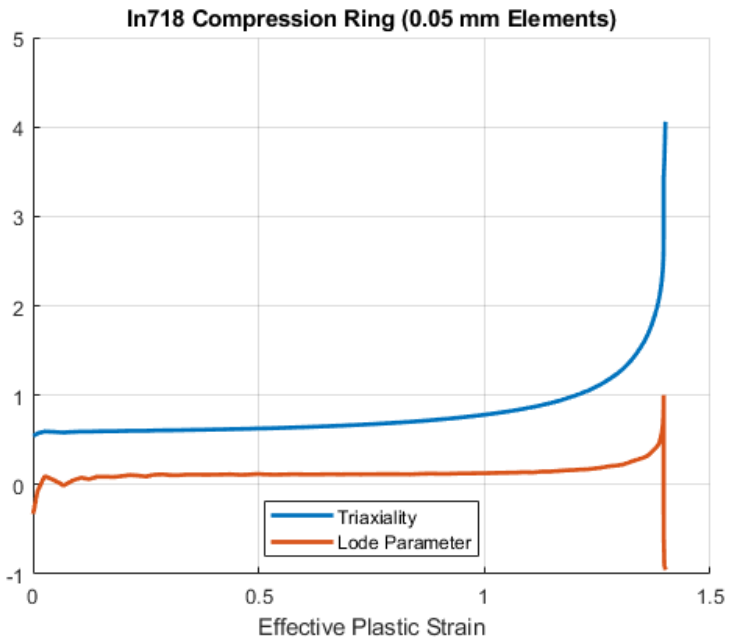

Figure 3.22: Stress state parameters for In718 notched ring with 0.05 mm elements

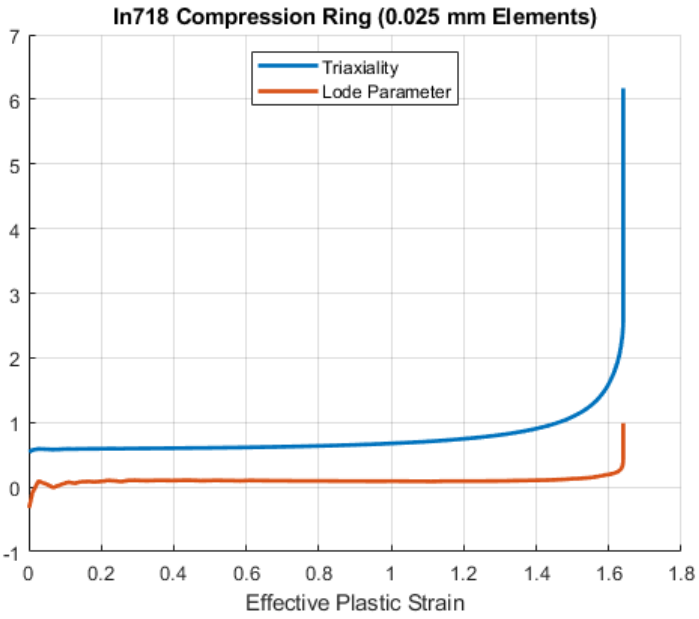

Figure 3.23: Stress state parameters for In718 notched ring with 0.025 mm elements

An Al-2024 notched ring numerical model is also created to compare with test data. The material model is derived from uniaxial tension data in the same manner as the Ti64 and In718 *MAT_024 models referenced in section 3.1, and the properties are displayed in Table 3.3. A mesh convergence study is not necessary, as this was previously performed at GMU [25]. A full simulation is constructed using the same mesh and boundary conditions as the Ti64 and In718 models.

Table 3.3: Al-2024 elastic properties

Material	Elastic Modulus (GPa)	Poisson's Ratio	Yield Stress (MPa)	Density (kg/mm^3)
Al-2024	70	0.339	381.19	2600

Chapter 4 Results and Discussion

The numerical and experimental results are both used to estimate the equivalent plastic strain to fracture under the states of stress induced by the elliptical backed punch and notched compression ring tests. An approach similar to work by Spulak [8] and Seidt et al [29] is used. Strain and force-displacement response data from both tests and simulations are compared along with local strain data near the fracture locations. If the tests agree with the simulation, then the plasticity model used in simulation is considered accurate. Once the plasticity model is confirmed to be accurate, the triaxiality, Lode parameter, and equivalent plastic strain extracted from simulation are assumed to represent the physical phenomena present in the tests. This assumption is necessary since the stress state parameters cannot be directly measured. Although the plastic strain at the fracture location can be estimated from displacements measured through DIC in some instances, it is generally considered best practice to take the simulated plastic strain value at fracture as the fracture strain, even if it differs slightly from the test value. This ensures consistency when calibrating the fracture surface in the material model. The fracture strain in simulation should correspond with the same load and displacement observed at fracture in the tests.

Average stress state parameters weighted with respect to the equivalent plastic strain increments are computed and used to estimate the point on the fracture surface where the fracture strain corresponds to. This is not necessarily the most accurate way to calibrate a stress-state dependent fracture model, particularly when the triaxiality and Lode parameter vary significantly throughout the experiment, such as in the backed punch tests. Monitoring the damage accumulated through each increment in the load path and ensuring damage reaches unity at the

point fracture occurs in the tests would provide the most accurate way to model fracture for a particular load path. However, using average stress state parameters is a much simpler approach that provides generalized insight into the performance of current *MAT_224 fracture models near the stress states of interest without the need for a more time-consuming numerical study. In the case of the notched rings, the stress state remains relatively constant throughout the duration of the tests. Thus, the value of the equivalent plastic fracture strain should remain relatively constant throughout the test duration. The damage accumulates under a constant state of stress for each time step, allowing for a more direct comparison to the fracture surfaces.

Certain precautions must be taken when comparing strains between DIC test data and LS-DYNA simulations. First, the Hencky strain tensor is used for all DIC strain computations in this work. However, LS-DYNA does not currently allow a Hencky strain tensor output. Instead, the software stores the corotational integral of the strain rate tensor. This is equal to the symmetric part of the velocity gradient. These two definitions are identical for the cases of uniaxial tension and compression. However, the two definitions are not comparable in general, especially in cases with large shear strains or large rotations. Because the backed punch and notched compression ring tests do not exhibit large shear strains or large rotations at the fracture locations for the coordinate systems defined in simulation and DIC, the measured DIC and simulated strain values can be reliably compared. Furthermore, the virtual strain gauge length (VSGL) and element size should match when comparing measured and simulated strains. This ensures the strains are computed over the same physical area in the tests and simulations. To account for this, all simulated strains are averaged over an appropriate number of elements to match the area the elemental strains are computed over to the VSGL.

Other strain outputs of interest for both experiments are the three principal strains: ϵ_1, ϵ_2, and ϵ_3. VIC-3D outputs two in-plane principal strains. The third principal strain can be found by assuming material incompressibility during plastic deformation, which means the trace of the strain tensor must be zero. This also assumes negligibly small elastic strains. Therefore,

$$\epsilon_3 = -(\epsilon_1 + \epsilon_2) \tag{3.1}$$

From these principal strains, the equivalent plastic strains from the test can be computed. The equivalent plastic strain is defined as

$$\bar{\epsilon_p} = \int d\bar{\epsilon}_p dt = \int \sqrt{\frac{2}{3} d\epsilon_{ij}^p d\epsilon_{ij}^p} dt \tag{3.2}$$

where $d\epsilon_{ij}^p$ is the plastic strain increment tensor. This is computed incrementally over each time integration cycle. Using a strain increment tensor derived from the principal strains,

$$\bar{\epsilon_p} = \sqrt{\frac{2}{3}} \int \left(\left(\frac{d\epsilon_1}{dt}\right)^2 + \left(\frac{d\epsilon_2}{dt}\right)^2 + \left(\frac{d\epsilon_3}{dt}\right)^2 \right)^{1/2} dt \tag{3.3}$$

This claim is technically only valid for the sequentially loaded punch tests. Whenever a principal strain is computed by DIC in the sequentially loaded tests, it is necessarily due to plastic deformation. In general, principal strains incorporate both elastic and plastic strain. However, strains computed in the actual tests are derived from the material in an unloaded state. Therefore, all of the elastic strains are inherently eliminated. For the notched rings, the elastic strains are not eliminated because these tests are loaded continuously. However, they are much smaller than the plastic strains, so the influence of elastic strains in the tests is negligible.

4.1 Elliptical Backed Punch

The force-displacement responses for the elliptical backed punch tests are plotted in Figures 4.1-4.3. The repeated drops in load observed in the sequentially loaded test data are due to the unloading and reloading of the specimen.

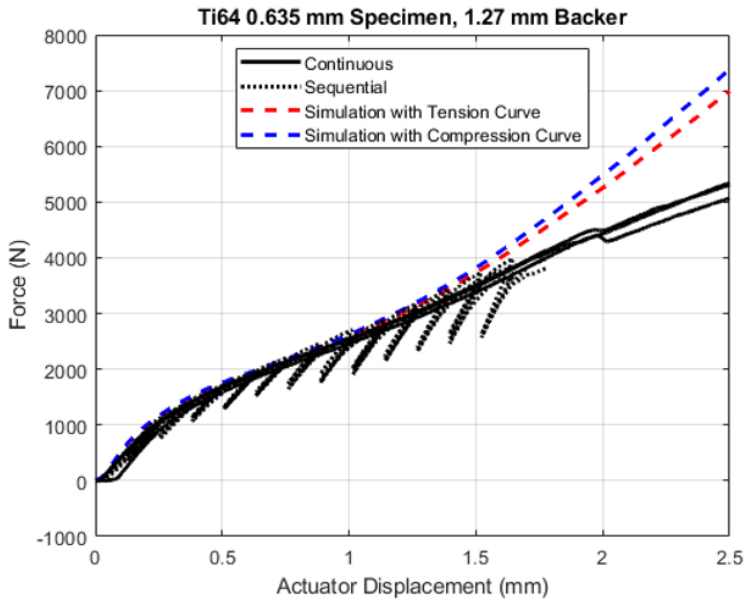

Figure 4.1: Force-displacement responses for the Ti64 thin specimen test

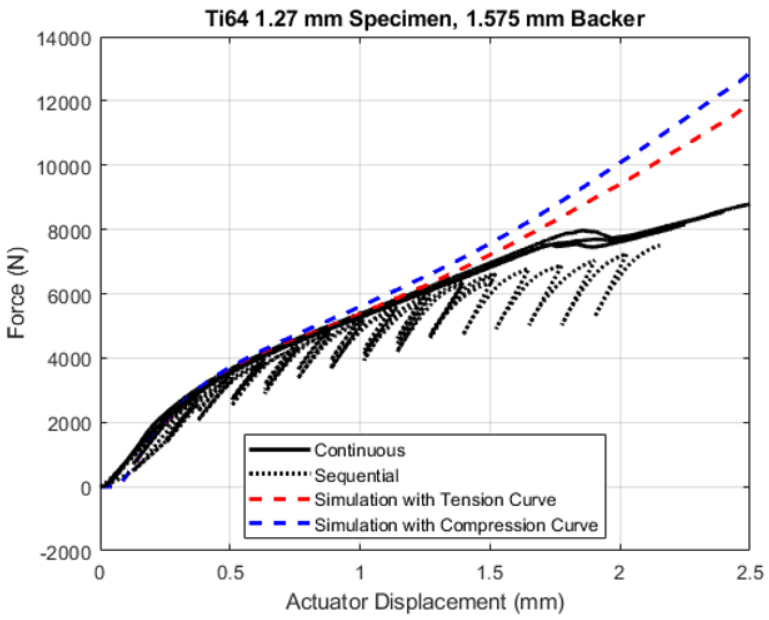

Figure 4.2: Force-displacement responses for the Ti64 thick specimen test

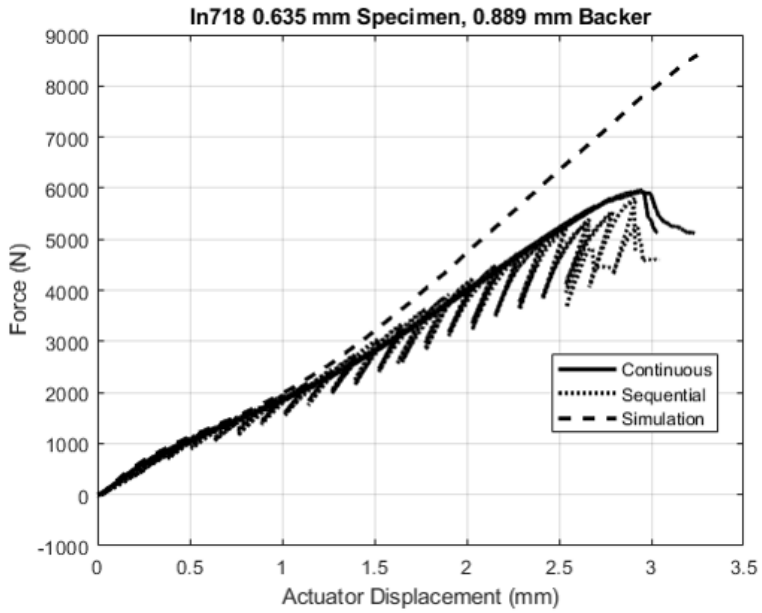

Figure 4.3: Force-displacement responses for In718 test

Figure 4.2 shows one thick Ti64 sequential test is carried out well beyond initial fracture. The load is clearly lower in this test after initial fracture than the continuous tests. It is hypothesized that the initial fracture occurs near the same displacement in the continuous tests compared to the sequential tests, and the load drops seen in the continuous tests are caused by more catastrophic crack propagations. To test this hypothesis, additional continuous tests are performed on each Ti64 geometry, but they are terminated at approximately the same displacement values where fracture occurs in the sequential tests. The thin specimen is loaded to a displacement of 1.8 mm, and the thick specimen is loaded to a displacement of 1.6 mm. These additional continuous tests both exhibit small cracks, as shown in Figure 4.4, confirming the continuous and sequential tests fracture at the same displacement. Thus, the sequential loading is not significantly altering the material response, and the DIC strain data from the sequential tests can reliably be compared to the simulation strain data. Because Ti64 exhibits asymmetric behavior in tension and compression and these tests induce a combination of tension and compression, two separate numerical models are included: one derived from uniaxial tension data and one from uniaxial compression. Both simulation responses are slightly stiffer than what is observed in the tests, but the tension curve produces a slightly closer match to the test data than the compression curve. Thus, the data from the tension curve simulations are used for further analysis and determination of the equivalent plastic strain to fracture.

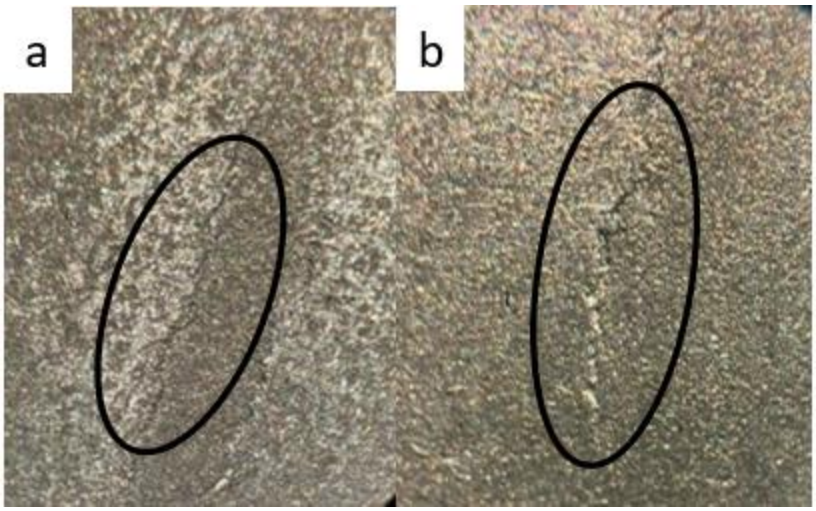

Figure 4.4: Cracks on surface of additional Ti64 continuous punch tests: a) thin specimen and b) thick specimen

The In718 simulation predicts significantly more stiffening than the tests. This is likely due to punch compliance in the actual tests. The 4340 steel punch may deform elastically, causing lower loads. This invalidates the assumption of punch rigidity, and future simulations may need to assume an elastic modulus for hardened 4340 steel to match the force-displacement responses. Although the strain data is unlikely to match at similar load values, the equivalent plastic strain at fracture can still be estimated if the strain histories agree as a function of punch displacement. A load drop is visible in two of the continuous tests and occurs at about 3 mm of punch displacement. One of the continuous tests is stopped at about 2.78 mm of displacement, and this test does not exhibit a drop in load. The tests that show a drop in load exhibit fracture on not only the specimen, but also on the backing plate. The test stopped before the load drop exhibits fracture on the specimen, but it does not exhibit fracture on the backing plate. Therefore, it can be concluded that the drop in load corresponds to a fracture on the backing plate, and

fracture on the test specimen occurs just before this drop in load at a displacement of about 2.78 mm. Figure 4.5 shows the crack on the specimen.

Figure 4.5: Fracture on In718 specimen where loading is stopped before load drop

Although the In718 continuous and sequential tests behave approximately the same for the duration of the tests, it is clear that the loads in the sequential tests are slightly lower than the continuous tests near the onset of fracture. In two sequential tests, a sharp load drop is visible. The softening and load drop behaviors can be seen in Figure 4.6. No backing plates fracture in the sequential tests, which indicates the drop in load is due to the specimen material fracturing. While the softening behavior exhibited near fracture in the sequential tests is not ideal, the material still behaves the same way in the continuous and sequential loading cases for the majority of the test duration. This lends credibility to the claim that the displacements measured through DIC in the sequential tests are representative of the displacements on the specimen surfaces in the continuous tests.

Figure 4.6: Softening and sharp load drop in In718 sequential test

There can also be some difficulties when attempting to spot the onset of fracture in the sequentially loaded tests. The specimen surface is examined for fracture after each loading increment, but the adhesive layer can cause the paint to stay intact and cover up a small crack. If fracture is not visible, the test is continued. Thus, the initial crack can be missed. In the In718 test titled Seq-N1, no load drop is visible in the force-displacement curve, but a small crack is still visible on the specimen surface. This indicates that the material likely fractures during the loading increment before the load drop in the other two tests. The DIC image before the drop in load is thus taken as the final frame when estimating the equivalent plastic strain to fracture.

The AE data for the Ti64 thin specimen tests all exhibit a high-energy event at a load of approximately 4500 N, as shown in the plot of normalized cumulative hit energy in Figure 4.7. Upon examination of Figure 4.1, it can be seen that the tests exhibit a slight drop in load around 4500 N. This indicates some fracture is almost certainly occurring at this time. However, it has

been shown that the initial fracture occurs at a lower load, so this high-energy AE hit combined with the load drop observed at about 4500 N is likely caused by a larger, more catastrophic crack propagation. The energy from the initial fracture is not large enough to distinguish from external noise.

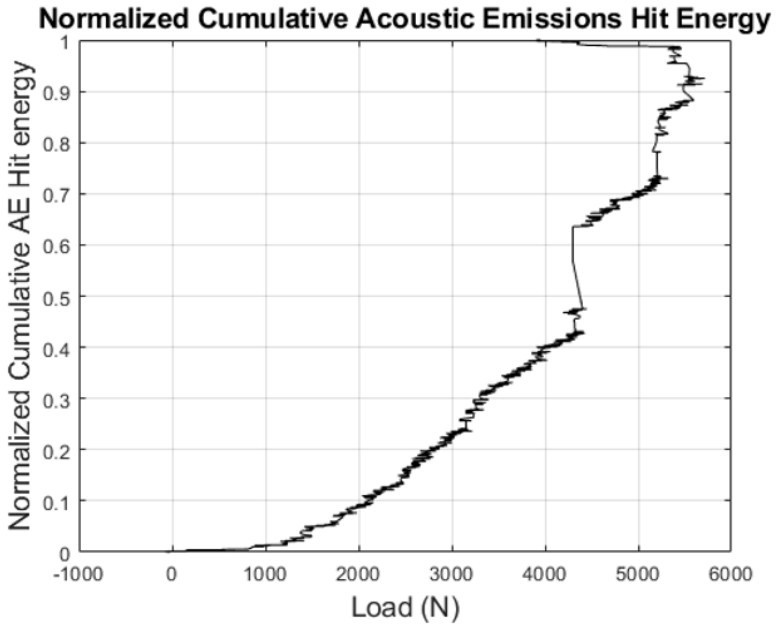

Figure 4.7: Normalized cumulative AE hit energy as a function of load for the Ti64 thin specimen test.

The remaining tests yield inconclusive results from the AE data. There are no consistent spikes in AE hit energy, as shown in Figures 4.8 and 4.9. The registered AE hits appear to be due to extraneous noise. It is unclear why the Ti64 thin specimen tests show clear evidence of fracture, but the thick Ti64 specimen tests do not. It is possible that the sensors were placed in slightly different locations on the test fixture for the thick specimen tests. If the sensors were

placed farther away from the specimen, the vibrations emitted from fracture would have to travel through more material, introducing a higher probability the energy from fracture could be damped out. Because the specimen is thicker, the vibratory waves inherently have to propagate through more material. This issue could be avoided in future experiments by fabricating larger specimens and backing plates, which would allow at least one sensor to be attached directly to the backing plate surface. For the purposes of these experiments, specimens were designed to use the least amount of material as possible, but larger backing plates could have been designed to allow for better AE sensor placement.

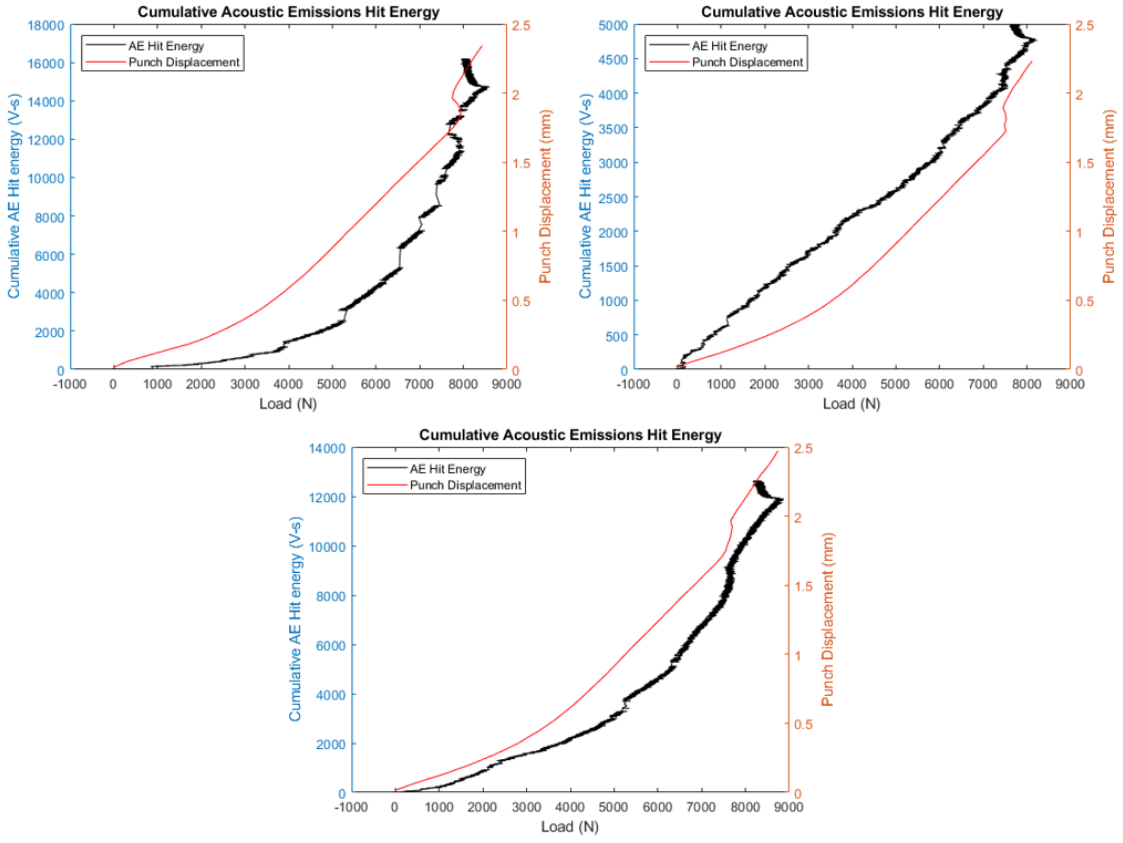

Figure 4.8: Cumulative AE hit energy for Ti64 thick specimen tests

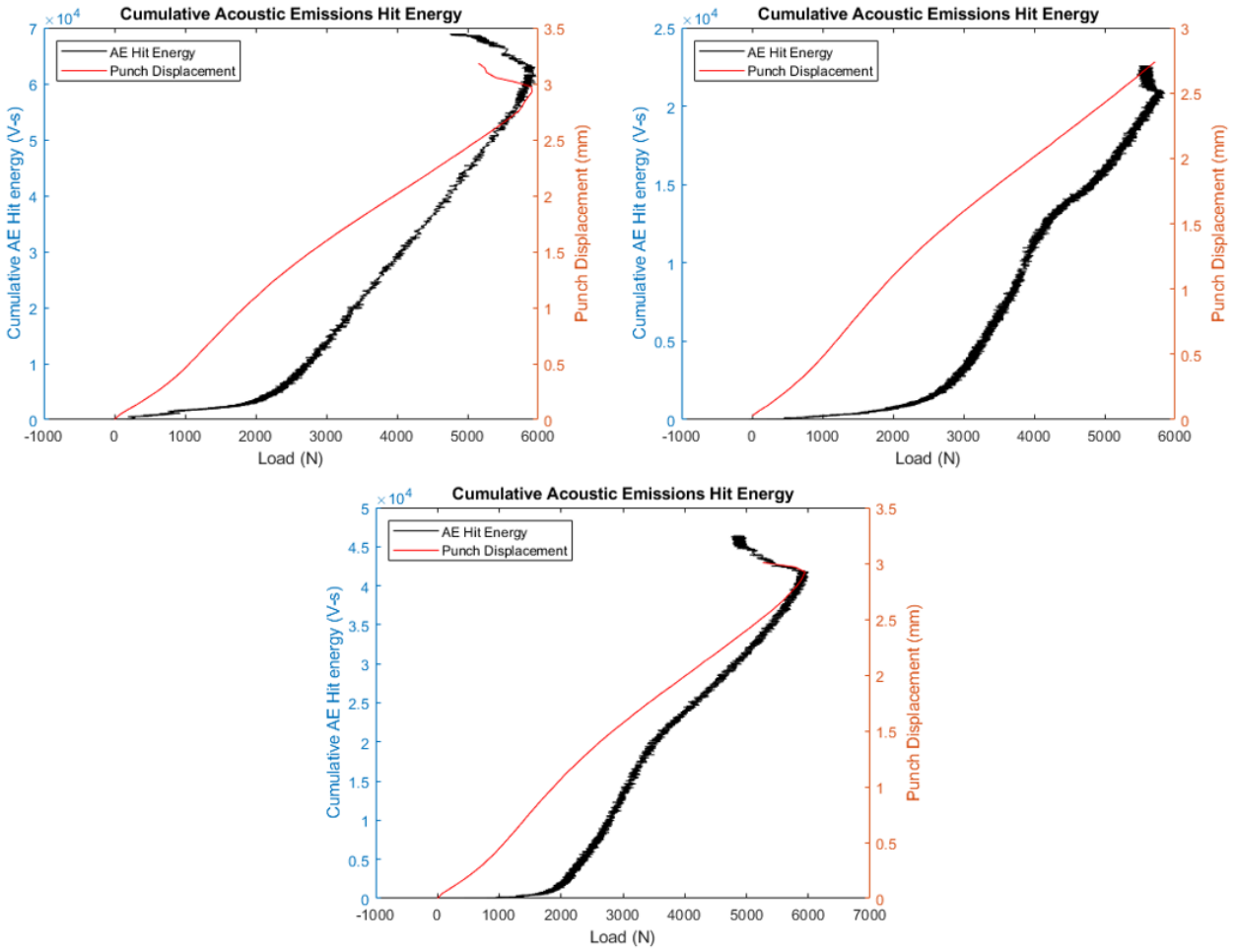

Figure 4.9: Cumulative AE hit energy for In718 tests

The location at which fracture initiates is significant for these tests because the location influences which element the stress load path should be extracted from in simulation. It is difficult to tell exactly where fracture initiates in the tests, but upon examination of the post-test images (Figures 4.10-4.12), it appears the cracks initiate along the major diameter of the punch. In the simulations, this would correspond to multiple elements. However, because the center element is placed under the most in-plane tension, it is reasonable to assume this is where the

fracture would initiate. This is because fracture strains generally decrease as triaxiality decreases. Thus, it is assumed that fracture initiates in the center and then quickly propagates along the punch major diameter as the punch is advanced, justifying the extraction of stress state history from the center element in simulation. This also maintains consistency with the design simulations, as stress states were fine-tuned based on the center elements.

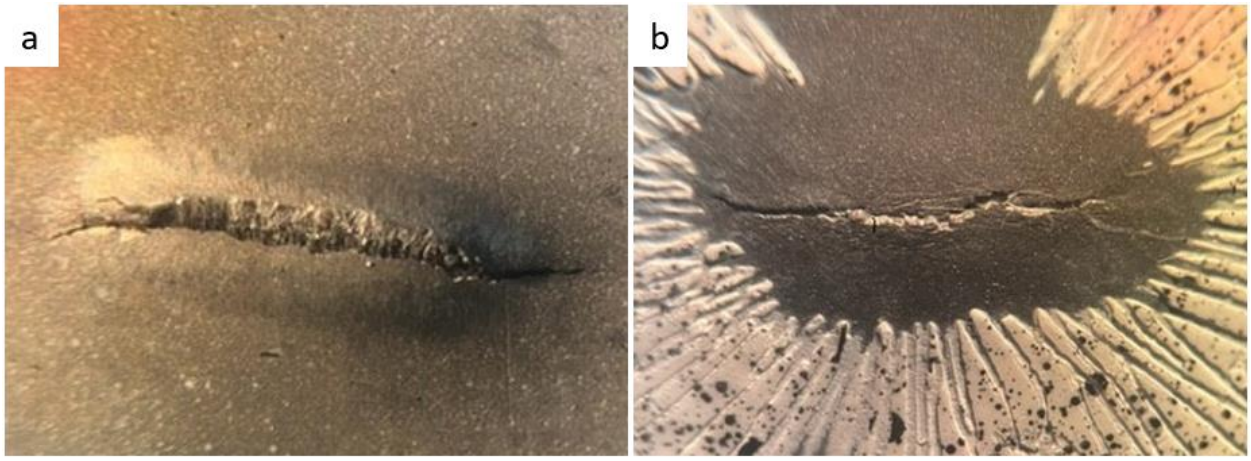

Figure 4.10: Post-test images of Ti64 thin specimens: a) continuous and b) sequential test

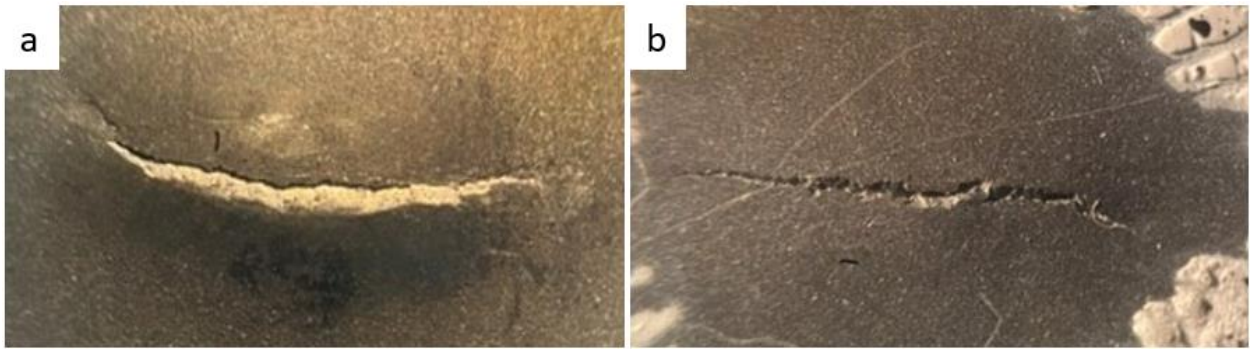

Figure 4.11: Post-test images of Ti64 thick specimens: a) continuous and b) sequential test

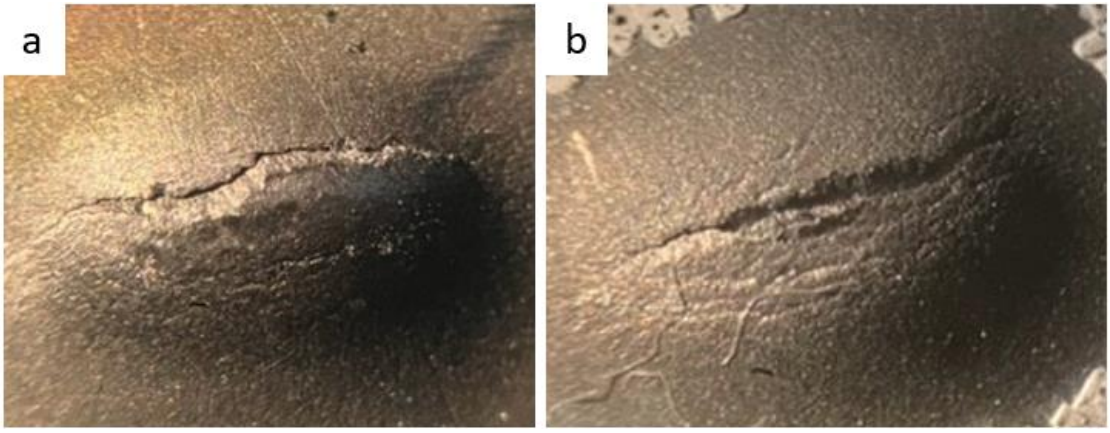

Figure 4.12: Post-test images of In718 specimens: a) continuous and b) sequential test

To validate the plasticity models are accurately capturing the physical material behaviors, strain data along line slices of elements in the simulations can be compared to line slices of DIC strain data in the tests, as shown in Figure 4.13. The maximum principal strains are extracted along both the major and minor diameters of the punches for each test. The simulated and measured values are plotted at similar punch displacement values along the punch major and minor diameters in Figures 4.14 and 4.15, respectively.

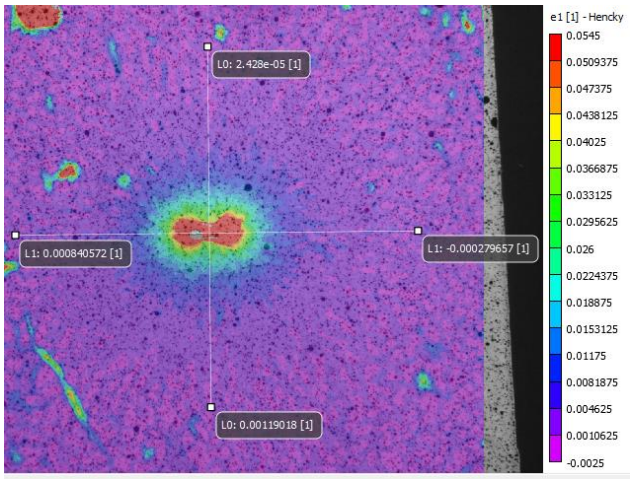

Figure 4.13: Sample line slice locations from a test specimen

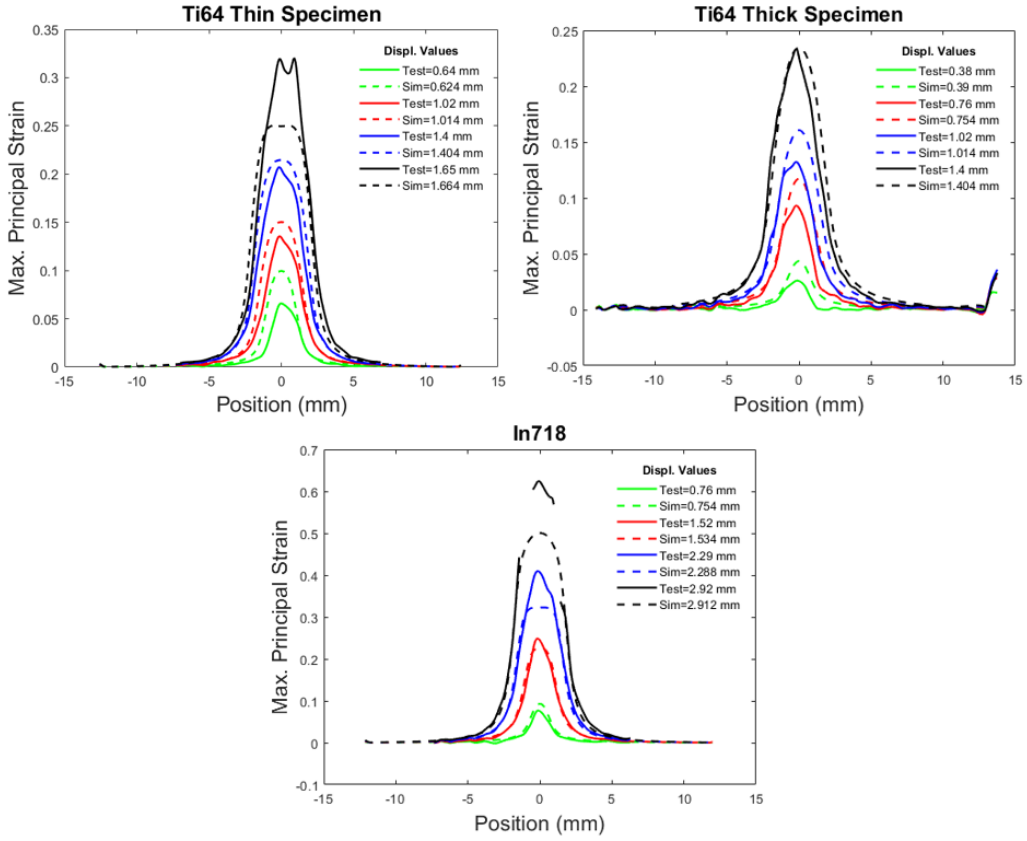

Figure 4.14: Maximum principal strain along major diameter

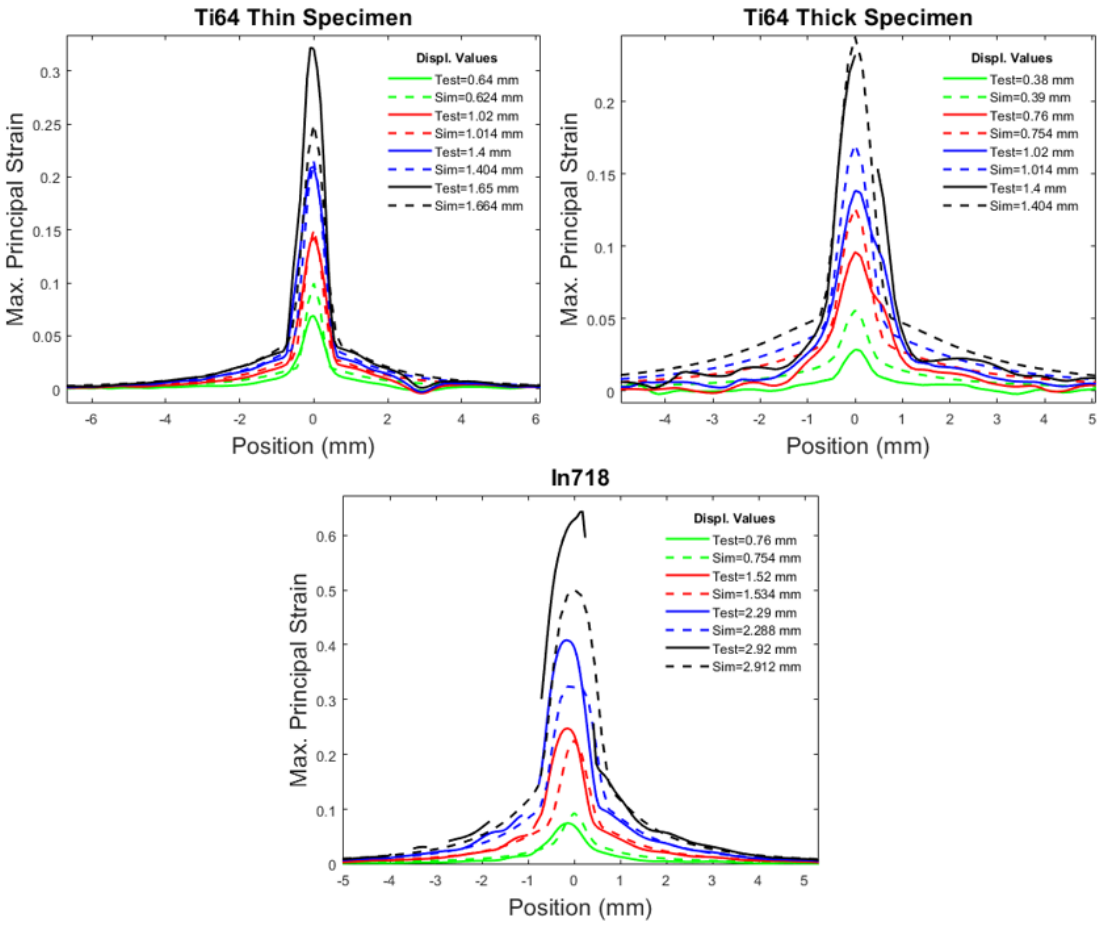

Figure 4.15: Maximum principal strain along minor diameter

It is evident that there is some DIC data dropout at high displacements. The contact between the specimen and backing plate can cause some of the paint to be scraped off, as shown in Figure 4.16. The large out of plane displacements also create radial cracking in the cyanoacrylate adhesive layer that protects the speckle pattern from smearing and flaking off. Furthermore, strain increments are large because these tests are loaded sequentially. These factors all introduce potential for DIC error and dropouts.

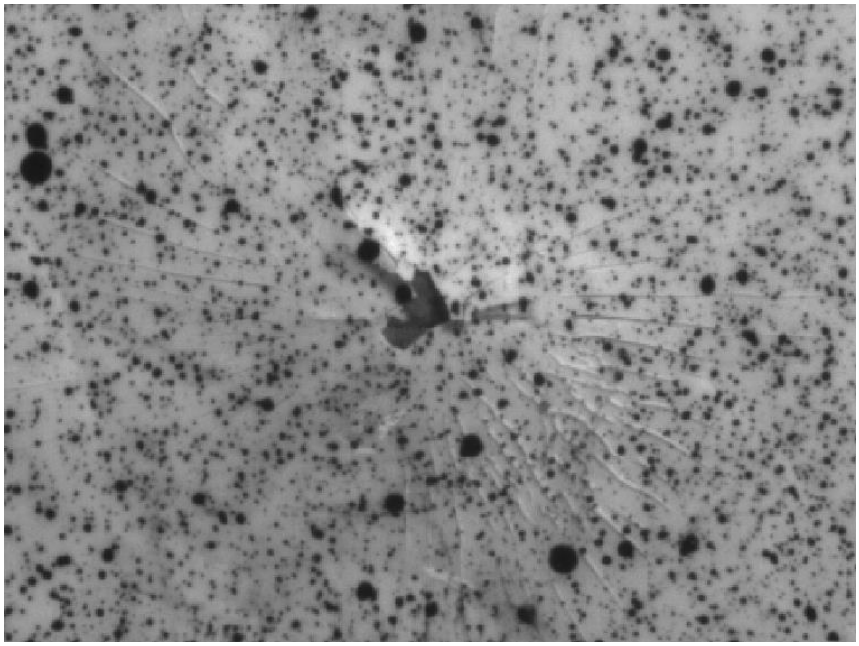

Figure 4.16: Example of paint flaking off and radial cracking in the adhesive layer

The Ti64 thin specimen tests show reasonable agreement with the simulation. The simulation over predicts the strains at low displacements and under predicts them at high displacements. For the Ti64 thick specimen, the strains align at high displacements, but once again the simulation under predicts the strains at lower displacements. In the case of In718, the strains align well early on, but the experimental strains are larger than the simulated values at high displacements. It is reasonable to assume the strains may be a bit higher in the tests near the onset of fracture due to strain localization that the plasticity models are not capturing. Elastic springback behavior will cause the strains to be slightly lower in an unloaded state compared to a loaded state, but the elastic strains should be small compared to the plastic strains. The imperfect matches at lower displacements are likely driven by small errors in both the DIC measurements and plasticity models. The stress-strain relations are derived from uniaxial test data, so they

cannot be expected to perfectly predict the material response in such a complex loading case. Simplified boundary conditions and slight geometric differences also introduce some error. Lastly, any anisotropy due to the plate rolling directions are not considered in either test or simulation. Considering the potential for errors, it is concluded that the tests and simulations are generally in agreement.

The principal strains at the point of fracture are plotted in Figures 4.17 and 4.18. For most tests, most or all of the DIC data survive the duration of the test, allowing a direct comparison of strains at the fracture location between test and simulation.

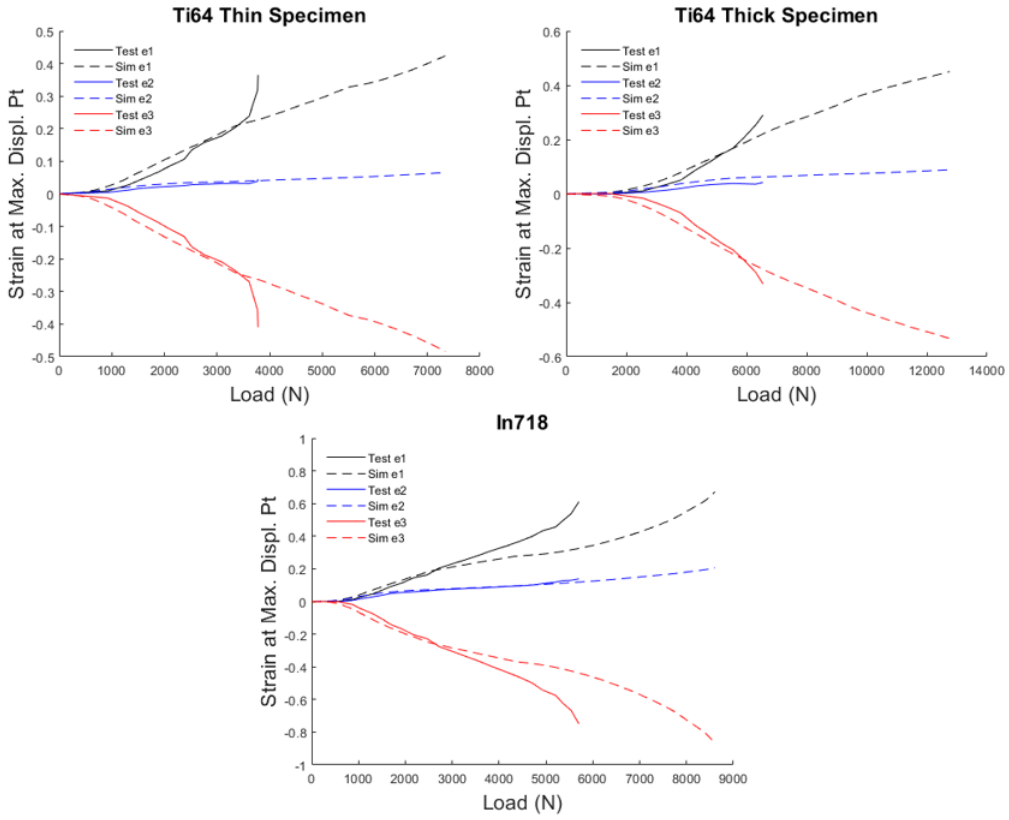

Figure 4.17: Principal strains at fracture location for backed punch tests as functions of applied load

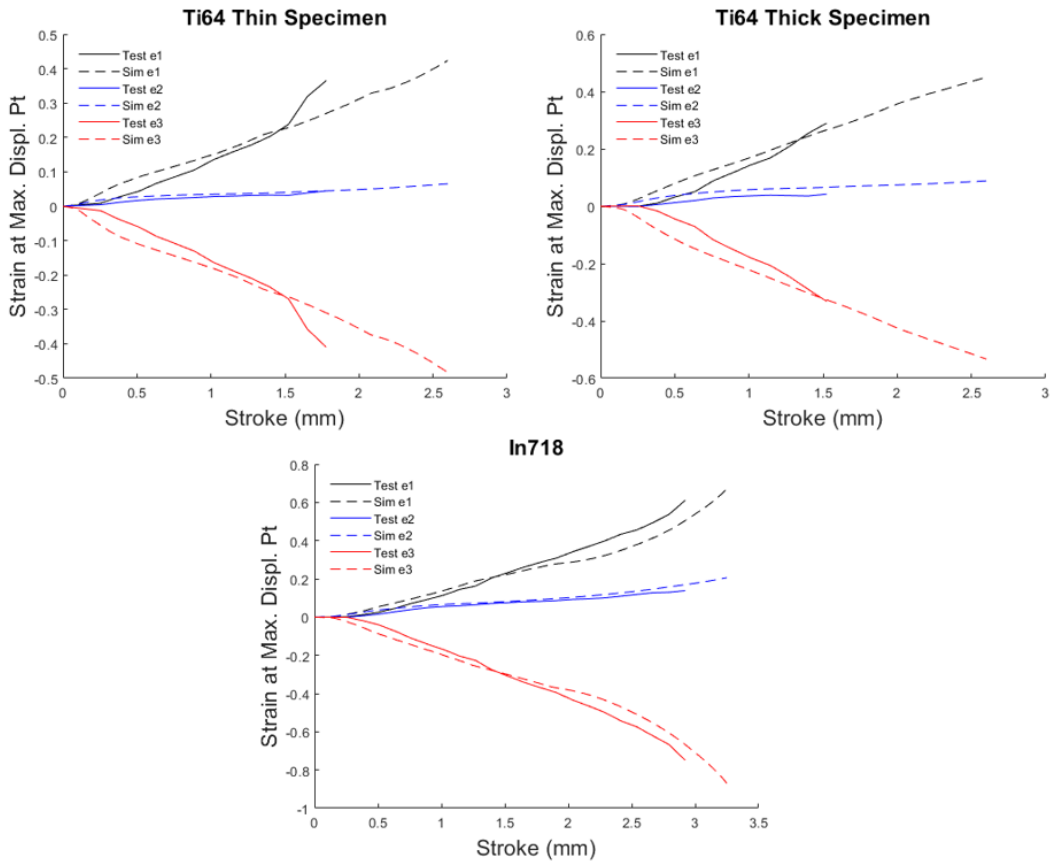

Figure 4.18: Principal strains at fracture location for backed punch tests as functions of punch displacement

The simulated and experimental principal strains all show reasonable agreement. Once again, it is important to note the experiments are performed with interrupted loading. This explains why the experimental strains start out a bit flatter than the simulated values. While the deformation is still elastic, the test data will show zero strain because the DIC images are taken in an unloaded state. There is also some inherent error in the DIC strain computation based on the chosen DIC parameters. Because strains are computed over a very small area, values can vary significantly among neighboring points. The strain filter helps alleviate this issue, but the

data can still be noisy depending on the size of the strain filter. The smallest possible strain filter of 5 was used in data processing for these tests to maintain a small VSGL, so noise is expected in the local strain computations. Therefore, perfect agreement cannot be expected, but both test and simulation should follow the same general trends. While the strain increases linearly, the lines should be approximately parallel. In Figure 4.17, once the load begins to flatten and the strains continue to increase exponentially, the test data deviate from the simulations. This is most likely due to strain localization as the material nears fracture, but paint flaking near the area of fracture as shown in Figure 4.16 can also artificially alter the DIC strains. In Figure 4.18, the strains are plotted as a function of punch displacement. There is good agreement between test and simulation for each test. There is some evidence of strain localization in the thin Ti64 test, but overall the simulation appears to capture the strain history well.

Next, the plastic strains are analyzed. The equivalent plastic strains are computed from the principal strain increments using the process described in the introduction to this chapter. These are plotted along with the stress state histories from the simulations in Figure 4.19. The data are truncated at the displacements where fracture occurs in the tests. The equivalent plastic strain at this point in the simulation is taken as the estimated equivalent plastic strain to fracture for the stress state of interest.

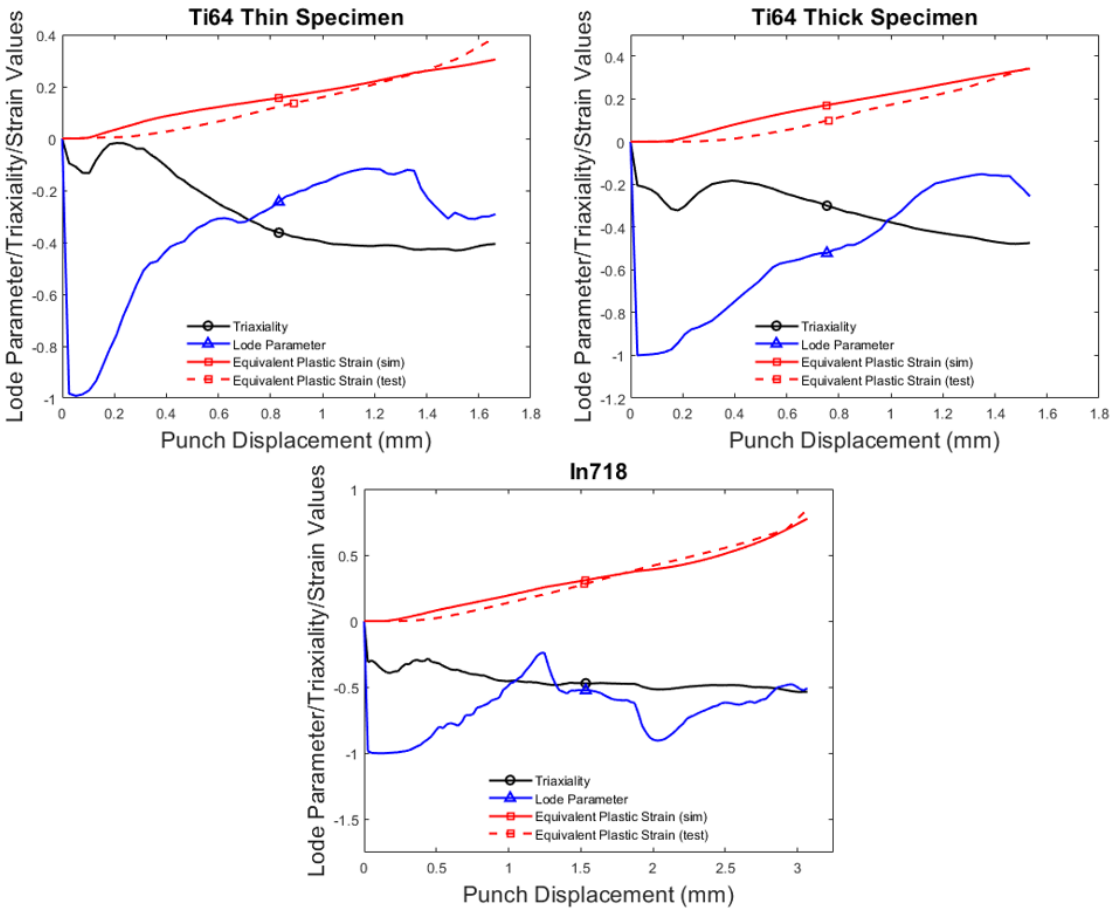

Figure 4.19: Stress state and plastic strain history for backed punch tests

It is evident that the plastic strains in the tests take a bit longer to start accumulating than they do in the simulations, especially for the Ti64 tests. It is possible the yield strengths in the simulations are slightly lower than the physical yield strengths in the tests. This is especially plausible for Ti64 since it is known to exhibit significantly asymmetric behavior in tension versus compression. In this combined loading state, the actual yield strength is unknown, so it is reasonable for the onset of plasticity to differ in the tests and simulations. Regardless, the Ti64 plastic strains show similar behavior in the tests and simulations for both the thin and thick

specimens, so extracting the fracture strain from simulation is still valid. The In718 test data show excellent agreement with the simulation. Although the force-displacement responses differ, the fracture strain can still reliably be estimated because the simulation accurately predicts the equivalent plastic strains in the tests. The simulations are truncated once the punch displacement at fracture matches the displacement at fracture in the simulation. The average stress state parameters are calculated, and the equivalent plastic strain from the simulation is taken as the estimated fracture strain. Results from each test are summarized in Tables 4.1-4.3. It is important to note that some or all of the fracture strains for a given test may be identical. This is because the strain at fracture is only extracted from the sequentially loaded tests. Therefore, if each test fractures at the same loading increment, as in the Ti64 thick specimen case, then the fracture strain will be identical for each since the simulation is truncated at the same displacement.

Table 4.1: Ti64 thin specimen fracture results

Test	Avg Lode Parameter	Avg Triaxiality	Fracture Strain from Test	Fracture Strain in *MAT_224 Fracture Surface	Disp at Fracture (mm)	Load at Fracture (N)
Seq-N2	-0.3452	-0.2768	0.3321	0.454	1.778	3781
Seq-N3	-0.3551	-0.2657	0.3045	0.455	1.651	3621
Seq-N4	-0.3452	-0.2768	0.3321	0.454	1.778	3968

Table 4.2: Ti64 thick specimen fracture results

Test	Avg Lode Parameter	Avg Triaxiality	Fracture Strain from Test	Fracture Strain in *MAT_224 Fracture Surface	Disp at Fracture (mm)	Load at Fracture (N)
Seq-N1	-0.4932	-0.3159	0.3413	0.457	1.524	6383
Seq-N2	-0.4932	-0.3159	0.3413	0.457	1.524	6548
Seq-N3	-0.4932	-0.3159	0.3413	0.457	1.524	6574

Table 4.3: In718 fracture results

Test	Avg Lode Parameter	Avg Triaxiality	Fracture Strain from Test	Fracture Strain in *MAT_224 Fracture Surface	Disp at Fracture (mm)	Load at Fracture (N)
Seq-N1	-0.6259	-0.4437	0.7003	0.6423	2.921	5702
Seq-N2	-0.6259	-0.4437	0.7003	0.6423	2.921	5782
Seq-N3	-0.6451	-0.4336	0.5759	0.6812	2.667	5262

For the Ti64 thin and thick specimen tests, the fracture strains obtained from the tests are lower than the values on the Ti64 *MAT_224 fracture surface. The average fracture strain for the thin specimen tests is 0.3229. *MAT_224 predicts an average fracture strain of 0.454 for the average stress states induced by the tests. This is a 40.6% error assuming the experimentally determined value is the true value. Each Ti64 thick specimen test yields the same fracture strain of 0.3413. The model's fracture surface has a fracture strain of 0.457 at the stress state of interest, indicating a 33.9% error in the model. There is clear potential for fracture surface calibration based on this test data. Hemispherical backed punch tests on Ti64 performed by Spulak [8] showed a fracture strain of 0.47 for an average Lode parameter and triaxiality of -0.98 and -0.25, respectively. The new thin test has a similar triaxiality, but a significantly lower fracture strain. Therefore, it is evident the Lode parameter has a significant impact on the fracture strain at triaxialities between -0.25 and -0.32. This is consistent with the theory behind modern fracture models, as fracture strains tend to decrease as the stress state deviates from axisymmetric loading. The influence of deviatoric stresses become more prevalent as the Lode parameter approaches 0, and increasing distortion and encouraging fracture.

The In718 *MAT_224 fracture surface appears to be a more accurate reflection of the ductile fracture behavior for the states of stress induced by the In718 elliptical backed punch

tests. The average fracture strain from the test data is 0.6588, and the average fracture strain from the model is 0.6553. This is a negligible percent difference of 0.53%. Previous backed punch tests on In718 yielded inconclusive results [8]. The specimens became excessively thin when loaded in a sequential manner, causing premature fracture in relation to continuously loaded tests. For the new tests, a thinner backing plate is used, which induces less compression. This allows fracture to occur in a more tension-dominated stress state before excessive thinning due to In718's high ductility causes premature failure. Also, the elliptical geometry pulls the Lode parameter away from -1, which evidently lowers the equivalent plastic strain at fracture significantly. The referenced work yielded lower limits on the fracture strain for In718. For an average triaxiality of -0.23 and average Lode parameter of -0.95, the lower limit to the fracture strain was determined to be 2.21. For an average triaxiality of -0.08 and average Lode parameter of -0.96, the lower limit to the fracture strain was determined to be 2.28. For the elliptical backed punch tests on In718, the average triaxiality is -0.4403, and the average Lode parameter is -0.6323. As mentioned above, the average fracture strain for this stress state is determined to be 0.6588. The fracture strain for In718 is clearly highly sensitive to the state of stress in this area of the fracture surface. It is likely that the decrease in triaxiality and deviation from a Lode of -1 relative to the previous work have a compounding effect in lowering the fracture strain.

As expected, the thin Ti64 specimen test induces a higher triaxiality than the thick specimen test. In the thin specimen test, the backing plate is twice as thick as the specimen; whereas in the thick specimen test, the backing plate is 1.24 times thicker than the specimen. The higher backing plate thickness ratio induces more out-of-plane compression, and thus a higher triaxiality. The In718 test experiences the lowest triaxiality with a backing plate to specimen

thickness ratio of 1.4. Although this ratio is greater than that of the Ti64 thick specimen test, the In718 test still induces a lower triaxiality. This is because the thick 1.27 mm Ti64 specimen induces more compression through the actual thickness of the specimen than the thinner 0.635 mm In718 specimen.

It is worth noting again that taking the average stress state values is not the most accurate way of comparing the tests to the fracture model. In reality, the damage of each element in simulation is accumulating based on the state of stress in each time step. This is why one of the goals in the test design phase was to maintain as constant of a triaxiality and Lode parameter as possible. This is also why the average triaxialities and Lode parameters are computed with respect to equivalent plastic strain. This ensures the stress states under which the most damage would be accumulated have the highest weight when computing the average. These considerations make taking the average stress states a valid approach to evaluating the current fracture model while avoiding the cumbersome approach of monitoring the damage evolution through each loading increment.

4.2 Notched Compression Ring

Examination of the force-displacement curves in the notched ring tests is the first step in validating the plasticity models used for the simulations. As shown in Figures 4.20 and 4.21, the Al-2024 and Ti64 test results showed excellent agreement with the simulations. However, in Figure 4.22, the In718 simulation predicts a significantly stiffer response than what is exhibited in the tests. Although the Ti64 and Al-2024 force-displacement responses show reasonable agreement between test and simulation data, it is evident that the slope of the tangent modulus is a bit higher in the simulations as the curves flatten in the tests. At this point, the strains are likely

localizing as the material approaches fracture, causing strains to be slightly higher near the fracture location than what is predicted in simulation.

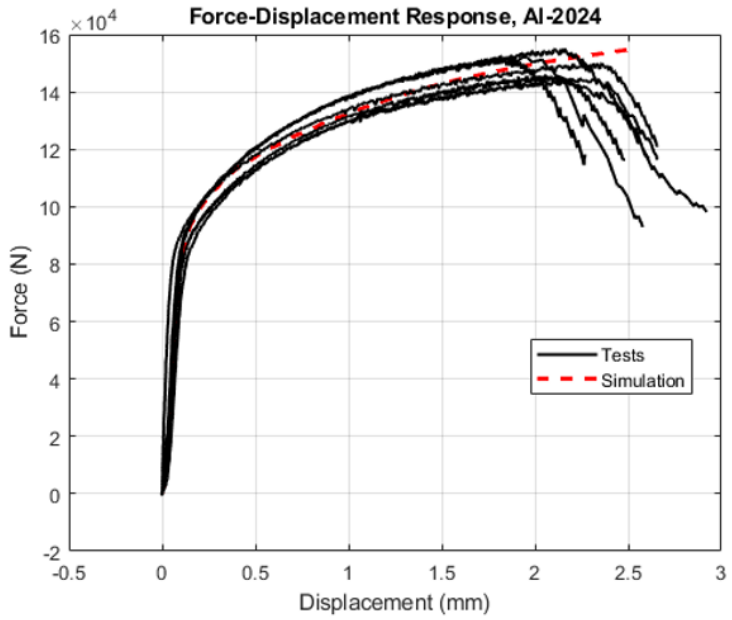

Figure 4.20: Force-displacement responses for Al-2024 notched rings

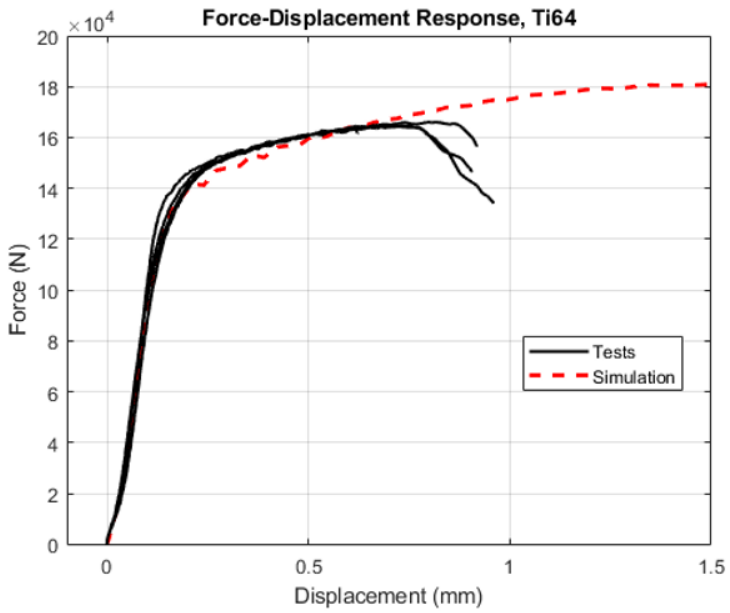

Figure 4.21: Force-displacement responses for Ti64 notched rings

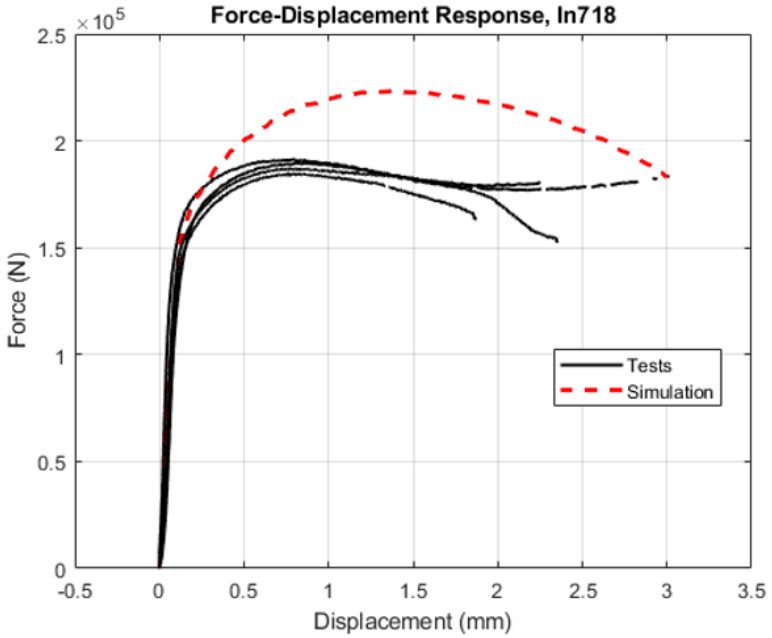

Figure 4.22: Force-displacement responses for In718 notched rings

It is difficult to see exactly when fracture occurs in the DIC images due to the nature of this compression test. Compression generally inhibits void growth and coalescence, and even when a crack does initiate, it can be too thin to clearly see in the images. The specimen does not clearly section itself as it would in a standard tension test. Also, the spray paint on the specimen can become smeared, wrinkled, or flake off, making it optically challenging to identify a crack. An example of wrinkling is shown in Figure 4.23.

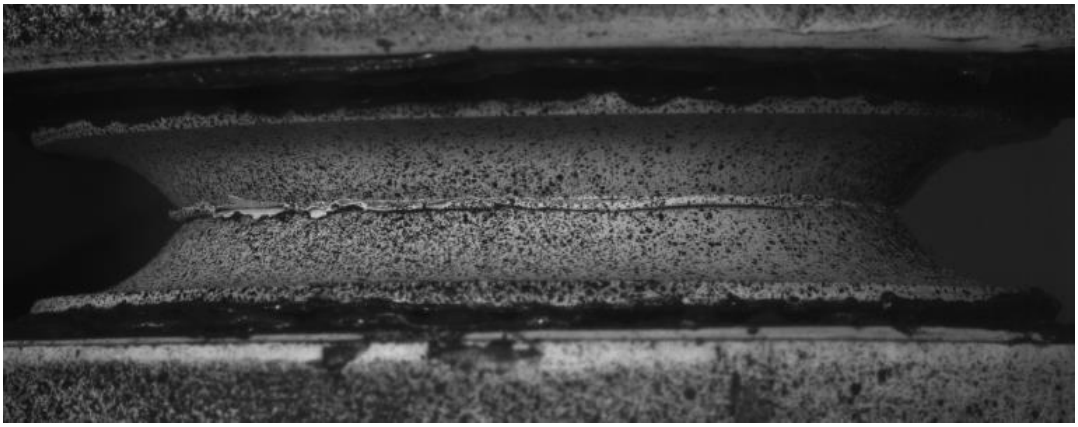

Figure 4.23: Example of paint wrinkling on an In718 specimen

Additionally, the acoustic emissions data obtained from these tests fail to capture the initial fracture. The energy emitted from the initial crack is too small to distinguish from external noise. The AE data can only reliably be used to identify a larger, more catastrophic fracture event. For example, in one of the Ti64 tests, the test is continued after the initial load drop for a few seconds, leading to severe buckling and crack propagation. This generates a relatively high-energy AE hit, as shown in Figure 4.24. A very small jump in AE hit energy can be seen in Figure 4.24 that appears to correspond to the drop in load. This jump could be due to the initial

fracture, but unfortunately this phenomenon is only observed in this particular test. The remaining tests do not show the same jump in energy near the load drop, so it cannot be concluded that this jump in energy corresponds to fracture. One limitation of this test setup is the inability to place the sensors in direct contact with the specimens due to their curved geometry. If reliable AE data is to be obtained in the future, it may be worth considering a specimen design that allows the AE sensors to be placed in direct contact with the specimen, allowing for vibrations emitted from fracture to be more easily detected.

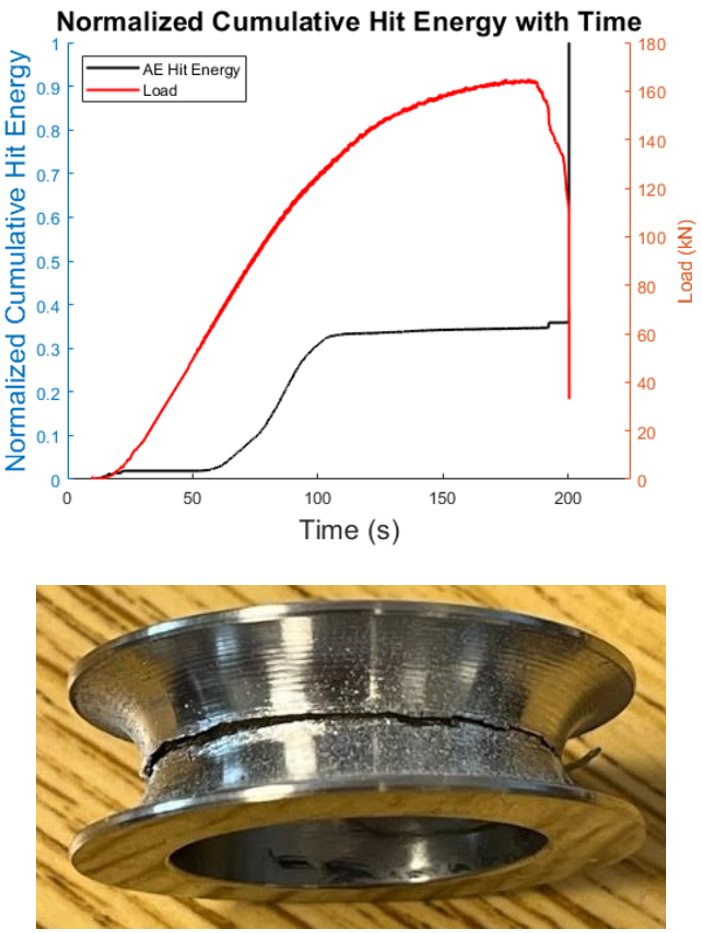

Figure 4.24: Normalized cumulative hit energy from a Ti64 test (top). The massive energy spike and load drop at the end is due to severe buckling and crack propagation (bottom). The crack propagates through the entire thickness of the specimen.

Despite the difficulties in seeing the fracture with DIC images and unreliable AE data, fracture can be correlated with the sharp drops in load seen in the force-displacement curves of Al-2024 and Ti64. Scanning electron microscopy (SEM) is used to confirm the presence of fracture in Figures 4.25 and 4.26. For Al-2024 and Ti64, planes slipping past one another in the center of the specimen are clearly visible, indicating material separation. It is reasonable to

conclude this material separation causes the specimen to lose its structural integrity, leading to a sharp drop in the applied load. Thus, a DIC image corresponding to the time at which the load first drops is taken as the final image before failure, and the simulation stress state history is truncated at this point when comparing test and simulation data for Al-2024 and Ti64.

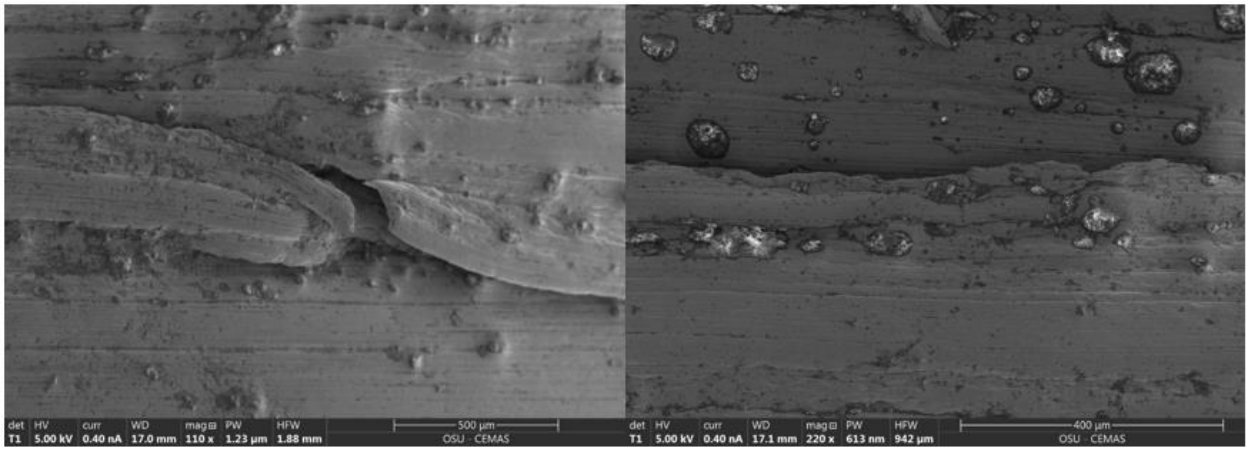

Figure 4.25: Post-test SEM images of a Ti64 specimen

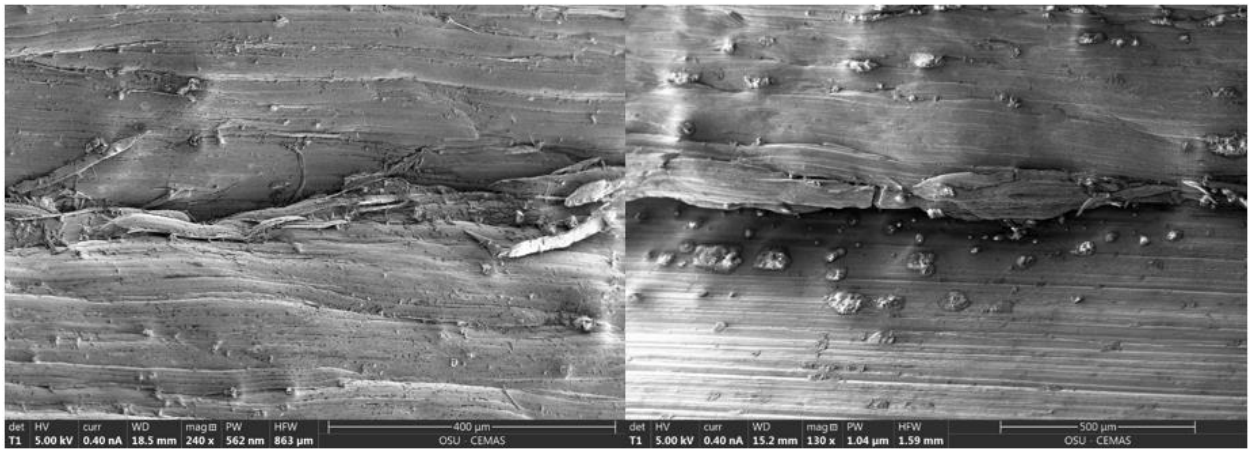

Figure 4.26: Post-test SEM images of an Al-2024 specimen

Fracture is not as obvious in the case of In718. The force-displacement curves do not exhibit consistent behavior. Only one of the curves shows a sharp drop in load, and two of them show a load increase after an initial decrease. Macroscopic images appear to show a circumferential crack around the center of the outside surface of the specimen, but when looking at this region more closely using SEM in Figure 4.27, the material appears to only buckle inward. This is the same buckling behavior predicted in simulation. To further investigate, the specimens are sectioned in half, allowing a view of the cross sections. Out of four samples, two exhibit fracture in shear, and two exhibit buckling behavior with no fracture. Figure 4.28 shows the fractured samples, and Figure 4.29 shows the other samples.

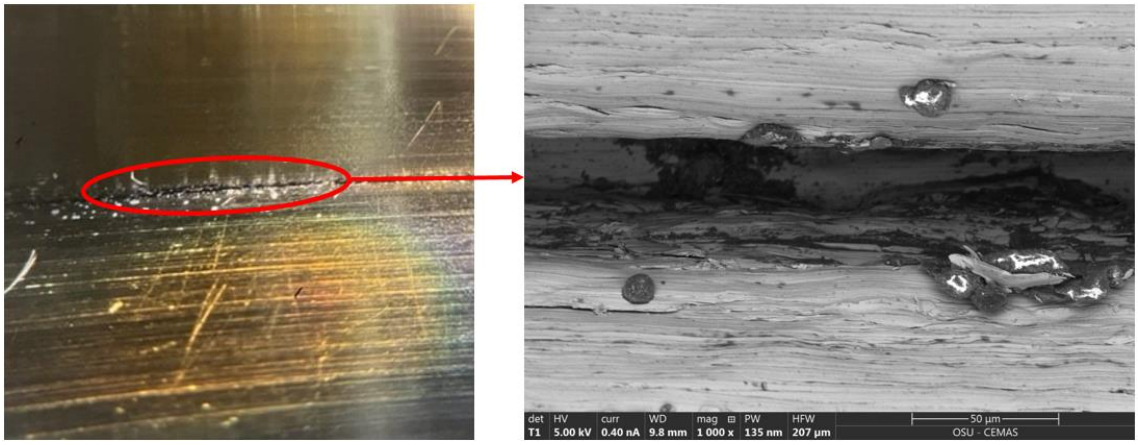

Figure 4.27: Buckling behavior in In718 test viewed under a stereo microscope (left) and a scanning electron microscope (right)

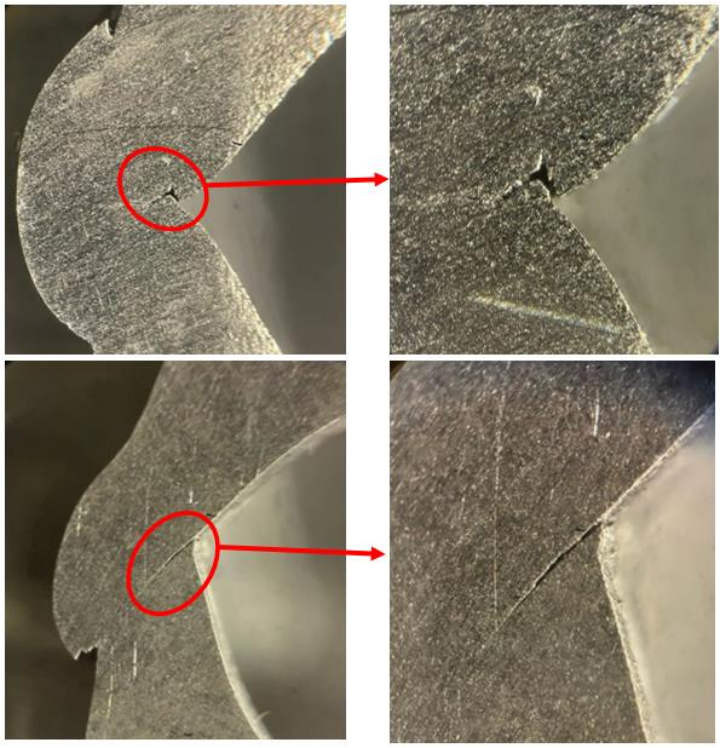

Figure 4.28: Cross section of fractured In718 samples

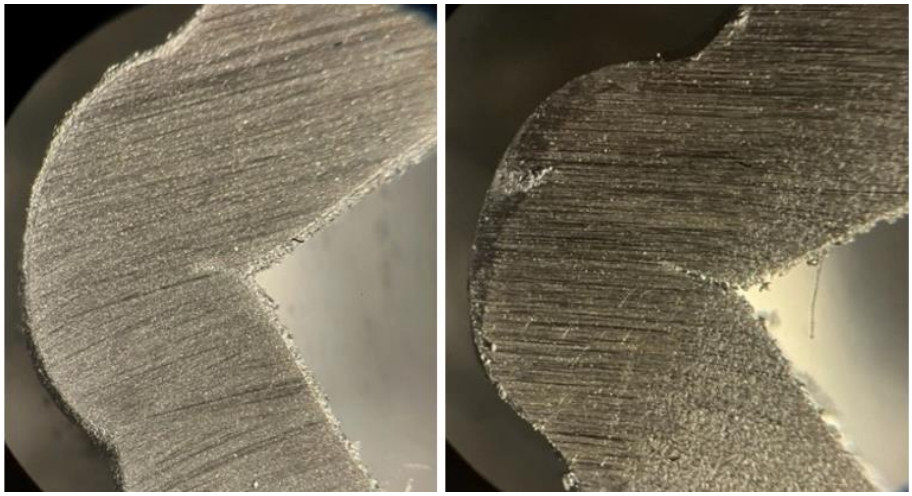

Figure 4.29: Cross section of In718 samples that did not fracture

The presence of fracture in In718 correlates with the boundary condition used in the test. The two fractured specimens are compressed between tungsten carbide platens bolted directly to the load frame, whereas the specimens that did not fracture are compressed between steel platens gripped in hydraulic wedge grips that are bolted to the load frame. One final test is performed with tungsten carbide platens placed between two large plates gripped in hydraulic wedge grips. This final test appears to not exhibit fracture, as the force-displacement response behaves in a similar way to the tests compressed between steel platens. Figure 4.30 displays the influence of the boundary condition on the force-displacement responses. In the tests with hydraulic wedge grips, the load steadily drops after reaching a maximum, levels out, and begins to steadily increase again. The tests without grips show a consistent decrease in load after it reaches a maximum. The steel platens introduce significantly more compliance than the tungsten carbide platens, and it is reasonable to think they may not be strong enough to load the In718 rings all the way to fracture. However, it is unclear why the hydraulic wedge grips appear to influence the results, as the loads do not exceed the specified 250 kN limit of the grips. It is possible that more pressure could be used to firmly grip the plates, but based on these results it is concluded that utilizing tungsten carbide platens without hydraulic wedge grips is the best approach the induce fracture. Despite the inconsistent fracture behavior, it is encouraging that the force-displacement responses are in reasonable agreement at lower displacements and the maximum load remains consistent at around 185 kN. Further investigation is necessary to determine why the simulated force-displacement response does not agree with the test data.

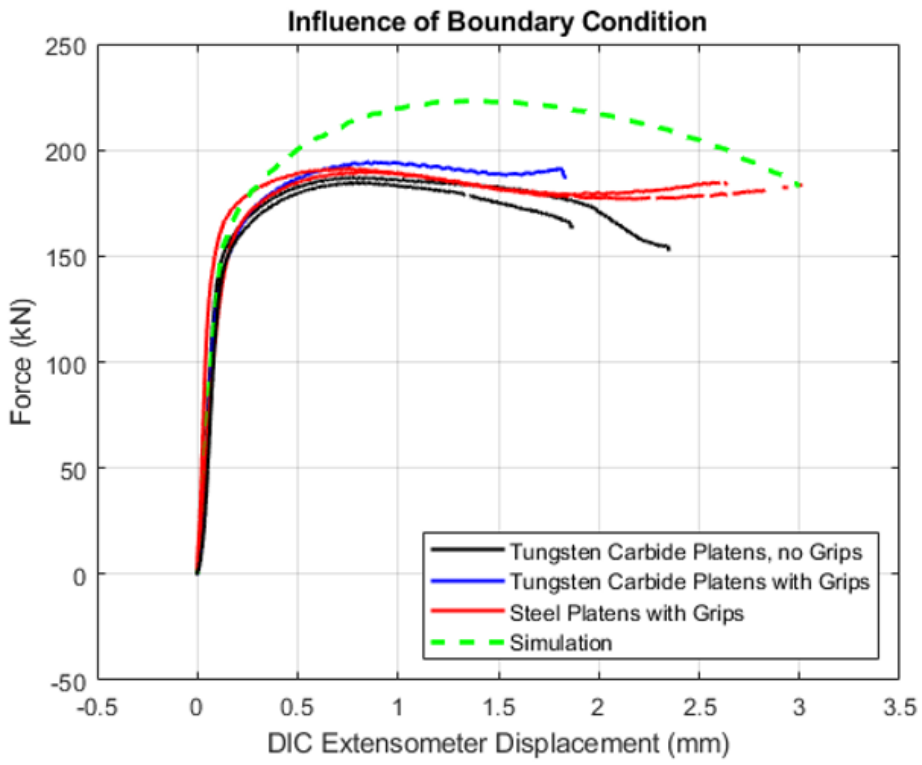

Figure 4.30: Influence of boundary condition on force-displacement response in In718 notched rings

Next, the strains measured through DIC are compared to the simulation data for each material. Line slices of DIC data points along the highest strained areas of the specimen are compared to line slices of element history strain data extracted from simulations in similar locations. The minimum principal strains are compared along these line slices at different displacements in Figure 4.32. Figure 4.31 illustrates a sample line slice location.

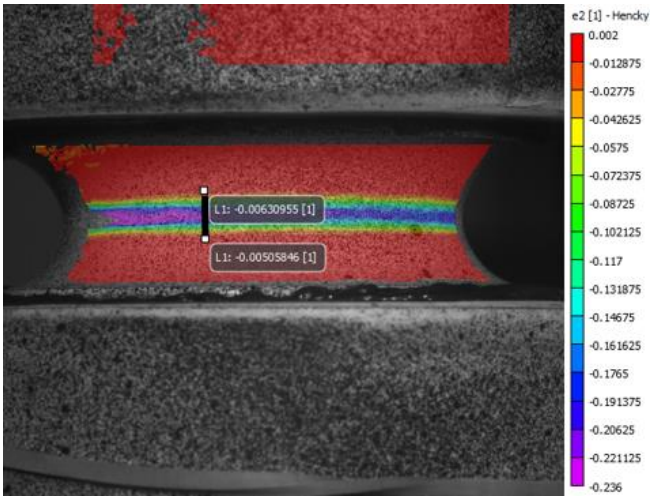

Figure 4.31: Sample location for line slice extraction

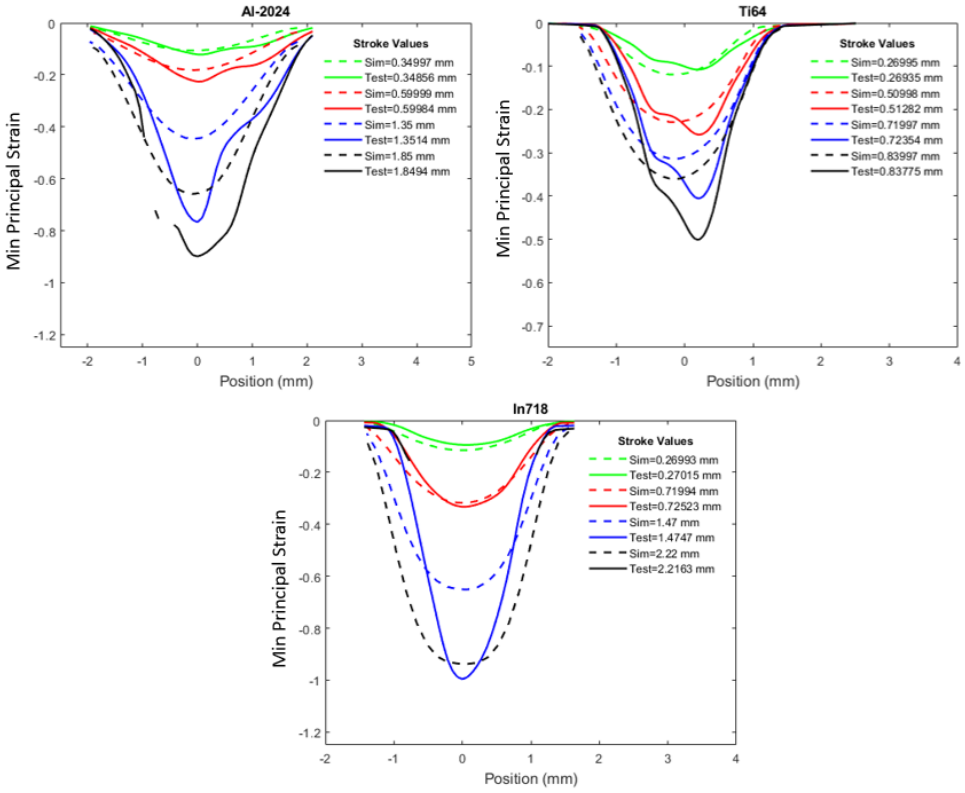

Figure 4.32: Minimum principal strains along line slices at various displacement values

Generally, test and simulation strains agree at low displacement values for all three materials. However, as displacements become larger, the DIC strains tend to either be higher than the simulated values or drop out completely. Figure 4.33 shows an example of a test with missing DIC data. Dropouts are expected at large displacements for these tests. Due to the nature of a compression test, the paint speckles can get compressed together and make it difficult for the software to track deformations. Because Ti64 fails at lower displacements, DIC data dropout is not as significant of an issue for these tests as it is for Al-2024 and In718. From this information, it can be concluded that the simulation captures the physical behavior of each material at low displacements. At higher displacements, strain localization, void growth and coalescence, and DIC error are all potential reasons for the poor match.

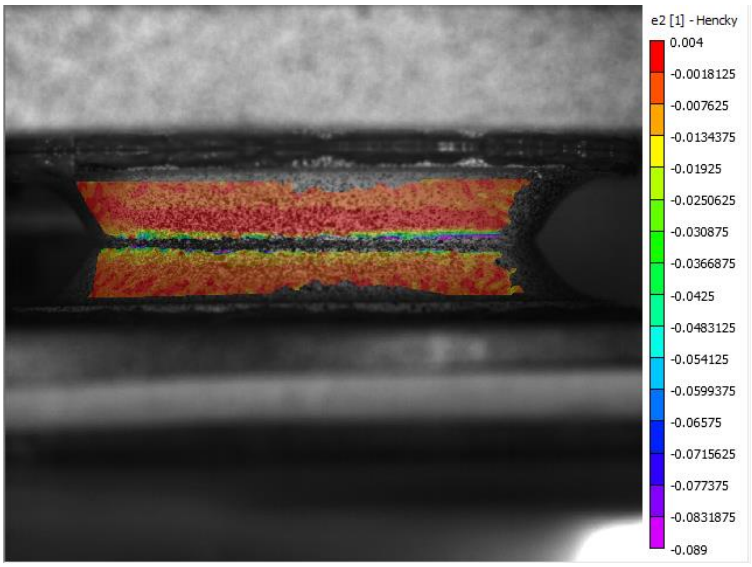

Figure 4.33: Sample DIC data dropout from an In718 test

To estimate the fracture strains under the stress state of interest, strain data at the point of fracture can be analyzed. The evolution of the principal strains at the fracture location can be compared between test and simulation. The principal strain evolution is plotted as a function of load and displacement in Figures 4.34 and 4.35, respectively.

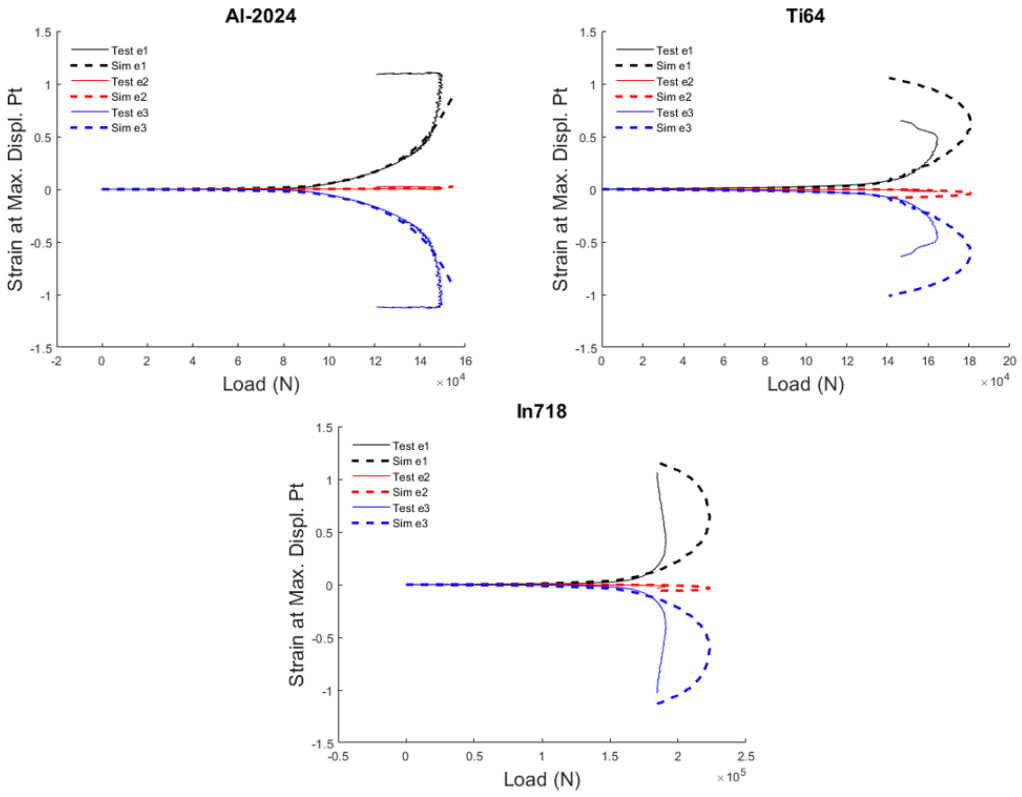

Figure 4.34: Principal strains at fracture points as a function of applied load

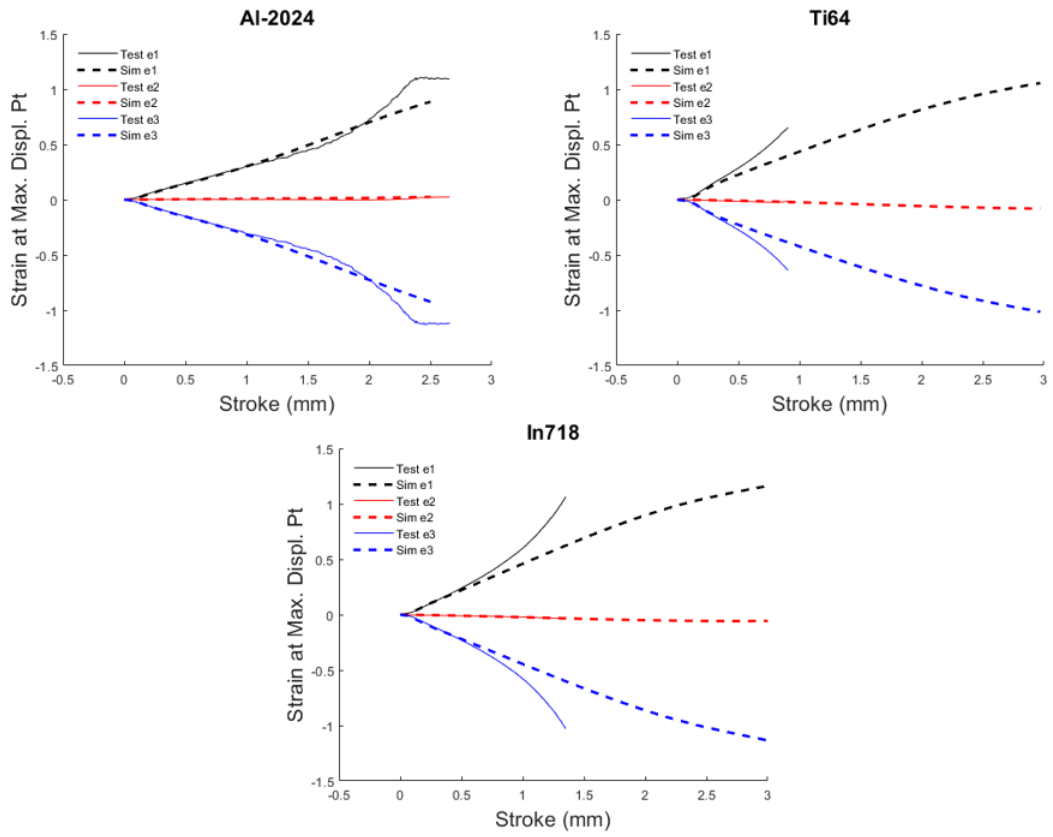

Figure 4.35: Principal strains at fracture points as a function of applied displacement

The Al-2024 and Ti64 test principal strains show excellent agreement with the simulation for the majority of the experiment duration. Once again, it can be seen that the measured DIC strain data is a bit higher than the simulated values at high loads and displacements. This is likely due to the localization of strains at the fracture location, which the simulation cannot account for as constructed. This phenomenon corresponds with the brief flattening of the force-displacement curves, followed by a sharp drop in load corresponding to material fracture. The In718 test principal strains do not align well with the simulations as a function of load due to the stiffer response predicted by the simulation. Strains in these tests accumulate at lower loads and more

rapidly than in the simulation. Plotting the principal strains as a function of displacement shows a better agreement at low displacements. However, the strains begin to increase and deviate from the simulated values at approximately 0.75 mm of displacement. The second principal strains are approximately zero for each case. The second principal direction corresponds to the tangential direction, and the strain being zero in this direction verifies the state of stress is one of plane strain compression.

From the principal strain increments, the evolution of equivalent plastic strain is computed at the fracture points for the tests and compared with simulation results. Once again, because these tests are loaded continuously, elastic strains are inherently present in the equivalent plastic strain calculation. Thus, the plastic strains calculated from the tests will begin accumulating immediately, even though this is not physically true. Because the displacements are so large in these tests, the elastic strains are negligible at higher displacements, so there should still be agreement between test and simulation despite the incorporation of elastic strains in the experimental results. The triaxiality and Lode parameter history at the critical element in simulation is monitored up to the displacement fracture is observed in the tests. The strain and stress state history data are shown in Figure 4.36. For the Al-2024 and Ti64 tests, there is reasonable agreement between the equivalent plastic strains in test and simulation until the test nears fracture. Once again, there is evidence of strain localization near the fracture point in the tests, and the DIC strains deviate from the plasticity models. For Al-2024, it is also clear that the numerical issues caused by element distortion identified earlier are significant. The triaxiality begins to increase and deviate from the designed value of 0.6 at about 1.5 mm of displacement. This is not an issue for Ti64 because fracture occurs well before the point where the stress state

values begin to deviate. However, the effect of incorporating elastic strains into the plastic strain computation is more evident for Ti64 due to the smaller displacements. The simulated plastic strain clearly starts flat, indicating no plastic strain accumulates for roughly 0.1 mm of displacement. This is why the experimental plastic strain is higher at the start. Regardless, the plastic strains at fracture are extracted from the simulations, so the error accumulated from the elastic strains in the tests do not affect the estimation of equivalent plastic strain at fracture.

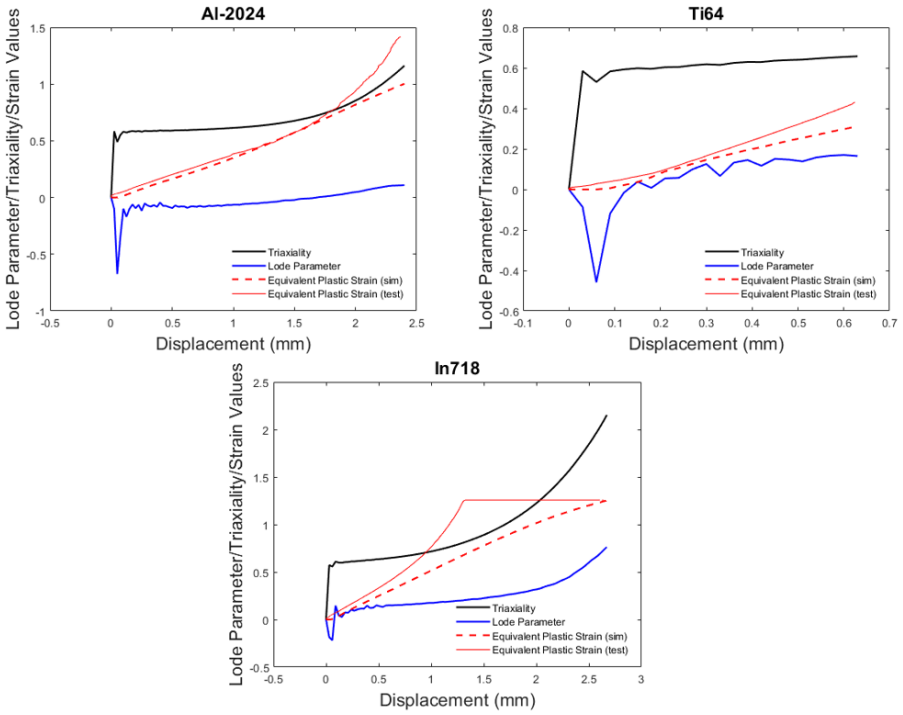

Figure 4.36: Equivalent plastic strain and stress state history

The In718 plastic strain behaves in a similar way as the principal strains. They accumulate much more rapidly than they do in simulation. The main cause of this poor match is the stiffer response predicted in simulation. The strains should accumulate slower in simulation

because the material exhibits more hardening relative to the tests. The material continues to harden until roughly 1.5 mm of displacement in the simulation, whereas hardening in the tests stops at roughly 0.75 mm of displacement. Furthermore, the DIC data tend to drop out well before the ends of the tests, which is indicated by the point where the plastic strain becomes horizontal in Figure 4.36. The instability seen in the stress state also becomes an issue since the In718 specimens survive large displacements without fracturing. The poor correlations between tests and simulation for the In718 notched compression ring along with the inconsistent fracture behavior lead to the conclusion that these tests cannot be reliably used to determine the equivalent plastic strain at fracture for In718 at this stress state. For a triaxiality of 0.6 and Lode parameter of 0, the current fracture surface for In718's *MAT_224 model has a fracture strain of 5.29. This essentially means fracture will not occur in an In718 simulation at this stress state. The results from the tests that fractured show that this claim may not be true.

The equivalent strain to fracture for Al-2024 and Ti64 are estimated by taking the simulated equivalent plastic strain values at the displacements fracture is observed in the tests. The average stress state parameters and current fracture strains in the *MAT_224 material models for those average stress states are tabulated along with the test results in Tables 4.4 and 4.5. Because the strain data do not agree between test and simulation for In718, the equivalent plastic strain from simulation is not assumed to represent the physical behavior. The lowest value of maximum equivalent plastic strain observed in the tests that fracture before DIC data dropout is 1.42. This can be considered a rough estimate of the lower limit of fracture strain for In718 at this state of stress. The actual fracture strain is likely to be significantly higher.

Table 4.4: Al-2024 notched compression ring fracture results

Test	Avg Lode Parameter	Avg Triaxiality	Fracture Strain from Test	Fracture Strain in *MAT_224	Displacement at Fracture (mm)	Load at Fracture (kN)
N2	-0.024	0.6965	0.9809	0.61812	2.34	145
N3	-0.0331	0.6707	0.9133	0.61812	2.19	143
N4	-0.0212	0.7059	1.0028	0.61812	2.38	149
N7	-0.0362	0.6629	0.8901	0.61537	2.13	154
N8	-0.0419	0.649	0.8424	0.61247	2.04	151
N9	-0.0499	0.6308	0.7691	0.61812	1.9	149

Table 4.5: Ti64 notched compression ring fracture results

Test	Avg Lode Parameter	Avg Triaxiality	Fracture Strain from Test	Fracture Strain in *MAT_224	Displacement at Fracture (mm)	Load at Fracture (kN)
N2	0.1047	0.605	0.3816	0.4726	0.7785	164
N4	0.1131	0.6136	0.4229	0.4726	0.8605	165
N5	0.1047	0.605	0.3816	0.4726	0.7502	165

The average triaxialities from the Al-2024 tests show some significant spread and deviation from the target value of 0.6. This is due to the element distortion in simulation at high displacements. The Lode parameter values also show some variability, but they are all relatively close to the target value of 0. If it is assumed that the physical state of stress corresponds to a triaxiality of 0.6 and Lode parameter of 0, as shown in the mesh convergence studies, then the fracture strain predicted by the Al-2024 *MAT_224 model is 0.591. The average fracture strain from the test data is 0.900. Clearly, the fracture strains predicted by the Al-2024 *MAT_224 model are much lower than what is indicated by the test data. The percent error is 52.3%, assuming the experimentally determined value to be the true value. Thus, the incorporation of

this test data into the Al-2024 *MAT_224 fracture surface, shown in Figure 4.37, could significantly increase its accuracy in predicting fracture at high stress triaxialities. The effect of the inaccurate fracture strain prediction is obvious when comparing the force-displacement responses of the test data compared to a simulation using the *MAT_224 model with failure considered, which is plotted in Figure 4.38. The simulation load sharply drops at about 1.5 mm of displacement, whereas the force drops in the tests occur at an average displacement of 2.16 mm.

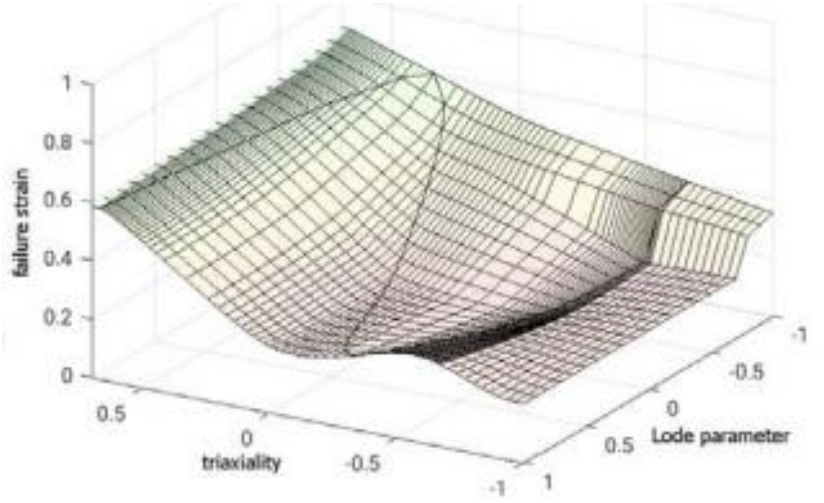

Figure 4.37: Al-2024 *MAT_224 fracture surface

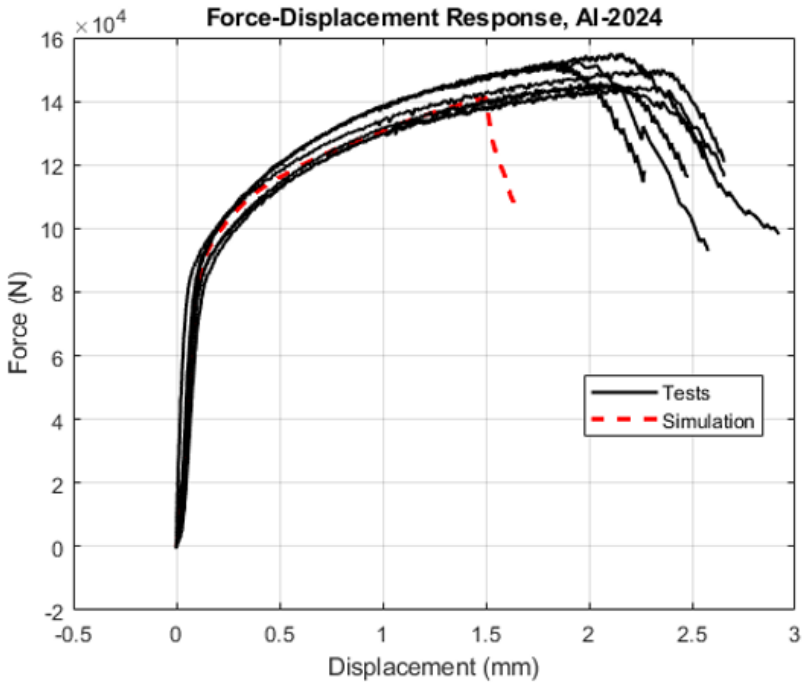

Figure 4.38: Force-displacement responses of Al-2024 notched ring tests and simulation using *MAT_224 failure model

The Ti64 *MAT_224 model is more accurate at this state of stress. For a Lode parameter of 0.1, the fracture strain plateaus at 0.4726 for triaxialities between 0.17 and 4.0. The average fracture strain from the tests is 0.3954, which yields a 19.5% error for the model. The fracture surface, shown in Figure 4.39, could be slightly lowered in this area, but more tests at triaxialities between 0.17 and 0.6 may provide more insight into what the shape of the surface should be. The Ti64 simulation run with the *MAT_224 fracture model, shown in Figure 4.40, shows a sharp load drop at 0.96 mm of displacement, which is slightly higher than the average displacement at fracture in the tests of 0.80 mm.

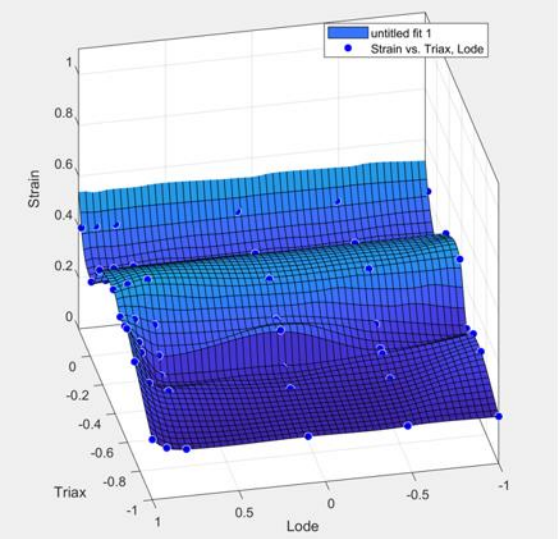

Figure 4.39: Ti64 *MAT_224 fracture surface

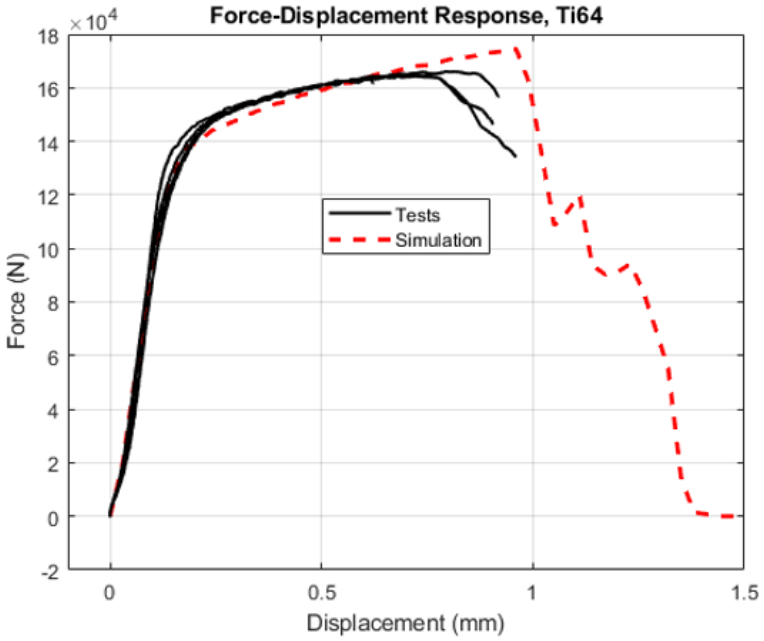

Figure 4.40: Force-displacement responses of Ti64 notched ring tests and simulation using *MAT_224 failure model

Chapter 5 Summary and Conclusions

The equivalent plastic strain at fracture is estimated for Ti64 and In718 under states of stress corresponding to combined asymmetric in-plane tension and out-of-plane compression using a novel backed punch test technique. The equivalent plastic strain at fracture is also estimated for Al-2024, Ti64, and In718 under a state of stress analogous to plane strain compression using a novel notched ring compression specimen. A combined experimental-numerical approach is used for each experiment. The force-displacement relations predicted through simulation are compared with experimental results. If the simulation adequately predicts the material plasticity in the experiments, the equivalent plastic strain in the simulation is extracted at the onset of fracture in the tests, and this value is used to estimate the equivalent plastic strain at fracture at the stress state of interest. This data is then used as a benchmark to evaluate the accuracy of current *MAT_224 ductile fracture models.

5.1 Elliptical Backed Punch

Three unique elliptical backed punch tests are performed with the following geometries and materials: a 0.635 mm (thin) Ti64 specimen with a 1.27 mm 1075 steel backing plate and 2x6 mm punch, a 1.27 mm (thick) Ti64 specimen with a 1.575 mm 1075 steel backing plate and 2x6 mm punch, and a 0.635 mm In718 specimen with a 0.889 mm 1075 steel backing plate and 2x4 mm punch. The simulation results for each test show stiffer force-displacement responses than the tests, especially for In718. However, the strain data at the fracture points match well between simulations and tests, allowing for a reliable estimation of the equivalent plastic fracture strains. The test results indicate the current fracture surface in the Ti64 *MAT_224 material model slightly over predicts the fracture strains for the Ti64 tests, while the In718 *MAT_224

material model accurately predicts the fracture strain. Average stress state parameters are tabulated in section 3.1 along with the fracture strain values.

5.2 Notched Compression Ring

The notched ring experiment is performed on custom test coupons for Al-2024, Ti64, and In718. Numerical analysis shows the physical state of stress converges to a triaxiality of 0.6 and Lode parameter of 0, which is equivalent to a state of plane strain compression. Al-2024 and Ti64 tests show clear fracture that corresponds with a sharp drop in applied load. 3D DIC is used to measure displacements and compute strains. The DIC data show reasonable agreement with the simulations, allowing for estimations of the equivalent plastic strain at fracture to be determined. These values are tabulated in section 3.2. The *MAT_224 model for Al-2024 significantly under predicts the fracture strain, indicating potential for improvements to be made to the model's fracture surface. The *MAT_224 model for Ti64 slightly over predicts the fracture strain, but is more accurate than the Al-2024 model. Some slight modifications can be made to the fracture surface, but the model performs relatively well for the stress states of interest. More fracture test data under compressive states of stress would better inform the fracture surface adjustment.

The In718 simulation predicts a much stiffer response than what is observed in the tests. The test strains are also much higher, which invalidates the typical procedure of extracting a fracture strain value from the simulation. The different boundary conditions used in the tests produce undesirable variations in the results. Fracture is observed for two of the tests, indicating the current In718 *MAT_224 fracture surface may not be accurate at this stress state, as it essentially does not permit fracture in this area of the surface. Further investigations into the

numerical analysis should be performed to match the simulation to the test data. Further improvements to the test, such as devising a test design to acquire better AE data, could help in determining the exact onset of fracture since there is not a clear drop in load as in the Al-2024 and Ti64 notched ring tests.

Appendix A Proposed Punch Test Design Load Paths

A total of 12 elliptical backed punch test geometries for each material are simulated in LS-DYNA. The load path for each is shown.

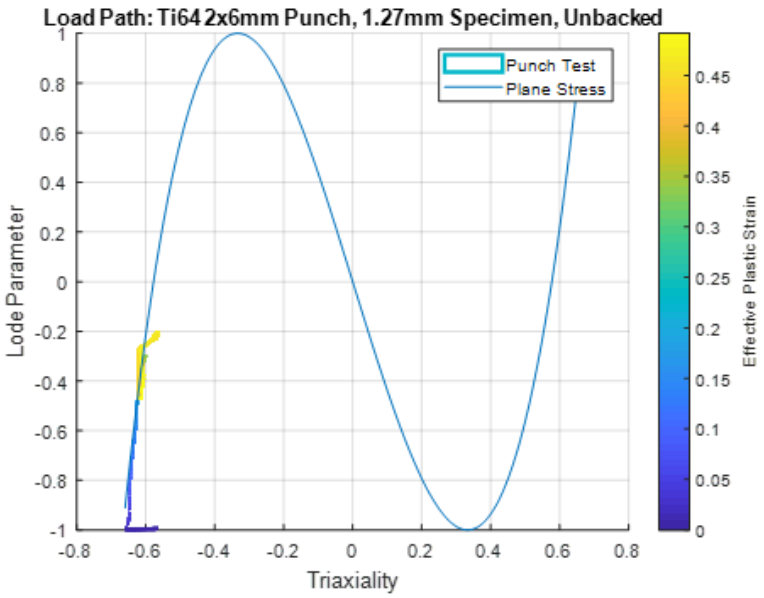

Figure A.1: Ti64, 2x6 mm punch, 1.27 mm specimen, unbacked

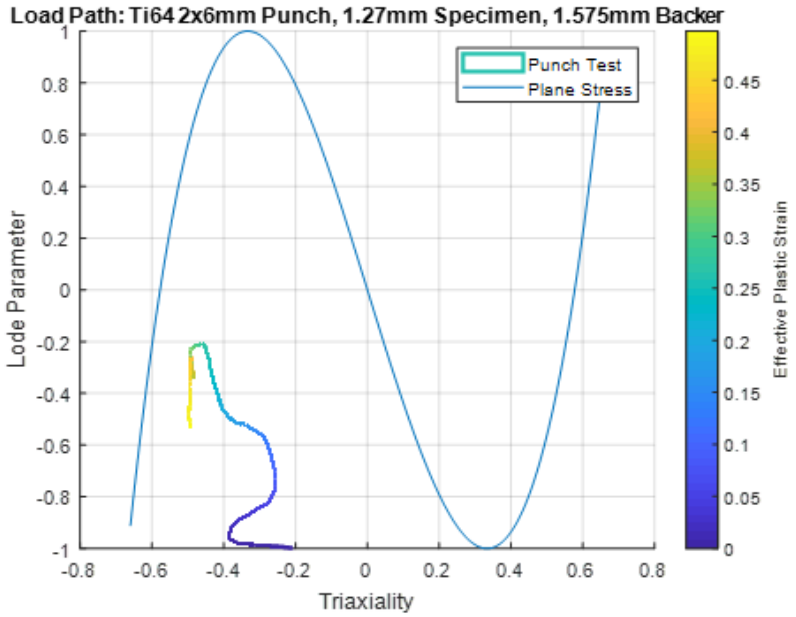

Figure A.2: Ti64, 2x6 mm punch, 1.27 mm specimen, 1.575 mm backer (chosen design)

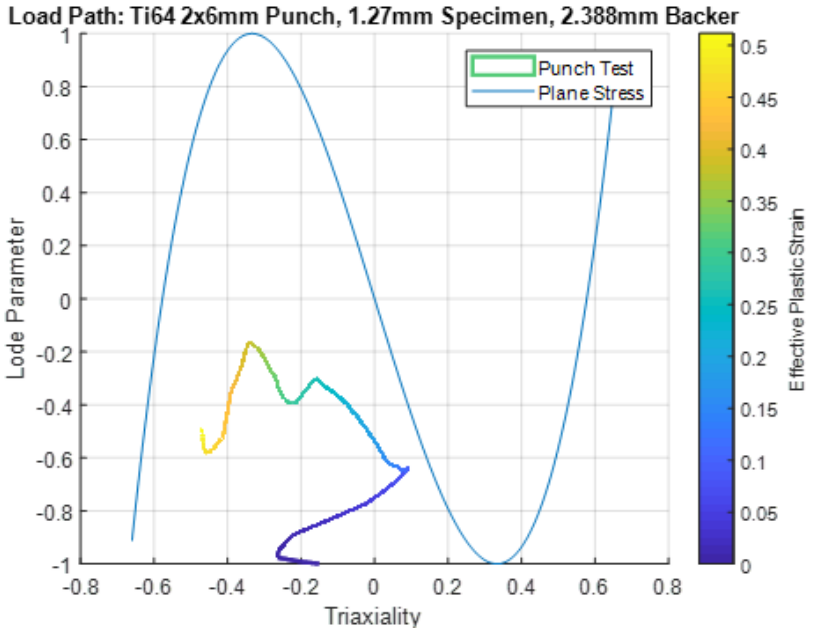

Figure A.3: Ti64, 2x6 mm punch, 1.27 mm specimen, 2.388 mm backer

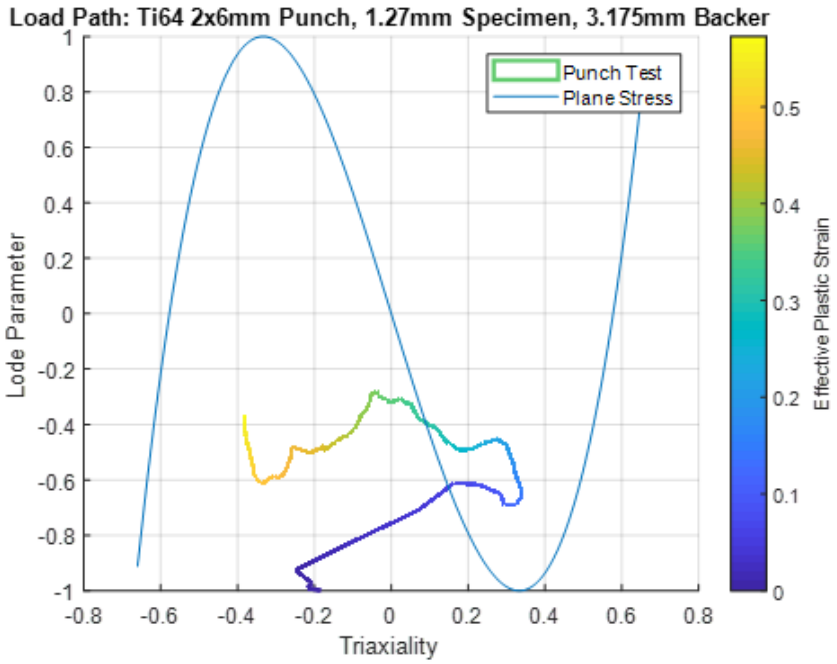

Figure A.4: Ti64, 2x6 mm punch, 1.27 mm specimen, 3.175 mm backer

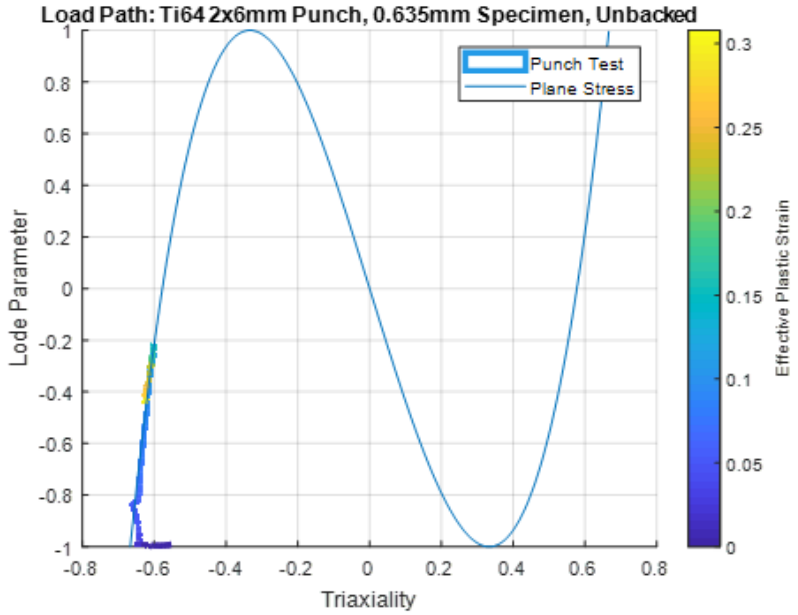

Figure A.5: Ti64, 2x6 mm punch, 0.635 mm specimen, unbacked

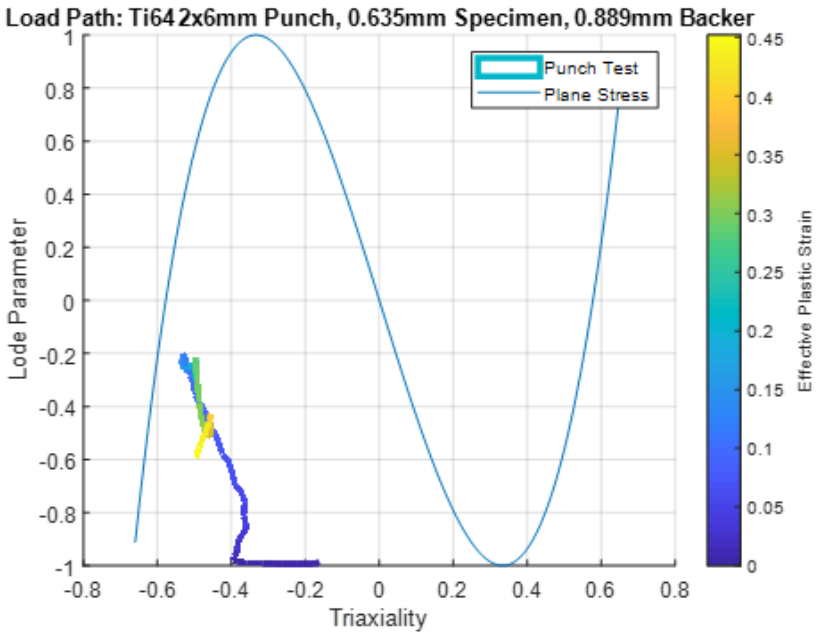

Figure A.6: Ti64, 2x6 mm punch, 0.635 mm specimen, 0.889 mm backer

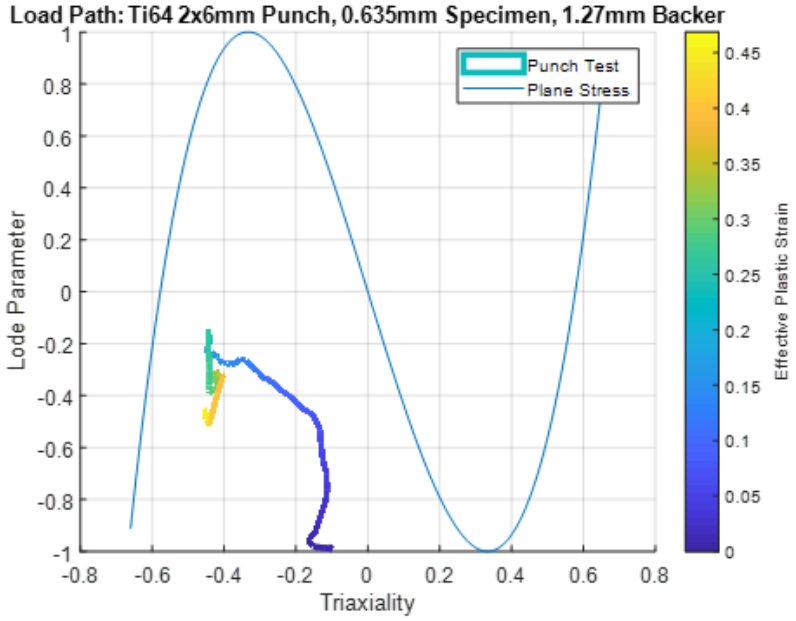

Figure A.7: Ti64, 2x6 mm punch, 0.635 mm specimen, 1.27 mm backer (chosen design)

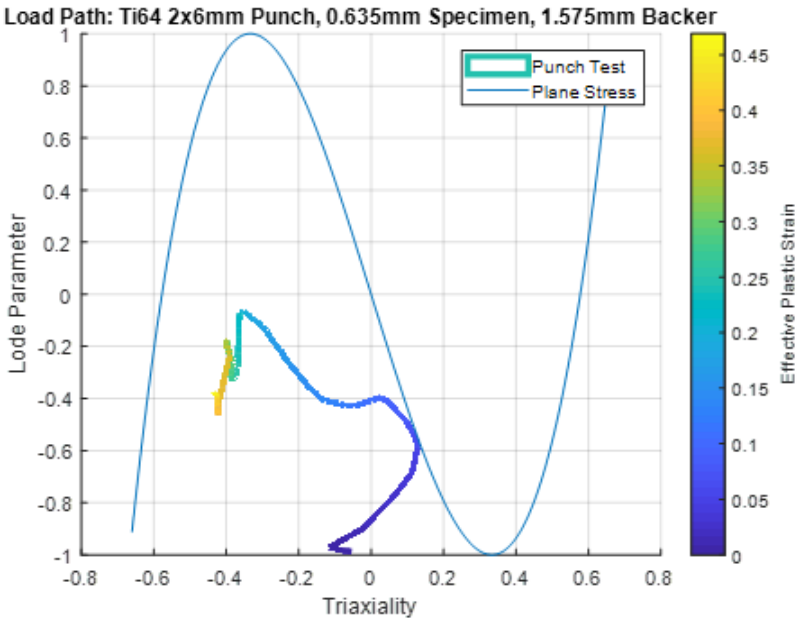

Figure A.8: Ti64, 2x6 mm punch, 0.635 mm specimen, 1.575 mm backer

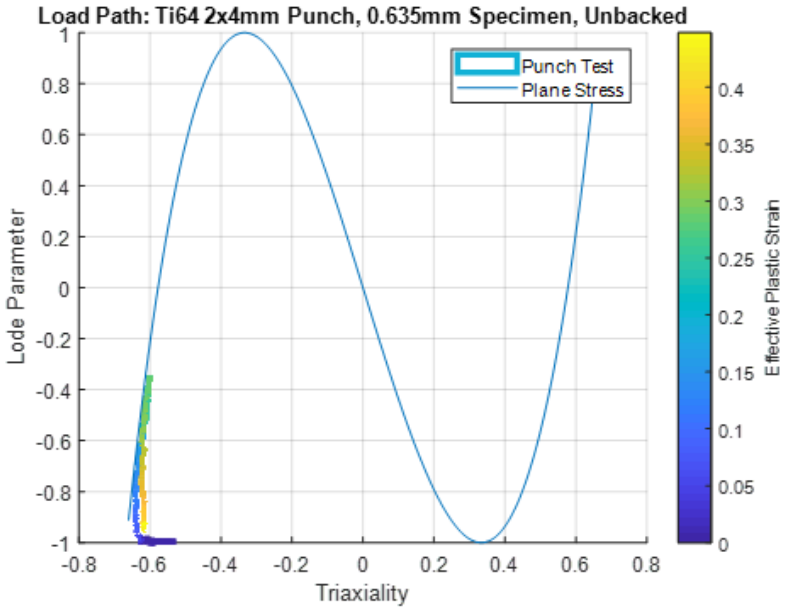

Figure A.9: Ti64, 2x4 mm punch, 0.635 mm specimen, unbacked

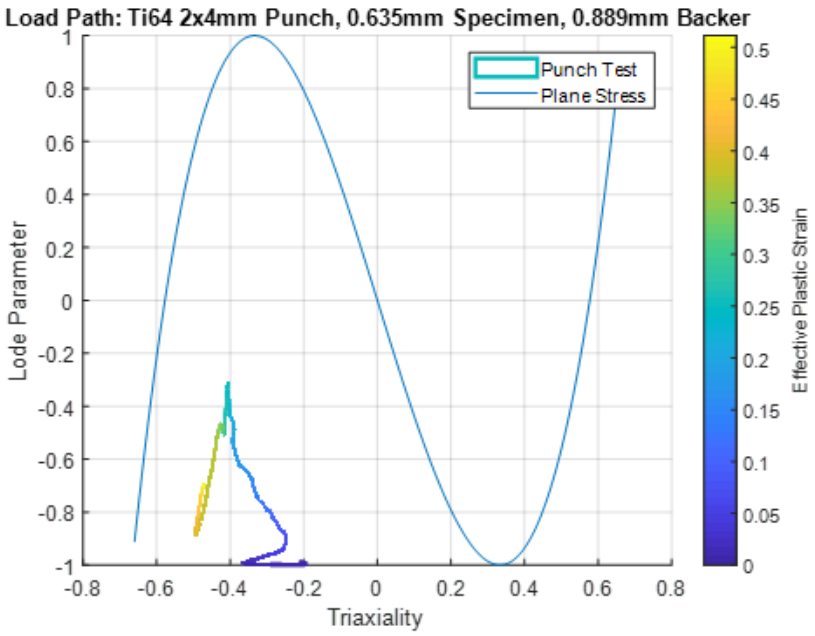

Figure A.10: Ti64, 2x4 mm punch, 0.635 mm specimen, 0.889 mm backer

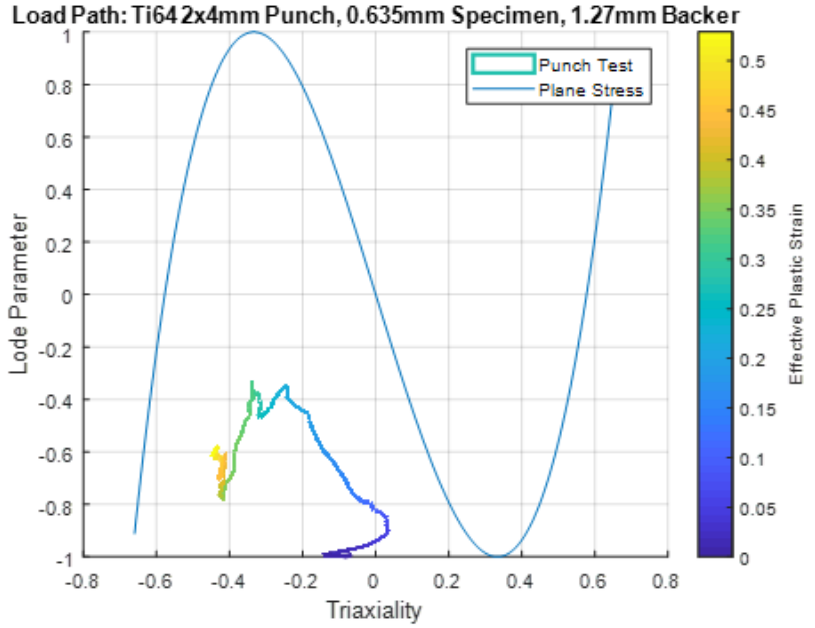

Figure A.11: Ti64, 2x4 mm punch, 0.635 mm specimen, 1.27 mm backer

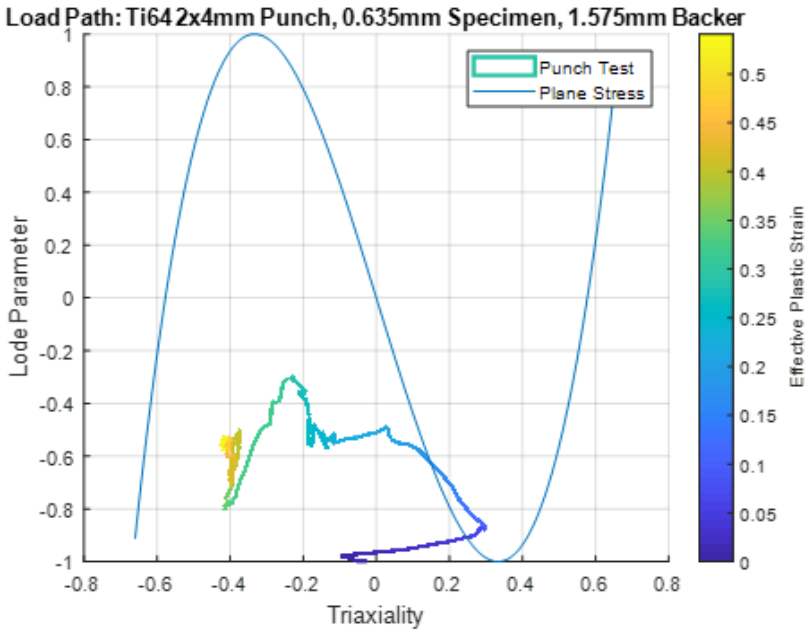

Figure A.12: Ti64, 2x4 mm punch, 0.635 mm specimen, 1.575 mm backer

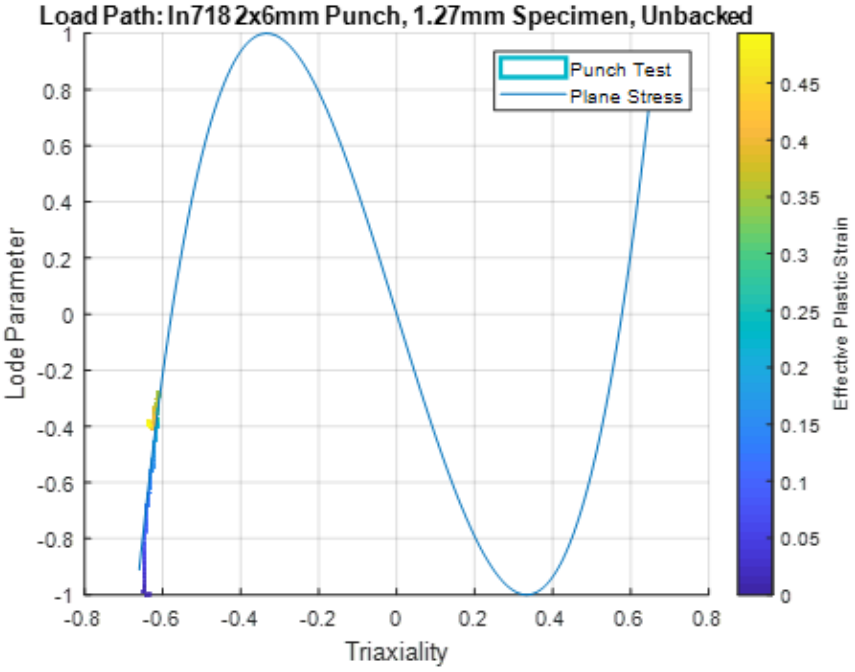

Figure A.13: In718, 2x6mm punch, 1.27 mm specimen, unbacked

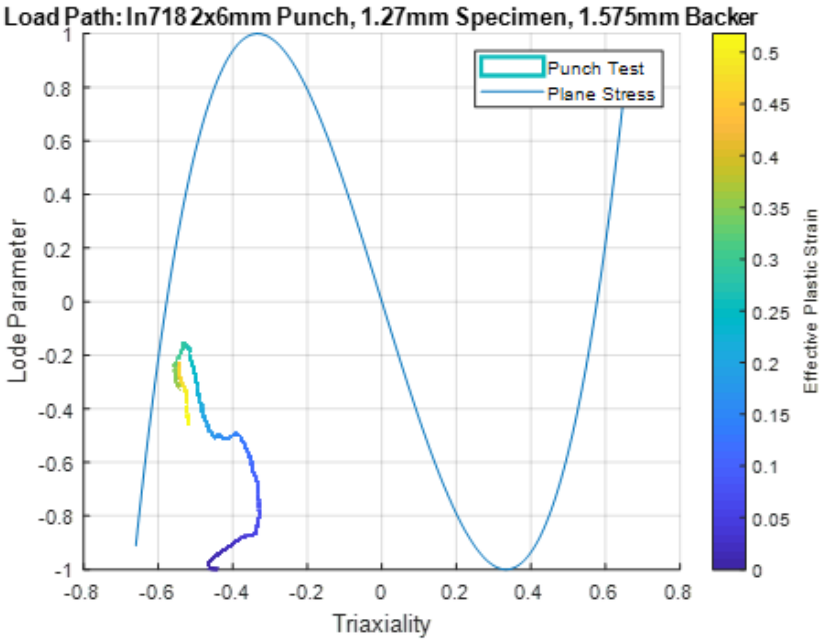

Figure A.14: In718, 2x6mm punch, 1.27 mm specimen, 1.575 mm backer

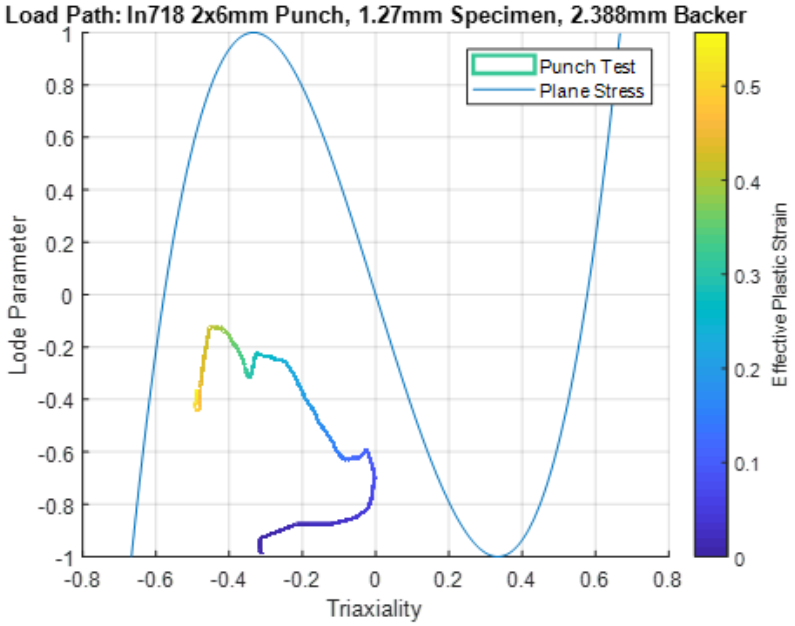

Figure A.15: In718, 2x6mm punch, 1.27 mm specimen, 2.388 mm backer

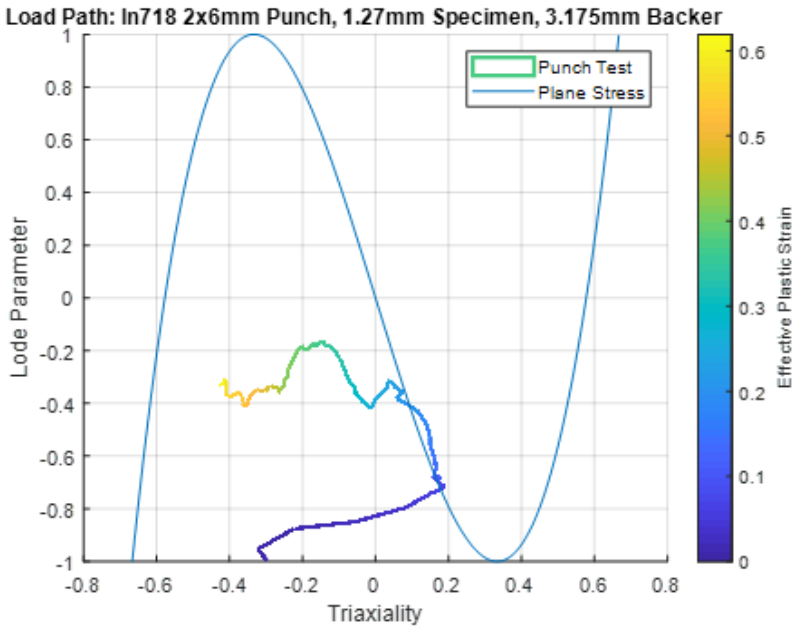

Figure A.16: In718, 2x6mm punch, 1.27 mm specimen, 3.175 mm backer

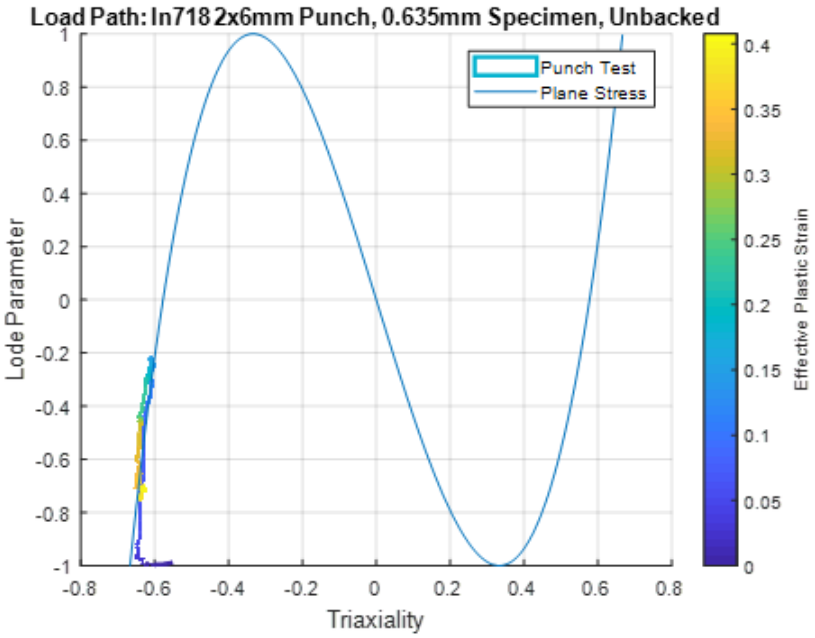

Figure A.17: In718, 2x6mm punch, 0.635 mm specimen, unbacked

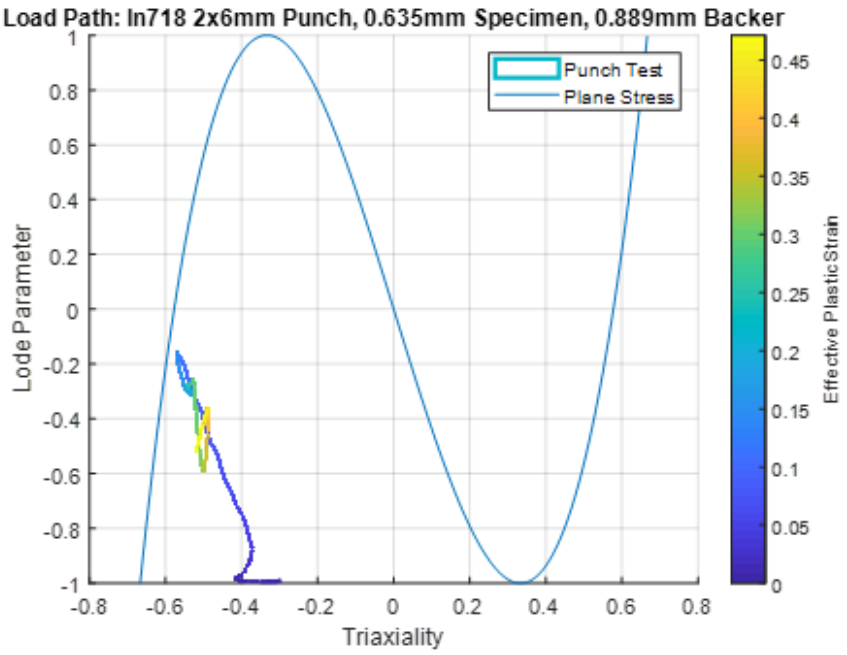

Figure A.18: In718, 2x6mm punch, 0.635 mm specimen, 0.889 mm backer

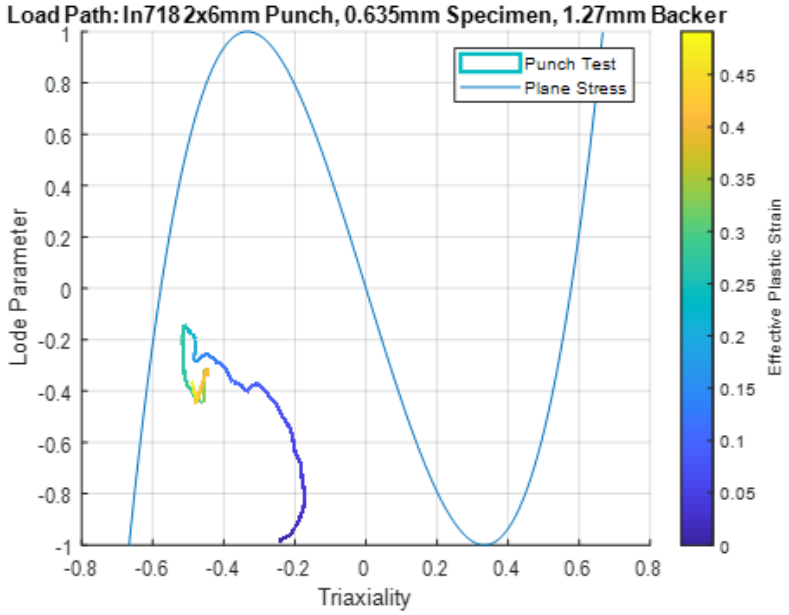

Figure A.19: In718, 2x6mm punch, 0.635 mm specimen, 1.27 mm backer

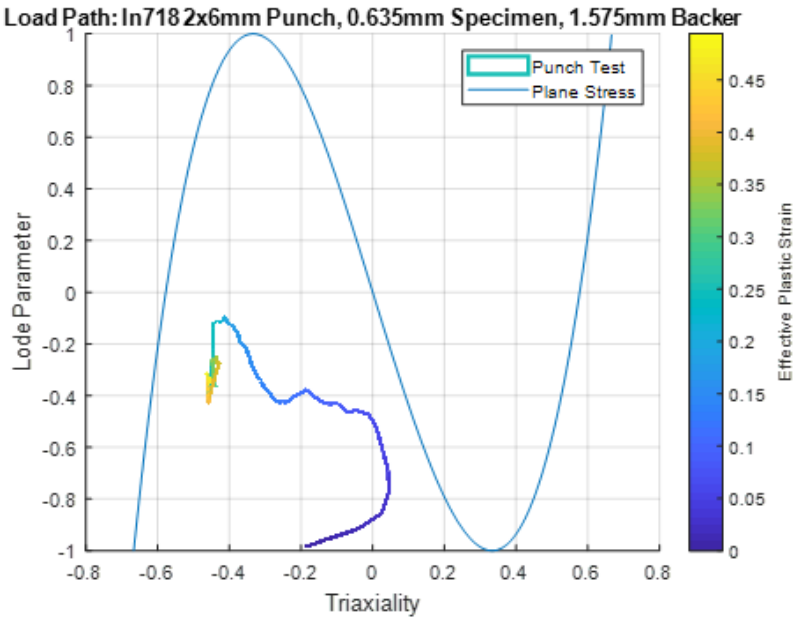

Figure A.20: In718, 2x6mm punch, 0.635 mm specimen, 1.575 mm backer

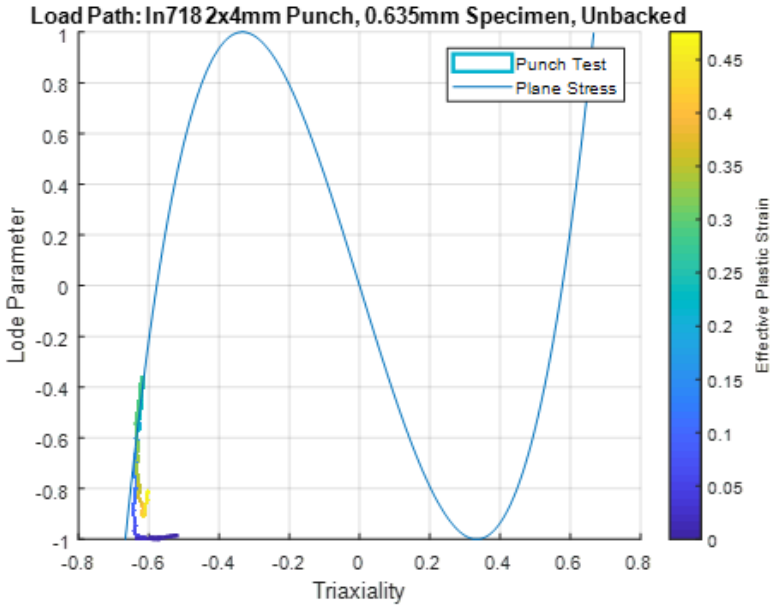

Figure A.21: In718, 2x4mm punch, 0.635 mm specimen, unbacked

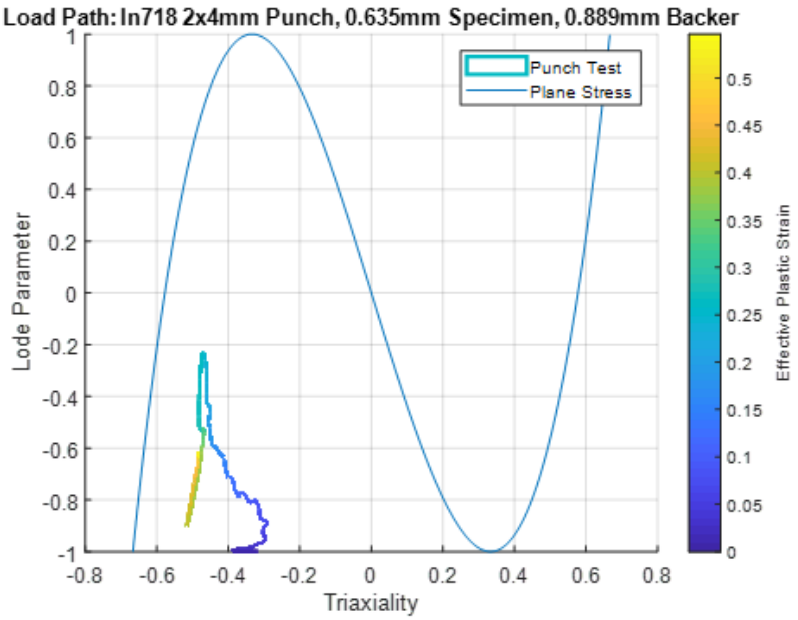

Figure A.22: In718, 2x4mm punch, 0.635 mm specimen, 0.889 mm backer (chosen design)

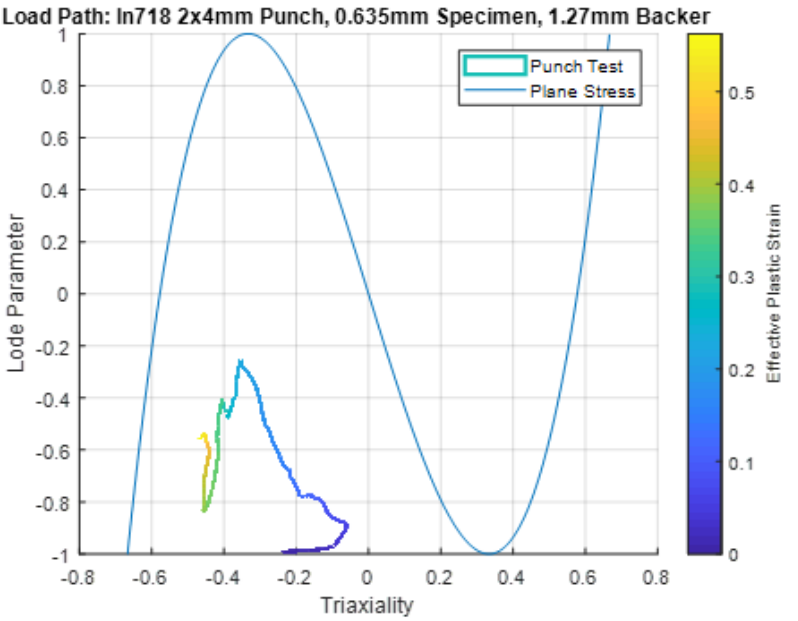

Figure A.23: In718, 2x4mm punch, 0.635 mm specimen, 1.27 mm backer

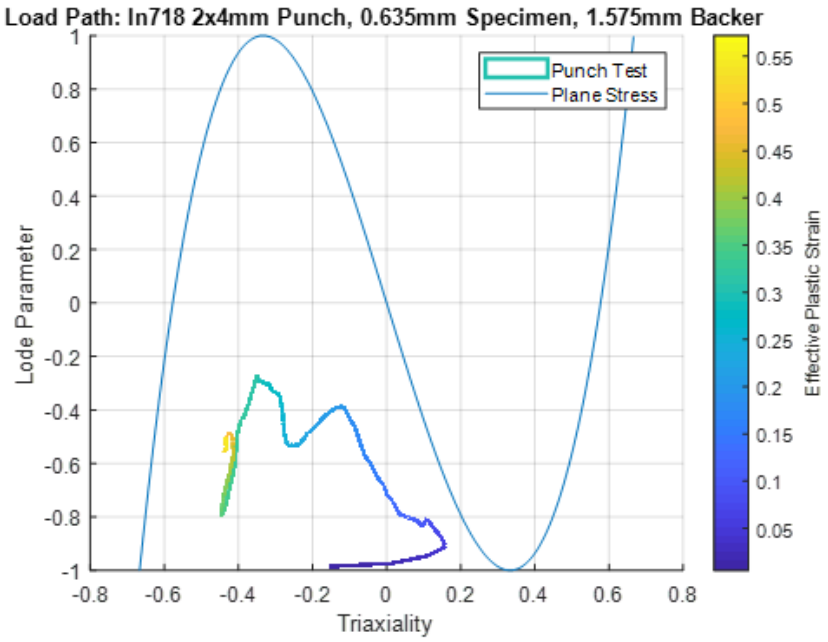

Figure A.24: In718, 2x4mm punch, 0.635 mm specimen, 1.575 mm backer

References

[1] "Aircraft Accident Report-United Airlines Flight 232, McDonnell Douglas DC-10-10, Sioux Gateway Airport, Sioux City, Iowa, July 19, 1989," National Transportation Safety Board, Washington, D.C., NTSB/AAR-90/06, Nov. 1990.

[2] W. Emmerling, D. Altobelli, K.S. Carney, and J.M. Pereira, "Development of a New Material Model in LS-DYNA Part 1: FAA, NASA, and Industry Collaboration Background," Federal Aviation Administration, Washington, D.C., DOT/FAA/TC-13/25, April 2014.

[3] "Aircraft Accident Report- Left Engine Failure and Subsequent Depressurization Southwest Airlines Flight 1380 Boeing 737-7H4, N772SW Philadelphia, Pennsylvania April 17, 2018," National Transportation Safety Board, Washington, D.C., NTSB/AAR-19/03, Nov. 2019.

[4] "United Airlines Flight 328 Boeing 777 Engine Incident." National Transportation Safety Board. ntsb.gov/investigations/Pages/DCA21FA085.aspx.

[5] C.K. Park, K.S. Carney, P. Du Bois, D. Cordasco, and C.D. Kan, "Aluminum 2024-T351 Input Parameters for *MAT_224 in LS-DYNA," Federal Aviation Administration, Washington, D.C., DOT/FAA/TC-19/41, P1, March 2020.

[6] R.L. Lowe, J.D. Seidt, and A. Gilat, "Characterization of the Lode = -1 Meridian on the Al-2024 Failure Surface for *MAT_224 in LS-DYNA," *Proc. 14th International LS-DYNA Users Conference,* 2016

[7] N. Spulak, R.L. Lowe, J.D. Seidt, A. Gilat, C.K. Park, and K.S. Carney, "Ductile fracture under in-plane biaxial tension and out-of-plane compression," *International Journal of Solids and Structures*, vol. 202, pp. 234-242, Oct. 2020.

[8] N. Spulak "Investigations into ductile fracture and deformation of metals under combined quasi-static loading and under extremely high-rate compressive impact loading," Ph.D. dissertation, Dept. of Mechanical and Aerospace Engineering, The Ohio State University, Columbus, OH, 2022.

[9] G.R. Johnson and W.H. Cook, "Fracture characteristics of three metals subjected to various strains, strain rates, temperatures, and pressures," *Engineering Fracture Mechanics*, vol. 21, pp. 31-48, 1985.

[10] Y. Bao and T. Wierzbicki, “On fracture locus in the equivalent strain and stress triaxiality space,” *International Journal of Mechanical Sciences*, vol. 46, pp. 81-98, Feb. 2004.

[11] I. Barsoum and J. Faleskog, “Rupture Mechanisms in combined tension and shear-Experiments,” *International Journal of Solids and Structures*, vol. 44, pp. 1768-1786, Oct. 2006.

[12] T. Wierzbicki, Y. Bao, Y.W. Lee, and Y. Bai, “Calibration and evaluation of seven fracture models,” *International Journal of Mechanical Sciences*, vol. 47, pp. 719-743, March 2005.

[13] X. Gao and J. Kim, “Modeling of ductile fracture: Significance of void coalescence,” *International Journal of Solids and Structures*, vol. 43, pp. 6277-6293, Sep 2005.

[14] A.B. Watts and H. Ford, “An Experimental Investigation of the Yielding of Strip Between Smooth Dies,” *Proceedings of the Institute of Mechanical Engineers*, vol. 1, pp. 448-453, 1952.

[15] M.S. Loveday, G.J. Mahon, B. Roebuck, A.J. Lacey, E.J. Palmiere, C.M. Sellars, and M.R. van der Winden, “Measurement of flow stress in hot plane strain compression tests,” *Materials at High Temperatures*, vol. 23, pp. 85-118, May 2006.

[16] M. Pietrzyk, J.G. Lenard, and G.M. Dalton, “A Study of the Plane Strain Compression Test,” *CIRP Annals*, vol. 42, pp. 331-334, 1993.

[17] A.P. Carvalho, L.M. Reis, R.P.R.P. Pinheiro, P.H.R. Pereira, T.G. Langdon, and R.B. Figueiredo, “Using Plane Strain Compression Test to Evaluate the Mechanical Behavior of Magnesium Processed by HPT,” *Metals*, vol. 12, Jan. 2022.

[18] P. Wang, Y. Sang, L. Shao, and X. Guo, “Measurement of the deformation of sand in a plane strain compression experiment using incremental digital image correlation,” *Acta Geotechnica*, vol. 14, pp. 547-557, May 2018.

[19] P. Kubík, F. Sebek, J. Hulka, and J. Petruska, “Calibration of ductile fracture criteria at negative stress triaxiality,” *International Journal of Mechanical Sciences*, vol. 108-109, pp. 90-103, April 2016.

[20] J.D. Seidt, “Development of a New Metal Material Model in LS-DYNA Part 3: Plastic Deformation and Ductile Fracture of 2024 Aluminum Under Various Loading Conditions,” Federal Aviation Administration, Washington, D.C., DOT/FAA/TC-13/25, P3, April 2014.

[21] J.T. Hammer, "Plastic Deformation and Ductile Fracture of Ti-6Al-4V under Various Loading Conditions," M.S. Thesis, Dept. of Mechanical and Aerospace Engineering, The Ohio State University, Columbus, OH, 2012.

[22] T.J. Liutkus, "Digital Image Correlation in Dynamic Punch Testing and Plastic Deformation Behavior of Inconel 718," M.S. Thesis, Dept. of Mechanical and Aerospace Engineering, The Ohio State University, Columbus, OH, 2014.

[23] M.A. Sutton, J.J. Orteu, and H.W. Schreier, *Image Correlation for Shape, Motion and Deformation Measurements Basic Concepts, Theory and Applications*, New York, NY, Springer Science+Business Media, 2009.

[24] *PCI-2 Based AE System User's Manual Rev 3*, Physical Acoustics Corporation, Princeton Junction, NJ, 2007.

[25] L. Wang, K.S. Carney, P. Du Bois, and C.D. Kan, FAA Progress Report 11/04/2020 [PowerPoint Slides].

[26] S. Haight, L. Wang, P. Du Bois, K.S. Carney, and C.D. Kan, "Development of a Titanium Alloy Ti-6Al-4V Material Model Used in LS-DYNA," Federal Aviation Administration, Washington, D.C., DOT/FAA/TC-15/23, May 2016.

[27] S. Dolci, "The Influence of Strain Rate, Temperature Effects, and Instabilities in Failure Modeling for Metal Alloys," Ph.D. dissertation, George Mason University, Fairfax, VA, 2021.

[28] "LS-DYNA Material Parameter Sets." AWG.Ansys.com. awg.ansys.com/Material+Parameter+Sets.

[29] J.D. Seidt, C.K. Park, M. Buyuk, R.L. Lowe, L. Wang, K.S. Carney, P. Du Bois, A. Gilat, and C.D. Kan, "An Experimental Investigation of the Influence of the State of Stress on the Ductile Fracture of 2024-T351 Aluminum," *Journal of Engineering Materials and Technology*, vol. 144, Oct. 2022.